Zentralinstitut für Medizintechnik
Technische Universität München

Dissertation

Thomas Gaaß

Acceleration of Radial Data Acquisition in Medical Imaging via Iterative, Histogram-Constrained Reconstruction

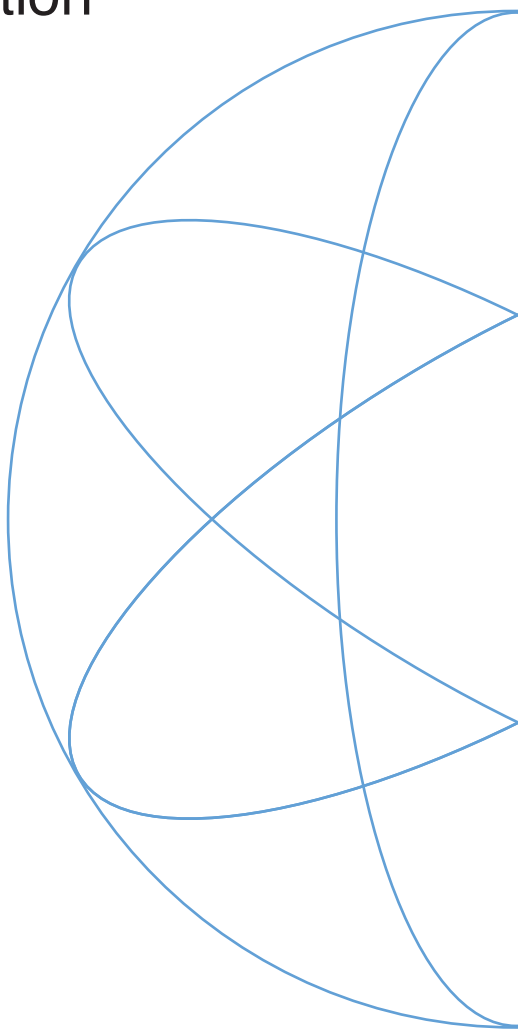

Supervised by Prof. Dr. Axel Haase
and Prof. Dr. Franz Pfeiffer

28. October 2013

Physik Department

Zentralinstitut für Medizintechnik
und
Lehrstuhl für Angewandte Biophysik (E17)

Acceleration of Radial Data Acquisition in Medical Imaging via Iterative, Histogram-Constrained Reconstruction

Thomas H. Gaaß

Vollständiger Abdruck der, von der Fakultät für Physik der Technischen Universität München zur Erlangung des akademischen Grades eines

Doktors der Naturwissenschaften (Dr. rer. nat.),

genehmigten Dissertation.

Vorsitzender:		Univ.-Prof. Dr. Norbert Kaiser
Prüfer der Dissertation:	1.	Univ.-Prof. Dr. Axel Haase
	2.	Univ.-Prof. Dr. Franz Pfeiffer

Die Dissertation wurde am 28.10.2013 bei der Technischen Universität München eingereicht und durch die Fakultät für Physik am 10.12.2013 angenommen.

Abstract

The need to reduce measurement time in magnetic resonance imaging (MRI) and dose in modern X-ray computed tomography (CT) acquisitions is a demanding task. The intrinsically long acquisition time in MRI when compared to physiological processes, such as respiratory and cardiac cycles, results in artifacts in static acquisitions and prohibits high temporal resolution in dynamic MRI. While acquisition time is not an issue in CT applications, novel developments such as phase-contrast CT (PCCT) have to meet strict dose limitations when aiming for clinical operation. Several approaches have emerged aiming at accelerating image acquisitions and lowering dose by reducing the amount of acquired data, so called *undersampling*, and subsequently compensating for induced aliasing artifacts. Iterative reconstruction techniques exploiting spatial and temporal redundancies in undersampled data acquisition for the suppression of aliasing artifacts have shown to be of great success. However, shortcomings regarding spatial resolution in non-dynamic acquisition and temporal resolution in case of dynamic acquisitions call for the investigation of improvements for current techniques or adequate substitutes.

For the acceleration of MR acquisitions a novel approach to reconstruct undersampled radial data via gradient driven regularized minimization is introduced. In the proposed method the histogram entropy of the reconstruction is employed as a measure of aliasing artifact and as the basis for their suppression. Reducing the image entropy via a low-entropy reference histogram yields a correction of artifacts in image space. The performance of the approach is evaluated on numerical simulations as well as on static and dynamic radially acquired *in vivo* MRI data. For non-dynamic reconstruction, two radial head MRI examinations were conducted and reconstructed. Time-resolved data was generated in terms of two individual, radially acquired functional cardiac MRI examinations.

Regarding dose reduction for PCCT acquisition a comprehensive evaluation of a compressed sensing inspired approach is presented. The performance of the reconstruction technique is evaluated on numerical simulations and *in vitro* measurements. Data was acquired with both a high-brilliance synchrotron X-ray source and a conventional tube source. Specimen included a fixated mouse, a fixated de-calcified mouse and a multi-contrast fluid phantom. Compressed sensing based reconstruction, reference histogram constrained artifact suppression and the combination of both is evaluated qualitatively and quantitatively.

Results demonstrate the possibility to lower the amount of data acquired by up to a factor of 16 without perceptual loss in image quality. Consequently, measurement time in MRI and dose in PCCT can be drastically reduced, resulting in higher spatio-temporal resolution and decreased patient risk, respectively. Sophisticated reconstruction techniques, such as the introduced, open up the possibility of cinematographic acquisitions of fast physiological processes and the potential transition of PCCT into clinical application in the future.

Zusammenfassung

Ein zentraler, limitierender Faktor in der medizinischen Magnetresonanztomographie (MRT) ist die intrinsisch lange Aufnahmezeit. Daher ist ein bedeutender Teil aktueller Forschung auf die Beschleunigung von MRT-Aufnahmen, unter anderem durch alternative Rekonstruktionsverfahren, fokussiert. Während auf dem Gebiet der Computertomographie (CT) Aufnahmezeiten keinen limitierenden Faktor darstellen, unterliegen vor allem auch Neuentwicklungen, wie die Phasenkontrast CT (PCCT) strengen dosislimitierenden Auflagen. Jüngst erhielt ein Rekonstruktionsansatz große Aufmerksamkeit, der potentiell sowohl die Aufnahmezeit in MRT-Untersuchungen, als auch die Strahlendosis in PCCT-Aufnahmen reduzieren kann. Dieser basiert auf der Idee, Messungen mit reduzierter Abtastdichte, das heißt reduzierter Datenmenge, durchzuführen und im Nachhinein auftretende Faltungsartefakte zu korrigieren. Als Grundlage dienen hierbei im Allgemeinen regularisierte, iterative Optimierungsverfahren. Während die meisten dieser Algorithmen zu relativ guten Ergebnissen führen, zeigen viele der bestehenden Methoden Unzulänglichkeiten bezüglich der räumlichen und/oder zeitlichen Auflösung der rekonstruierten Bilder.
Innerhalb dieser Arbeit soll ein neuer Ansatz vorgestellt werden, der auf Grundlage der Shannon-Entropie, bzw. des Intensitätshistogramms ein Maß für radiale Aliasing-Artefakte und deren Korrektur berechnet. Der entwickelte Algorithmus wurde sowohl auf die speziellen Gegebenheiten von dynamischer und nicht-dynamischer MRT, als auch auf PCCT Messungen angepasst. Zur Evaluation der Methode wurden numerischen Simulationen, wie auch *in vivo* Untersuchungen an gesunden Probanden durchgeführt. Hierbei wurden zwei unabhängige MRT-Messungen am Kopf, sowie zeitlich aufgelöste Herzaufnahmen durchgeführt und mit der neu entwickelten entropiegestützten Methode rekonstruiert.
Bei den präsentierten Experimenten an PCCT Daten liegt der Fokus dieser Arbeit, neben der Anwendung des entwickelten entropiegestützten Ansatzes, auf einer umfassenden Validierung von sogenannten 'compressed sensing' (CS) basierten Rekonstruktionsverfahren. Diese wurden bis dato vor allem bei der MRT benutzt. Messungen wurden sowohl mit einer Synchrotron-Röntgenquelle, als auch einer konventionellen Röhrenquelle durchgeführt.
In allen Rekonstruktionen zeigt sich eine qualitativ wahrnehmbare und messbare Verbesserung der Bildqualität im Vergleich zu Standardmethoden, bei einer, um biszu 16-fachen Reduzierung der Datenmenge. PCCT Untersuchungen konnten zeigen, dass die Anwendung einer CS-basierten Optimierung bei stark verringerter Dosis zu vergleichbaren Erfolgen führt, wie sie bereits aus der MRT bekannt sind. Bei der Kombination mit der entwickelten entropiegestützten Methode konnte auch hier eine deutliche Steigerung der erreichbaren Bildqualität bei dosis-limitierten Aufnahmen gezeigt werden. Die untersuchten Techniken zeigen das Potential in Zukunft noch detailiertere cinematographische Aufnahmen, sowie die klinischen Anwendung von PCCT zu ermöglichen.

Contents

1 Introduction

1.1 Rapid undersampled, radial magnetic resonance imaging

Magnetic resonance imaging (MRI) has developed into a irreplaceable non-invasive diagnostic tool in modern medicine. Its foundation was set by the discovery of nuclear magnetic resonance (NMR) by Felix Bloch [1] and Edward Mills Purcell [2] in 1945, awarded with the Nobel Prize for Physics in 1952. Since then NMR was developed further as a spectroscopy tool for the structural analysis of complex molecules. But it was not until the early 1970's that the principles underlying magnetic resonance imaging were found by Sir Peter Mansfield [3] and Paul C. Lauterbur [4]. The ingenious idea to spatially encode the acquired global signal by imprinting magnetic field gradients was assigned with the Nobel Prize in Physiology and Medicine in 2002. MRI, hence the translation of NMR into an imaging modality offers the possibility for non-invasive, high-resolution three-dimensional imaging of alive specimen with an unparalleled variety of applications. The versatile possibilities of designing MRI experiments led to the development of numerous approaches for generating image information. Using basically an unchanged MRI device it is possible to generate images dependent on the diffusion coefficient [5, 6], display blood flow [7, 8], quantify blood distribution [9], perform functional brain imaging [10, 11] or ventilation imaging on the lung [12, 13] to only name a few applications. However, one major challenge still subject to current scientific interest is the intrinsically long acquisition time of MR images when compared to rapid inner body processes. While latest accomplishments in the fields of hard- and software development opened up the possibility to realize cinematographic MRI, the urge for higher spatial image resolution and temporal resolution calls for a reconsideration of the basic principles of signal processing in order to expand resolution limits within the inherent hardware limitations.

The need to save measurement time and to temporally resolve fast physiological processes holds a demanding task for modern magnetic resonance imaging (MRI). The intrinsically long acquisition times in MRI when compared to processes, such as respiratory and cardiac cycles, patient motion or blood pulsation results in artifacts in the reconstruction. Especially imaging techniques such as magnetic resonance angiography (MRA) [7, 14, 15], cardiac imaging [16–18] and dynamic contrast-enhanced MRI (DCE MRI) [19–21] aim for very short acquisition times.

Several approaches have been reported aiming to accelerate MRI acquisitions. Well-established post-processing algorithms such as SMASH [22–24], GRAPPA [24–26], PILS [24, 27] and SENSE [24, 28, 29] utilize multi-coil information to accelerate MRI acquisitions. The spatial information from the phased array coils is used to reconstruct simultaneously acquired partial images of the object. These techniques manage to reduce acquisition times, however, the limitation to low reduction factors poses a possible shortcoming.

On the acquisition side, beside accelerated sequence design, such as FLASH [30, 31] and balanced steady-state free precession (bSSFP) [32–34], the most promising work to decrease measurement time is done on altering k-space trajectories from the traditional Cartesian grid sampling. Reconstruction techniques, such as the non-uniform fast Fourier transform algorithm (NUFFT) [35–37] offer the possibility to reconstruct images from basically any k-space sampling design. Sampling schemes, such as radial sampling are not only fast and robust, but also enable the use of novel reconstruction and post-processing techniques.
In non-dynamic MRI numerous approaches are based on utilizing spatial redundancies in the image. The straightforward approach to save measurement time in single acquisition of static objects is to reduce the amount of acquired data per k-space. However, a decrease in sampling density causes unavoidable aliasing or undersampling artifacts in the conventionally reconstructed image. Compressed sensing (CS) [38–44] and similar techniques take advantage of the distinctive nature of artifacts resulting from specific sampling schemes. Artifacts in acquisitions, using pseudo-random or also radial sampling schemes manifest as noise-like or *incoherent* image impairments, offering an opportunity to differentiate between image features and artifacts. Universal image features, such as sparsity can be employed as prior information in a non-linear iterative reconstruction framework. The term incoherent refers to a definition, introduced by Donoho [39], which characterizes the relationship between the basis of the imaging domain and the sampling pattern.
In dynamic MRI several techniques [45] aim to utilize redundancies in the spatial, temporal or spatio-temporal domain to recover images from undersampled data sets. Approaches using temporal redundancy include Keyhole [46–48], BRISK [16] and TRICKS [7], which base on view-sharing of high frequencies.
Techniques employing both spatial and temporal redundancy simultaneously comprise UNFOLD [49], TSENSE [50], x-f Choice [51], k-t BLAST [52], k-t SENSE [52], or compressed sensing based approaches, such as k-t SPARSE [53]. These techniques correct for undersampling artifacts by transformation in other reconstruction domains (x-f / k-t / x-PC space) and utilization of reference or training data of low spatial resolution. While dynamic contrast changes are recovered in the aforementioned techniques, bulk motion is generally not corrected effectively.
Another group of techniques, comprising TSENSE [17], TGRAPPA [54], HYPR [55], HYPR-LR [56], PR-FOCUSS [57] and PICCS [58] are representative techniques in the category of subsequent spatial and temporal correction. A time averaged composite image is utilized to either calibrate parallel imaging reconstruction or spatially constrain single time frames. While this composite image yields an aliasing-free reconstruction, temporally averaged structures may be projected into the single frame reconstruction.
A different family of non-dynamic approaches, denoted as maximum entropy methods (MEM) was previously mostly applied in astronomy and spectroscopy [59–61] but has also found applications in the registration [62] and reconstruction [63–66] of medical images. ME techniques utilize the Shannon entropy [67, 68] or the intensity histogram [69, 70] as a measure of artifacts, similar to sparsity in CS frameworks.
The technique presented in this work is also based on an iterative optimization employing prior knowledge in the form of reference data. However, in contrary to most of the

aforementioned methods a non image space based representation is used to constrain the iterative reconstruction. By using the intensity histogram as a measure of image quality and aliasing artifacts, the reconstruction becomes independent from the actual image space representation, posing a huge advantage when dealing with undersampled data and dynamic changes.
After extensively explaining the theoretical background of the proposed algorithm in Chapter 3, Chapter 4 will demonstrate that a low-resolution reconstruction of static radially undersampled data yields an artifact-free image. Further it will be shown that the low-entropy histogram of said reconstruction can be employed as reference in order to correct aliasing artifacts in the full resolution image. Subsequently, Chapter 5 will introduce a low-entropy reference computed from the composition of dynamically acquired radial MR data and introduce a comprehensive framework employing both spatial low-resolution and temporal low-resolution information as artifact-free reference. Qualitative and quantitative results are presented on numerical simulations and *in vivo* MR measurements in both cases. Finally Chapter 6 concentrates on the evaluation of the influence of different algorithm parameters, as well as the optimization of the employed optimization constraints.

1.2 Low-dose phase-contrast computed tomography

Conventional X-ray based computed tomography (CT) is a well-established medical imaging modality. The underlying principle of recording the transmitted intensity after penetrating an object is basically unchanged since the discovery of X-rays by W. C. Röntgen in 1895 [71]. CT denotes the computerized reconstruction of a multi-angle acquisition to a three-dimensional object. X-rays produce high-resolution images of strongly absorbing materials, such as bones, based on the difference in the imaginary part of the complex refractive index. However, due to the low absorption cross-section of low-Z (Z being the atomic number) elements, such as soft tissue in biological matter, the use of conventional CT is limited or has to be overcome by the use of highly absorbing contrast agents.
Over the past ten years the idea of phase-sensitive imaging was employed in the context of X-ray imaging. X-ray phase-contrast computed tomography (PCCT) techniques additionally acquire information about the real part of the refractive index corresponding to an X-ray phase shift. Recently developed techniques for the extraction of phase information comprise propagation based imaging [72], the analyzer based approach [73, 74] and grating based imaging [75–78]. Grating based PCCT was initially, successfully implemented at X-ray synchrotron radiation sources for *in vitro* measurements. Since grating-based PCCT acquisition can also be realized with conventional X-ray tubes [78–81], this method is in particular of interest for potential future medical examinations [82–84] and is therefore the technique of choice within this work.
It has been demonstrated that grating-based PCCT projections can be reconstructed using filtered backprojection (FBP), by implementing an altered filter [85]. As in conventional absorption based CT, a certain sampling density has to be achieved also in PCCT measurements. Consequently, in order to generate a high-resolution image without artifacts a large number of projections is necessary. Ultimately the goal is to translate PCCT into

clinical applications, where a large number of projections would cause an undesirable large radiation exposure.
While precise dose optimization has yet to be performed when using PCCT, following the ALARA (as low as reasonable) principle, dose reduction is an important issue for clinical applications. The straightforward way to save measurement time, as well as dose is to reduce the number of projection images per gantry rotation. However, conventional FBP reconstruction of such few-view data sets results in images impaired by aliasing artifacts.
Since conventional CT examinations face the same dose-limiting restrictions as PCCT, this issue has led to the development of numerous approaches on alternative reconstruction techniques. In contrary to the pure analytical reconstruction using FBP, analytical methods comprising ART (algebraic reconstruction technique) [86], SIRT (simultaneous iterative reconstruction technique) [87, 88] and SART (simultaneous algebraic reconstruction technique) [89] and statistical approaches such as the *adaptive statistical iterative reconstruction* or ASIR [90] are based on iterative optimization algorithms. In order to result in a successful and artifact-reduced reconstruction, all of these techniques call for an extensive knowledge of the system matrix of the imaging procedure. Since the computation of such a matrix on a voxel basis has yet to be comprehensively solved in case of PCCT, algebraic and statistical iterative approaches are still of only limited use for phase-contrast CT.
A different approaches, based on a regularized optimization was recently introduced for general signal recovery and initially applied for the reconstruction of magnetic resonance images. Independent from the type of data acquisition Donoho et al. demonstrated that under certain conditions it is possible to recover artifact-free images from a drastically smaller number of samples, using a measurement-reconstruction technique called compressed sensing.
This method utilizes the natural sparsity of tomographic images or the sparsity of tomographic images after a suitable transformation as prior information in an optimization process, in order to fully reconstruct images from a number of measurement samples heavily violating the Nyquist-Shannon criterion.
The aim of the presented work is to investigate the performance of a compressed sensing based reconstruction on phase-contrast computed tomography. Simulation studies [91, 92] and other previous publications [92–94] could already demonstrate the general feasibility of iterative, compressed sensing based approaches on PCCT data. However, these studies mostly assessed data generated from very simple objects, obtained with highly brilliant synchrotron radiation. Consequently, the presented work pursues a comprehensive assessment of simulated and measured data. Against the background of future dose-limited clinical applications of PCCT with the help of CS, a special focus was lain on the applicability to tomograms, acquired with a conventional X-Ray source.
After a detailed introduction of the underlying theory in Chapter 3, Chapter 7 will present results on the performance of the CS-based reconstruction. Subsequently, the histogram constrained approach, initially introduced for undersampled MRI is adapted for PCCT. Its performance is assessed in comparison to CS and as a combination of both constraints. Evaluated data comprises numerical simulations, as well as *in vitro* measurements on mouse specimen from both a synchrotron and a conventional X-Ray tube source.

2 Technical Basics

2.1 Nuclear magnetic resonance

Nuclear magnetic resonance (NMR) was first described and measured by Isidor Rabi [95] in 1938. For his experiments on NMR in molecular beams Rabi was awarded with the Nobel Prize in Physics in 1944. Rabi's experiments were carried out on liquids and solids by Felix Bloch and Edward Purcell in 1944, which was again awarded with the Nobel Prize in Physics in 1952.
Magnetic resonance imaging employs the effect of NMR to measure the spatial distribution of hydrogen atoms (^{1}H) and other nuclei of non-zero nuclear spin. Hence, the following chapter aims to briefly describe the basic physical principles necessary to understand the content of this work. For a more extensive description of NMR physics the interested reader may be referred to the standard text books [96–99].

2.1.1 Nuclear spin and magnetic moment

In 1922 Otto Stern and Walther Gerlach performed an experiment, which is today often used to illustrate basic principles of quantum mechanics such as quantization and how the process of measuring affects the system being measured. In the *Stern-Gerlach* experiment a beam of silver particles is sent through an inhomogeneous magnetic field and subsequently detected on a photographic plate in order to measure the particles' deflection. While classical mechanics predicts an isotropic distribution of angular momenta among the particles, resulting in a homogeneous pattern on the photographic plate, the experiment actually showed two distinct deflection distribution directions. This result constitutes the first evidence of a quantized intrinsic angular momentum, termed *spin*.
The total angular momentum of an atomic nucleus comprises the spins and orbital angular momenta of the single nuclei and is termed the nuclear spin $\mathbf{I}$ of the nucleus. In case of an odd number of protons and/or neutrons the nuclear spin is non-zero and can be derived from the magnetic moment via:

$$\mu = \gamma \mathbf{I}. \tag{2.1}$$

The gyromagnetic ration γ is a characteristic constant for every nucleus and takes with $\gamma = 2.675 \cdot 10^8 \frac{rad}{Ts}$ for the hydrogen atom the highest known value for stable nuclides. Within a comprehensive quantum mechanical description nuclear spin and magnetic moment are expressed as operators $\widehat{\mathbf{I}} = \left(\widehat{I}_x, \widehat{I}_y, \widehat{I}_y\right)$ and $\widehat{\boldsymbol{\mu}}$. For $\widehat{\mathbf{I}}$ the following commutator relationships hold:

$$[\widehat{\mathbf{I}}^2, \widehat{I}_i] = 0 \tag{2.2}$$

$$[\widehat{I}_i, \widehat{I}_j] = \mathrm{i}\hbar\epsilon_{ijk}\widehat{I}_k \qquad i \in \{x, y, z\} \tag{2.3}$$

If z is used as quantization axis, the eigenvalue equation for $\widehat{\mathbf{I}}$ reads as

$$\widehat{\mathbf{I}}^2 |I, m\rangle = I(I+1)\hbar^2 |I, m\rangle \tag{2.4}$$

$$\widehat{I}_z |I, m\rangle = m\hbar |I, m\rangle . \tag{2.5}$$

The quantum numbers m and I characterize the eigenfunctions $|I, m\rangle$, where $m \in \{-I, -I+1, \cdots I-1, I\}$ and I can take values $0, 1/2, 1, 3/2, 2, \ldots$. In case of the proton $I = \frac{1}{2}$ and m is 2-fold degenerate.

External magnetic fields

NMR is based on the interaction of a magnetic moment with an external magnetic field, described by the Hamiltonian

$$\widehat{H} = -\widehat{\boldsymbol{\mu}}\mathbf{B} = -\gamma\widehat{\mathbf{I}}\mathbf{B} \tag{2.6}$$

In case of a stationary magnetic field in z-direction ($\mathbf{B} = (0, 0, B_0)$) $\widehat{H}$ can be simplified to

$$\widehat{H} = -\gamma\widehat{I}_z B_0. \tag{2.7}$$

Since $\widehat{H}$ and $\widehat{\mathbf{I}}$ have common eigenvectors, the eigenvalues E_m of the according Schroedinger equation can be computed using the eigenstates from Equ. 2.4.

$$\widehat{H} |I, m\rangle = E_m |I, m\rangle \tag{2.8}$$

$$E_m = -\gamma\hbar m B_0 \tag{2.9}$$

Equation 2.9 shows that an external magnetic field causes the $(2I+1)$-fold degeneracy regarding m in a field-free setting to split up (see Fig. 2.1). This phenomenon is termed Zeeman-effect and the emerging energy levels are separated by an energy gap

$$\Delta E_m = E_m - E_{m-1} = \gamma\hbar B_0 = \hbar\omega_0 \tag{2.10}$$

proportional to the Larmor frequency

$$\omega_0 = \gamma B_0. \tag{2.11}$$

Transitions between these energy levels can be induced by applying a rotating electromagnetic field of frequency $\nu_0 = \frac{\omega_0}{2\pi}$ polarized orthogonal to the field direction. In case of hydrogen (spin-$\frac{1}{2}$) and a typical field of $B_0 = 1.0$T the transition Larmor frequency is $\nu_0 = 42.6$MHz.

2.1.2 Macroscopic magnetization

In the commonly used semi-classical description of NMR the macroscopic magnetization $\mathbf{M}$ yields the measurement variable in an NMR experiment. Let N be a certain number of nuclear spins in a volume V in thermal equilibrium. Then, the occupation probabilities p_m of the Zeeman levels are computed using Boltzmann statistics:

$$p_m = \frac{e^{-E_m/kT}}{\sum_{m=-I}^{I} e^{-E_m/kT}} = \frac{e^{\gamma\hbar m B_0/kT}}{\sum_{m=-I}^{I} e^{\gamma\hbar m B_0/kT}} \tag{2.12}$$

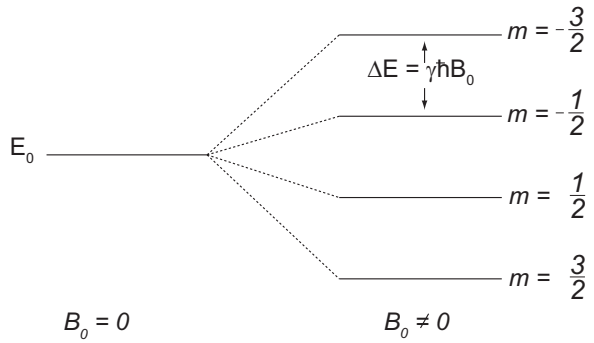

Figure 2.1: Zeeman levels of a nucleus with spin quantum number $I = 3/2$ in an external magnetic field of flux density $\vec{B_0}$. The energy gap of two arbitrary, neighboring energy levels is $\Delta E_m = \gamma\hbar B_0 = \hbar\omega_0$.

In case of hydrogen Equ. 2.12 yields a ratio of $p_{\frac{1}{2}} - p_{-\frac{1}{2}} \approx 10^{-6}$ at body temperature (T= 310K) and a field strength of $B_0 = 1.5$T. While this ratio is very small, the high abundance of hydrogen in biological tissue accounts for a measurable macroscopic magnetization

$$\mathbf{M} = \frac{1}{V}\sum_{i=1}^{N}\langle\widehat{\boldsymbol{\mu}}_{\boldsymbol{i}}\rangle = \frac{1}{V}\sum_{i=1}^{N}\gamma\left\langle\widehat{\mathbf{I}}_i\right\rangle. \tag{2.13}$$

Since the expectation values of the x- and y-component of the nuclear spin are cancelled out (see Fig. 2.2), the macroscopic magnetization is aligned with the external magnetic field. In thermal equilibrium its maximal or equilibrium value M_0 is:

$$M_0 = \frac{N\gamma\hbar}{V}\sum_{m=-I}^{+I} m p_m = \frac{N\gamma\hbar}{V}\frac{\sum_{m=-I}^{+I} m e^{\frac{m\hbar\omega_0}{kT}}}{\sum_{m=-I}^{+I} e^{\frac{m\hbar\omega_0}{kT}}} \tag{2.14}$$

Since $kT \gg \gamma\hbar B_0$ the first-order Taylor series approximation for high temperatures is applicable resulting in:

$$M_0 \approx \frac{N}{V}\frac{I\left(I+1\right)\gamma^2\hbar^2}{3kT}B_0 \tag{2.15}$$

Hence, M_0 is proportional to the local spin density $\frac{N}{V}$ and γ^2. Consequently, due to its high abundance and gyromagnetic ratio when compared to other nuclei with non-zero spin (e.g. ^{23}Na, ^{13}C, ^{31}P and ^{19}F), hydrogen yields the a superior nucleus for NMR experiments.

2.1.3 Temporal evolution of magnetization

Using the Hamiltonian form Equ. 2.6 and the summation in Equ. 2.13 one can derive the temporal evolution of the magnetization of an ensemble in an arbitrary field $\mathbf{B}(t)$ resulting in

$$\frac{d\mathbf{M}(t)}{dt} = \mathbf{M}(t) \times \gamma\mathbf{B}(t). \tag{2.16}$$

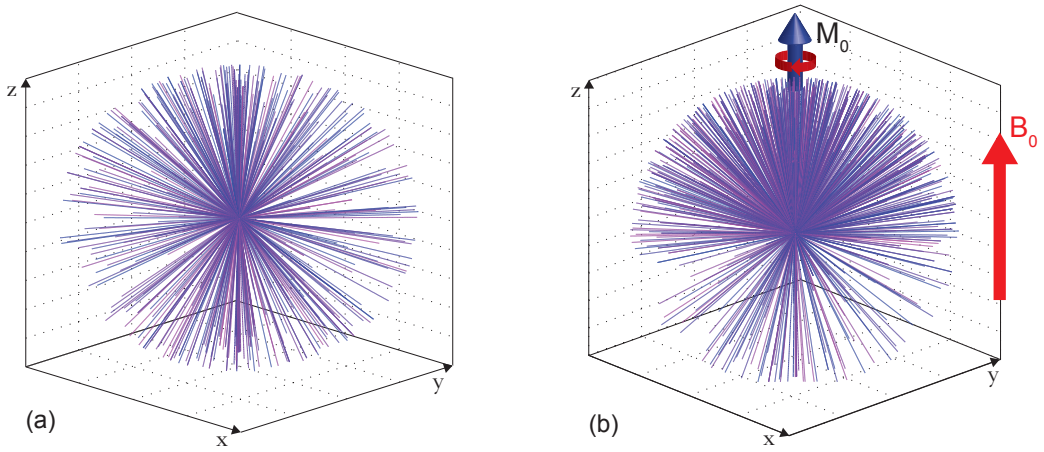

Figure 2.2: (a) Distribution of the expectation values of a spin-1/2 ensemble without an external magnetic field. Spins are orientated randomly with a uniform distribution over directions. (b) In a magnetic field B_0 a certain degree of alignment along the direction of the external field is established, resulting in a macroscopic magnetisation, precessing about the direction of B_0. (Image adapted from [100])

namely Euler's equation of motion known from classical mechanics. Its solution describes a precessing motion of $\mathbf{M}$ about the direction of $\mathbf{B}(t)$ with a frequency ω which reads:

$$\left|\frac{d\mathbf{M}(t)}{dt}\right| = \gamma\,|\mathbf{B}(t)|\,|\mathbf{M}(t)|\sin(\alpha) = \omega\,|\mathbf{M}(t)|\sin(\alpha). \tag{2.17}$$

Here, α denotes the angle between $\mathbf{B}(t)$ and $\mathbf{M}$. In case of a static magnetic field in z-direction $\mathbf{B}(t) = (0, 0, B_0)$ ω equals the Larmor frequency ω_0 (cf. Equ. 2.11).

2.1.4 Radio frequency excitation

The angle α in Equ. 2.17 can be altered by applying a radio frequency (RF) pulse, which is equivalent to superposing $\mathbf{B}(t) = (0, 0, B_0)$ with a temporal dependent magnetic field $\mathbf{B_1}(t)$. The RF-field with amplitude B_1 and frequency ω_1 has to be polarized orthogonally to the axis of $\mathbf{B}$:

$$\mathbf{B}_1(t) = B_1(\cos(\omega_1 t), \sin(\omega_1 t), 0) \tag{2.18}$$

Substituting $\mathbf{B}_1$ in Equ. 2.16 results in a time dependent total field:

$$\frac{d\mathbf{M}(t)}{dt} = \gamma\mathbf{M}(t) \times (B_1\cos(\omega_1 t), B_1\sin(\omega_1 t), B_0) \tag{2.19}$$

In order to simplify the considerations it is convenient to introduce a transformation from the stationary laboratory system (x, y, z) in a coordinate system rotating with the frequency ω_1 ($x' = x\cos(\omega_1 t) + y\sin(\omega_1 t)$, $y' = -x\sin(\omega_1 t) + y\cos(\omega_1 t)$, $z = z'$), in which $\mathbf{B_1}$ is stationary aligned with the x'-axis. The simplified equation of motion in the rotating systems reads:

$$\frac{d\mathbf{M}(t)}{dt} = \gamma\mathbf{M}(t) \times (B_1, 0, B_0 - \frac{\omega_1}{\gamma}) = \gamma\mathbf{M}(t) \times \mathbf{B}_{eff} \tag{2.20}$$

In compliance with Equ. 2.16 now the macroscopic magnetization vector describes a precessing motion about the axis of the effective magnetic field $\mathbf{B_{eff}} = (B_1, 0, B_0 - \frac{\omega_1}{\gamma})$ with frequency $\omega_{eff} = \gamma \|\mathbf{B_{eff}}\|$.
If $\omega_1 = \gamma B_0$ the RF-field oscillates in resonance with the Larmor frequency and $\mathbf{B_{eff}} = (B_1, 0, 0)$ in x'-direction. The irradiation with an RF-field of duration t_p causes the magnetization $\mathbf{M}$ to rotate about an angle α orthogonal to x'. The so called flip angle α is computed via:

$$\alpha = \gamma B_1 t_p \tag{2.21}$$

Hence, the flip angle is adjusted with the amplitude or the duration of the irradiated RF-pulse, which is referred to as α-pulse (most commonly $\frac{\pi}{2}$- or π-pulse). The underlying physical effect is based on the transition of energetic states from the lower to the higher Zeeman level.
After the RF-pulse is turned off the induced transversal magnetization $M_{xy} = M_0 \sin\alpha$ is precessing with frequency ω_0 about the z-axis in the laboratory system.

2.1.5 Relaxation

While the considered situation so far describes an ideal system, in reality, due to molecular and chemical exchange processes, nuclei and their respective magnetic moment are in constant thermal motion. The statistical nature of this motion causes an additional, locally fluctuating magnetic field which in turn induces changes in the macroscopic magnetization known as relaxation.

Spin-lattice relaxation Spin-lattice relaxation denotes the effect of the longitudinal magnetization recovery after the application of an RF-pulse. The component of the aforementioned additional magnetic field perpendicular to B_0 induces - similar to the RF-field - transitions between the Zeeman levels. This mechanism allows the spin system to receive or dispense energy in order to return back to the Boltzmann distribution of energy states. The so called lattice, hence, all neighboring atoms and molecules serve as an energy reservoir. The parameter characterizing this process in termed the longitudinal relaxation time T_1:

$$M_z(t) = M_0(1 - \exp\left(\frac{-t}{T_1}\right)) \tag{2.22}$$

Spin-spin relaxation The term spin-spin relaxation denotes the decay of transversal magnetization M_{xy} over time. The coherence of single spins after the RF excitation is irreversibly lost primarily due to dipole-dipole interactions. Here, the transversal magnetization decays exponentially characterized by the parameter T_2.

$$M_{xy} = M_0 \exp\left(\frac{-t}{T_2}\right) \tag{2.23}$$

The component of the locally fluctuating field parallel to B_0 is affecting the precession frequency of the spin, inducing dephasing, hence loss in phase coherence and as a consequence the loss of macroscopic magnetization in the transversal plane.

In addition to the effect of the introduced fluctuating fields, in real systems imperfections in the homogeneity of the B_0-field induce an even faster dephasing of the transversal magnetization. Similar to fluctuating fields this static field causes an additive phase and the so called T_2'-relaxation process. In contrary to the T_2-relaxation the static nature of the interfering field offers the possibility to reverse the dephasing within a specially designed NMR experiment.
The comprehensive effect of dephasing in the x-y-plane is described as T_2^* decay:

$$\frac{1}{T_2^*} = \frac{1}{T_2} + \frac{1}{T_2'} \tag{2.24}$$

Bloch equations

A mathematical description of the described processes was first proposed by Felix Bloch [101]. Bloch introduced a set of empirically found equations for the temporal evolution of the magnetization vector:

$$\frac{dM_x}{dt} = \gamma(\mathbf{M} \times \mathbf{B})_x - \frac{M_x}{T_2} \tag{2.25}$$

$$\frac{dM_y}{dt} = \gamma(\mathbf{M} \times \mathbf{B})_y - \frac{M_y}{T_2} \tag{2.26}$$

$$\frac{dM_z}{dt} = \gamma(\mathbf{M} \times \mathbf{B})_z + \frac{M_0 - M_z}{T_1} \tag{2.27}$$

In case of a simple $\alpha = \pi/2$ experiment and a perfectly homogeneous field $\mathbf{B} = (0, 0, B_0)$ the solutions of Equ. 2.25 - 2.27 can be easily expressed in the laboratory system:

$$\begin{aligned} M_{xy}(t) &= M_{xy}(0)e^{i\omega_0 t}e^{-\frac{t}{T_2}} \\ M_z(t) &= M_0 - (M_0 - M_z(0))e^{-\frac{t}{T_1}} \end{aligned} \tag{2.28}$$

The M_{xy} component is the relevant measurement variable in an NMR experiment. After the excitation the transversal magnetization precesses with frequency ω_0 about the z-axis, while its amplitude is decaying with T_2. The oscillating magnetic field is simultaneously detected by an adjacent coil and represents the actual physical quantity detected in NMR and MRI.

Experimental design

The collection of existing NMR and MRI experiments is very extensive. However, the source of the measured signal can basically be assigned to two different effects. The gradient-echo and the spin-echo experiment are essentially the basis of all other experimental designs and shall be introduced very briefly.

Radio frequency echo As mentioned in Subsection 2.1.5 the dephasing effect due to static inhomogeneities in the B_0-field is reversible. The experiment used to compensate for the signal loss on the basis of an RF-pulse is termed spin-echo experiment [102].
After a $\frac{\pi}{2}$-pulse (Fig. 2.3(a)) coherent spins in the transversal plane start to dephase (Fig. 2.3(b)) due to the local difference in the magnetic field. Consequently, after a certain time TE/2 two spins with a frequency difference of $\Delta\omega$ experience a phase difference of $\Delta\Phi = \Delta\omega\frac{TE}{2}$. The application of a π-pulse (Fig. 2.3(c)) causes the phase difference to change sign to $\Delta\Phi = -\Delta\omega\frac{TE}{2}$. Since the local precession frequencies are unaffected by the 180° inversion pulse, after another time period of $TE/2$ the dephasing effect is compensated and all spins are rephased ($\Delta\Phi = 0$) forming a so called spin echo (Fig. 2.3(d)). Hence, the characteristic time parameter TE for this experiment is termed the echo time.

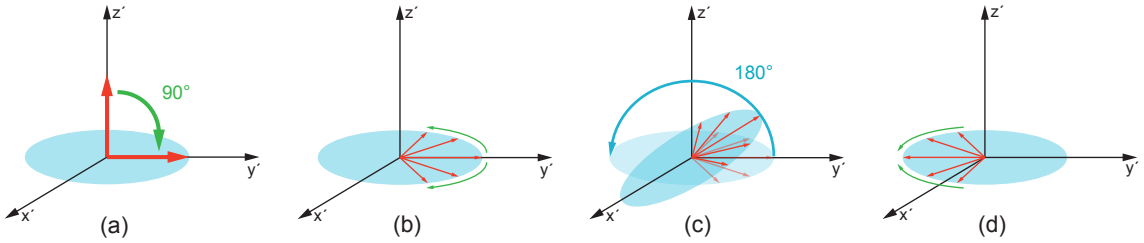

Figure 2.3: Generating a spin-echo: (a) The RF-excitation tips the longitudinal magnetization into the $x'y'$-plane. (b) Due to inhomogeneities in the magnetic field coherent spins dephase over time. (c) The application of a 180°-pulse after the half echo time (TE) inverts the spins' phases, hence the dephasing effect. (d) After another $TE/2$ the spins are fully rephased forming the spin-echo signal.

Gradient-echo The gradient-echo experiment differs from the spin-echo in regard to the flip angle α, which is usually below 90° and the absence of a 180° inversion pulse. As there is no rephasing due to inversion, the spin signal has to be generated in a different manner. As already explained, local differences in the magnetic field cause spin ensembles to dephase. This effect can be employed in order to artificially induce an echo signal. By applying a linear magnetic field gradient a controlled dephasing of the spin system can be obtained. Vice versa, the application of an inverse gradient after a certain time period causes the spins to rephase and form an echo signal. In contrary to the RF-echo experiment, static magnetic field inhomogeneities are not compensated for in a gradient-echo experiment. Hence, the signal decay is depending on T_2^* rather than T_2 alone.

2.2 Magnetic resonance imaging

So far, the signal measured in the described experiments is obtained from the whole measurement object. However, to incorporate NMR as an imaging tool, crucial spatial information is missing. In the early 1970's Lauterbur [4] and Mansfield [3] developed a technique that opened the possibility to imprint spatial information in the acquired NMR signal. The basic underlying concept is to linearly vary the main magnetic field, in order to generate spatially dependent Larmor frequencies. The following chapter is intended to give a brief overview of the theoretical background MRI is based on. For a more extensive overview on MR imaging techniques and sequences the standard text books may be recommended [98, 103].

2.2.1 Field gradients and spatial encoding

When applying a gradient filed $\mathbf{G}$ of the form

$$\mathbf{G} = \frac{\delta B_z}{\delta x}\mathbf{e}_x + \frac{\delta B_z}{\delta y}\mathbf{e}_y + \frac{\delta B_z}{\delta z}\mathbf{e}_z = G_x\mathbf{e}_x + G_y\mathbf{e}_y + G_z\mathbf{e}_z \tag{2.29}$$

the total magnetic field and hence the Larmor frequency of the affected spins becomes spatially dependent:

$$\omega(\mathbf{x}, t) = \gamma B_z(\mathbf{x}, t) = \gamma(B_0 + \mathbf{x}\mathbf{G}(t)) \tag{2.30}$$

The Bloch equations taking the linearly varying field into account formulate as:

$$\frac{dM_x}{dt} = \gamma\mathbf{x}\mathbf{G}(t)M_y - \frac{M_x}{T_2} \tag{2.31}$$

$$\frac{dM_y}{dt} = -\gamma\mathbf{x}\mathbf{G}(t)M_x - \frac{M_y}{T_2} \tag{2.32}$$

$$\frac{dM_z}{dt} = \frac{M_0 - M_z}{T_1} \tag{2.33}$$

resulting in the following solutions:

$$M_{xy}(t) = M_{xy}(t_0)e^{i2\pi\Phi(\mathbf{x}(t),t)}e^{-\frac{t}{T_2}} \tag{2.34}$$

$$M_z(t) = M_z(t_0)e^{-\frac{t}{T_1}} + M_0\left(1 - e^{-\frac{t}{T_1}}\right) \tag{2.35}$$

The applied gradient field generates a local phase shift $\Phi(x(t), t)$ depending upon the amplitude and the duration of the local gradient amplitude:

$$\Phi(\mathbf{x}(t), t) = -\gamma\int \mathbf{x}\mathbf{G}(t')dt' + \Phi(0) = -\mathbf{k}(t)\mathbf{x} + \Phi(0) \tag{2.36}$$

Here, $\mathbf{k}(\mathbf{t})$ denotes the spatial frequency

$$\mathbf{k}(t) = \gamma\int_0^t \mathbf{G}(t')dt'. \tag{2.37}$$

Since the measured signal S is proportional to the total excited transversal magnetization, the outcome of an experiment is computed by integrating Equ. 2.34. Neglecting relaxation effects the integration yields:

$$S(\mathbf{k}(t),t) \propto \int_V M_{xy}(\mathbf{x},t_0)e^{-i2\pi\mathbf{k}(t)\mathbf{x}}d\mathbf{x} = \mathcal{FT}(M_{x,y}) \tag{2.38}$$

Equation 2.38 shows that the signal acquired in the spatial frequency domain or k-space is proportional to the Fourier transform ($\mathcal{FT}$) of the spatial distribution of the transversal magnetization M_{xy}. The latter can therefore be calculated by applying the inverse $\mathcal{FT}$ on the measured k-space:

$$M_{xy}(\mathbf{x}) \propto \int S(\mathbf{k}(t),t)e^{i2\pi\mathbf{k}(t)\mathbf{x}}d\mathbf{k} = \mathcal{FT}^{-1}(S(\mathbf{k}(t),t)) \tag{2.39}$$

By employing three orthogonal linear gradients separately it is possible to manipulate every single component of k and imprint spatial encoding in all three dimensions. The acquisition of single values in the three dimensional k-space generates a hologram, whose $\mathcal{FT}$ results in a spatially resolved image in real space. The trajectory through k-space is determined by the temporal geometry of the applied gradient and conventionally describes a Cartesian grid. Imaging parameters such as resolution or field of view in real space are defined by Δk, the interval between two adjacent k-space points and by the maximal spatial frequency k_{max} (cf. Subsection 2.2.3).

2.2.2 Slice selection

In order to acquire parallel slices of the whole volume the most commonly used method is to only excite spins of a certain spatial extent in z-direction (see Fig. 2.4). This is realized by inducing a linear magnetic field gradient (G_z) along the intended slice direction. As a consequence, the precession frequency ω of spins is varying in the direction of the gradient

$$\omega(z) = \gamma(B_0 + G_z z), \tag{2.40}$$

which in turn only leaves certain spins in resonance with the excitation pulse. More precisely, if an RF-pulse with central frequency ω is applied with a bandwidth $\Delta\omega$ simultaneously with the gradient G_z only spins within the slice Δz get excited (see Fig. 2.4(a)). In the described case the Bloch equations have to be solved for the simultaneous application of an RF-pulse and a magnetic field gradient. Let the peak of the excitation pulse be at time $t = 0$ and suppose the gradient starts at time $t = T/2$ with the same duration T as the RF-pulse. Then, for small flip angles ($M_z(t) \approx M_0$) an approximated solution can be found [103]:

$$M_{xy}(T/2,z) = i\gamma M_0 e^{-i\gamma z G_z \frac{T}{2}} \int_{-T/2}^{T/2} B_1(t)e^{i\gamma z G_z t}dt \tag{2.41}$$

One can draw several important conclusions from this result:

- The gradient causes dephasing of the transversal magnetization over the selected slice (first exponential term), hence loss of signal. The application of a second oppositely poled gradient of same amplitude and a duration $t = T/2$ compensates for the dephasing effect (cf. Fig. 2.4b).

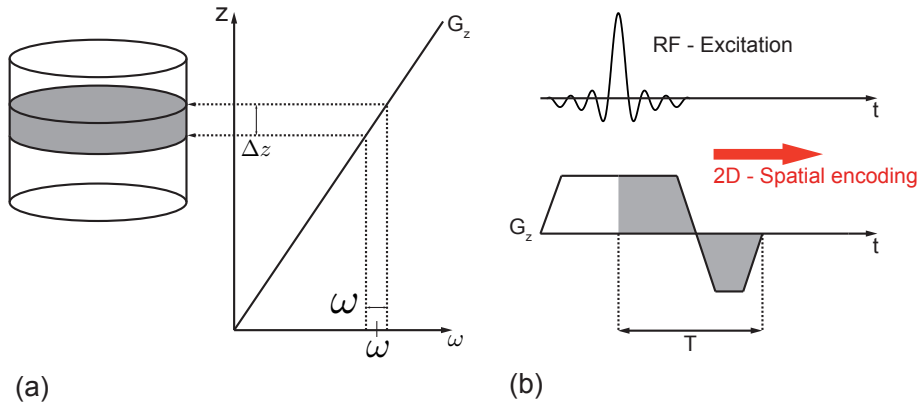

Figure 2.4: Slice selection. (a) A gradient in z-direction, applied during the excitation pulse irradiated with a central frequency of ω_S and bandwidth $\Delta\omega$ results in a selective excitation of spins contained in Δz (b) Schematic visualization of the sequence design. The gradient G_z is switched on at the start of the excitation pulse and switched off when the excitation is complete. In order to compensate for the dephasing due to the first gradient a second gradient of opposite sign and half duration is applied.

- The slice profile of M_{xy} is the Fourier transformed envelope of the RF-pulse (B_1) and depends similar to the slice thickness on the frequency spectrum of the RF-pulse:

$$\Delta z = \frac{\Delta\omega}{\gamma G_z} \tag{2.42}$$

  Consequently, the slice thickness is reduced by increasing the gradient amplitude and/or decreasing the RF-pulses bandwidth. Theoretically, the application of a *sinc*-pulse (the $\mathcal{FT}$ of a rectangular profile) induces the excitation of a rectangular magnetization profile.

$$B_1(t) = B_1 sinc\left(\frac{\pi t}{\tau_S}\right) \tag{2.43}$$

$$\Delta\omega = \frac{1}{\tau_S} \tag{2.44}$$

  Here, τ_s is the first cross point of the *sinc* function. However, since the measurement time in MRI is limited, the *sinc*-pulse has to be cropped to a certain duration, which causes imperfections in the rectangular profile.

After slice selection the acquired signal is encoded in two dimensions resulting in the signal expression:

$$S(k_x, k_y, t) \propto \int_x \int_y M_{xy}(t_0) e^{-i2\pi(k_x x + k_y y)} dxdy \tag{2.45}$$

Consequently, 2D-tomography can be realized with only two encoding direction.
Nevertheless, the slice selection step can be substituted by exciting the whole measurement

volume and encoding in three dimensions, resulting in real 3D-tomography. However, the additional encoding step causes the measurement time to further increase and consequently shows for instance more motion artifacts in the image.

2.2.3 Discrete k-space sampling and the Nyquist limit

While the acquired signal (Equ. 2.38) and its Fourier transformation (Equ. 2.39) are continuous, sampling in reality is a discrete operation. That is, the signal detected by the detection coil and consequently the k-space are sampled after time intervals Δt or k-intervals $\Delta k = \gamma G \Delta t$, over a non-infinite interval. Consequences following from discrete sampling can be observed on a simplified one-dimensional measurement.
Mathematically, discrete sampling is described by the multiplication of the continuous signal with an equidistant comb or sampling function:

$$\Delta k \sum_{n=-N/2}^{N/2} \delta(k - n\Delta k) \tag{2.46}$$

yielding the measured signal

$$S_m(k) = S(n\Delta k) = \Delta k \sum_{n=-N/2}^{N/2} S(k)\delta(k - n\Delta k), \tag{2.47}$$

where $S(k)$ is the known expression for the infinite, continuous signal (see Equ. 2.38).
Equivalent to the continuous case, in reality a discrete version of the Fourier transform is used to reconstruct the real space image from k-space data, resulting in

$$M(x) = \Delta k \sum_{n=-N/2}^{N/2} S(n\Delta k) e^{i2\pi n \Delta k x} \tag{2.48}$$

The discrete $\mathcal{FT}$ has a periodical spectrum, repeating with the sampling frequency. It is apparent from Equ. 2.48 that $e^{i2\pi n\Delta k x}$ is unchanged for any n if x is changed according to:

$$x \to x + \frac{1}{\Delta k} \tag{2.49}$$

Consequently, the reconstruction shows identical copies of the magnetization distribution, centered around x_i in image space.
If the sampled signal contains components with a frequency higher than half the maximal sampling frequency, these repeating copies overlap, which is termed aliasing. Higher frequencies components in the signal can not be resolved and are interpreted as lower frequencies, hence reconstructed as a so called folding artifact. To avoid this effect the following condition has to be satisfied when setting up the NMR experiment:

$$x_{min} = -\frac{2}{\Delta k} \leq x \leq \frac{2}{\Delta k} = x_{max} \tag{2.50}$$

$$FOV = \frac{1}{\Delta k} \tag{2.51}$$

Equation 2.50 is one formulation of the Nyquist theorem [67, 104] and basically states, that the measured object has to be contained in the set up field of view (FOV).
Let $k_{max} = \frac{N\Delta k}{2}$ be the highest frequency sampled in k-space. Then the image space resolution can be expressed as:

$$\Delta x = \frac{FOV}{N} = \frac{1}{k_{max}} \tag{2.52}$$

Consequently, in order to resolve small objects in image space, k-space has to be sampled to high frequencies, thus at a great distance from the k-space center ($\mathbf{k} = 0$). Vice versa, the center of k-space contains most of the contrast information of low frequency. Since only small encoding gradients are applied close to the k-space center, almost no dephasing is caused leading to a maximum in signal intensity.

2.2.4 Sequence design

Figure 2.5 demonstrates a schematic sequence design for a basic spin-echo sequence. The single rows depict the series of RF-pulses, gradients in x-, y- and z-direction and the acquired signal. More generally, the encoding directions are commonly referred to as slice-, phase and readout-direction. After the slice selective 90°-excitation both phase (green) and frequency (blue) gradients encode the measurement volume in two dimensions, setting the k-value to maximum magnitude (cf. gradients I) for the first measurement (cf. gradients II). Subsequently, the generated echo is sampled by scanning through frequencies $k_{min} : \Delta k : k_{max}$.

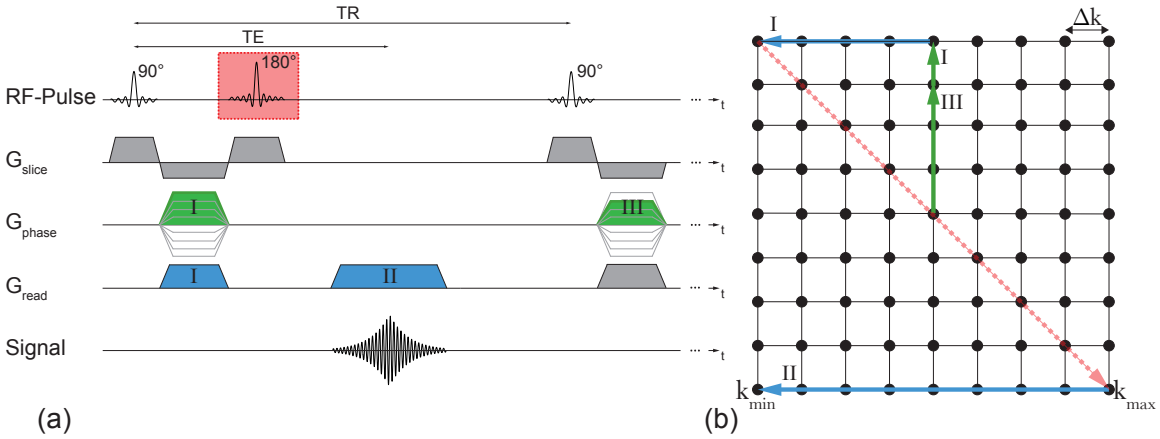

Figure 2.5: (a) Schematic structure of a basic spin-echo sequence. After the slice selective 90°-pulse the spin ensemble is phase encoded and selectively inverted by the 180°-pulse. After the echo time TE has passed, the signal is acquired while frequency encoding. If necessary the measurement is repeated after the repetitions time TR. (b) Influence of the applied gradients on the k-space position. The first gradients (I) set phase and frequency to a minimum, while the second gradient (II) shifts through all frequencies during the data acquisition.

2.2.5 Image contrast

One of the most prominent benefits of MRI is its flexibility in image contrast. The information possibly contained in the image comprises blood volume, the diffusion coefficient, blood flow, fat content and several other quantities. Primary parameters influencing the contrast of the reconstructed image are already apparent in the basic signal expression of for instance the spin-echo sequence:

$$S(t) = M_0 \cdot \left(1 - \exp\left(\frac{-TR}{T_1}\right)\right) \cdot \exp\left(\frac{-TE}{T_2}\right) \tag{2.53}$$

While the repetition time (TR) and the echo time (TE) are parameters set by the MRI user, the spin-echo signal in Equ. 2.53 depends upon three physical quantities: The introduced relaxation times T_1 and T_2, and the proton density contained in the equilibrium magnetization M_0. The extend to which the image contrast is defined by a certain parameter can be influenced via the set measurement parameters. An image contrast primarily defined by for instance the T_1 time is called T_1-weighted. Following the principle parameter settings for the three main image weightings are presented.

- Long TR ($TR > 5 \cdot \mathrm{T}_1$) and TE as short as possible:
  The longitudinal magnetization is completely relaxed after the chosen TR for all contained tissue types. Additionally, due to the short TE almost no transversal relaxation occurs causing the acquired signal to almost exclusively depend upon the proton density of the measurement volume.

- Long TR and long TE ($TE \approx \mathrm{T}_2$):
  Again the longitudinal magnetization is completely relaxed. However, due to the long echo time, T_2 relaxation appears, which makes areas of different T_2 times separable. Hence, the image is T_2-weighted.

- Short TR ($TR \approx \mathrm{T}_1$) and TE as short as possible:
  Due to differences in T_1 the signal recovers to a different degree in different areas during the set repetition time. Together with a short echo time, prevent a T_2 bias of the image contrast, the resulting measurement is primarily T_1-weighted.

Figure 2.6 presents the different parameter weightings on an MRI slice through the human brain.

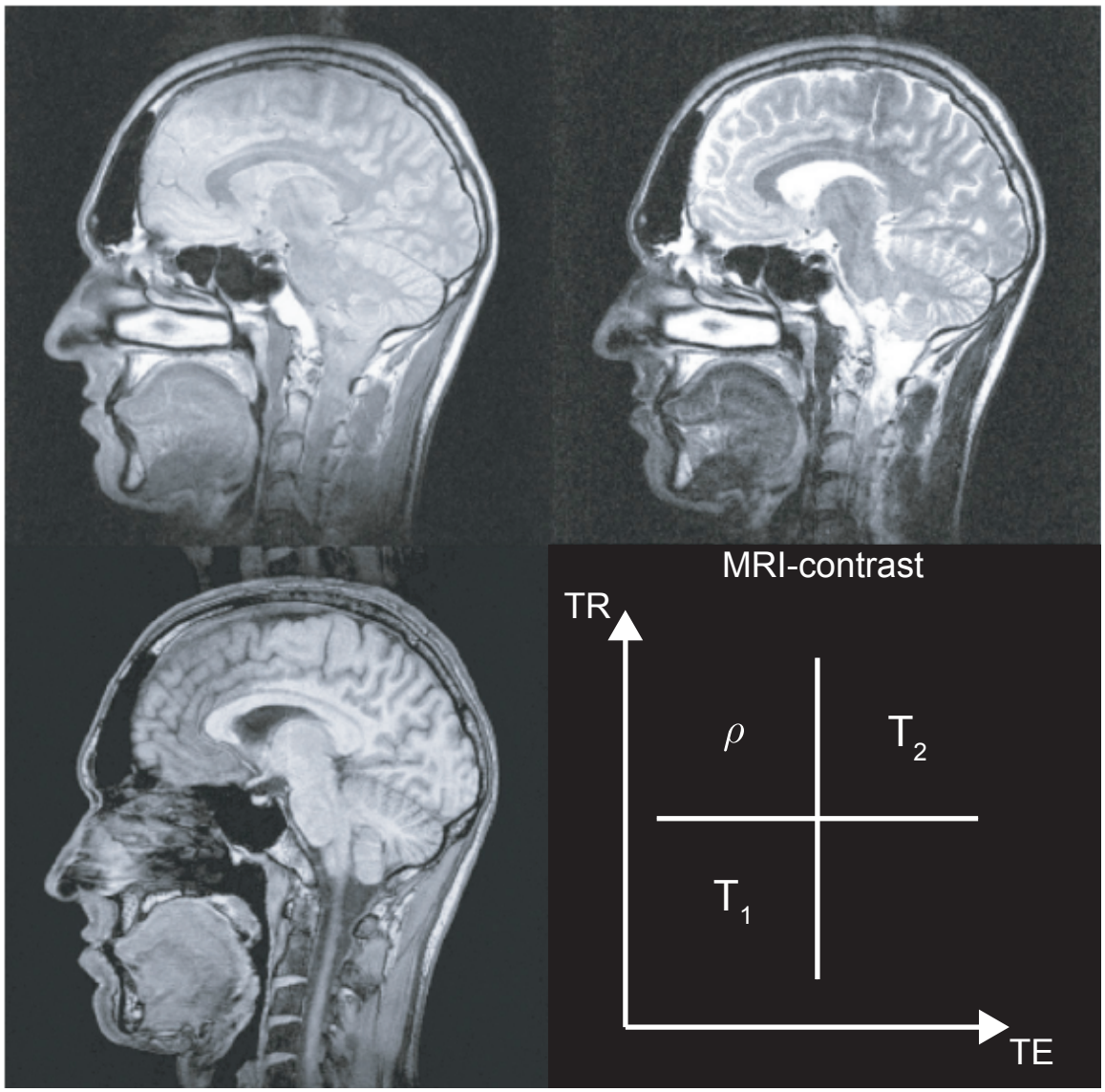

Figure 2.6: Three different weightings in the contrast of MRI: Choosing a long repetition time and a short echo time results in a proton density weighted image. A long TR and long TE generate an image contrast primarily based on differences in T_2. Whereas a short TR and short TE cause the contrast to depend upon the differences in T_1. Image courtesy [105].

2.3 Phase-contrast X-ray computed tomography

Conventional X-ray based computed tomography (CT) is a well-established medical imaging modality [106, 107]. CT generates high-resolution images of strongly absorbing materials, such as bones, based on the difference in the absorption coefficient, resulting in high contrast between bone and soft tissue. However, due to the low absorption cross-section of materials such as soft tissue in biological matter [108], the use of absorption CT is limited or has to be overcome by the use of highly absorbing contrast agents.
While soft tissue is almost transparent to X-ray, the cross-section for elastic scattering of hard X-rays is approximately three orders of magnitude larger than that of absorption. When penetrating tissue, this scattering causes a phase shift of the X-rays depending on the real part of the refractive index, offering the possibility to differentiate between numerous types of tissue.
This fact led to the development of several imaging techniques using X-Ray in order to measure the real part of the refractive index and perform phase-contrast CT (PCCT) [109]. The first approaches on retrieving hard-X-ray phase information on the basis of a double grating set-up was realized 2005, using a synchrotron source a synchrotron source [76, 77, 110]. In the following year a set-up was developed, which achieved phase-sensitive measurements on a lab-based system without the necessity of a high-brilliant X-rays source [78]. Recent studies [81, 83, 84] could already demonstrate the feasibility of grating-based PCCT as a *in vivo* imaging device. At the same time great progress was made on the improvement of the underlying imaging technique [111–114].
The following sections are intended to briefly introduce the major concepts behind grating-based phase-contrast CT measurements.

2.3.1 X-ray interaction with matter

Similar to optical light the interaction of X-rays with matter depends upon the wavelength of the electromagnetic wave penetrating the material. Effects accompanying X-rays travelling through matter can be calculated from the complex index of refraction $n = 1 - \delta + i\beta$. In general refraction effects comprise both absorption and a phase shift (see Fig. 2.7).

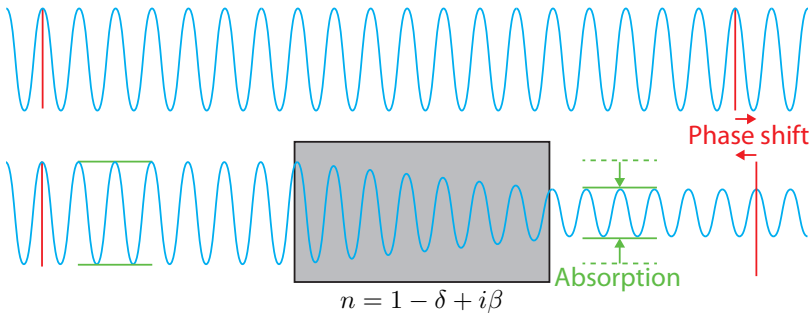

Figure 2.7: Propagation of an electromagnetic wave passing a medium of refractive index $n = 1 - \delta + i\beta$. While penetrating the medium the amplitude of the initial wave is reduce and its phase is shifted when compared to an undisturbed wave.

The degree to which X-rays are attenuated in media, as indicated by green lines in Fig. 2.7, can be computed from the imaginary part β of the refractive index n given by

$$\beta = \frac{\rho_a \sigma_a}{2k}. \tag{2.54}$$

Here ρ_a is the atomic number density and σ_a denotes the absorption cross-section. The intensity loss due to absorption is derived from the *Lambert-Beer* law

$$\begin{aligned} I &= I_0 e^{-2\beta k x} \\ &= I_0 e^{-\mu x} \end{aligned} \tag{2.55}$$

where $k = |\mathbf{k}| = 2\pi/\lambda$ is the length of the wave vector and x is the penetration depth.
In addition to intensity loss due to absorption, X-rays experience a shift in the waves phase relative to a wave traveling through vacuum. The phase shift can be calculated from the real part δ of the refractive index given by

$$\delta = 2\pi \rho_a Z r_0 / k^2. \tag{2.56}$$

Here, Z is the atomic number and $r_0 = 2.82 \times 10^{-5} \mathring{A}$ denotes the Thomson scattering length. The phase shift $\Delta\Phi$, indicated by red lines in Fig. 2.7 can be computed via

$$\Delta\Phi = \delta \mathbf{k} \cdot \mathbf{r}. \tag{2.57}$$

2.3.2 Grating interferometer

As described in the previous section, when coherent X-rays travel through the sample, amplitude and phase of the propagating wave-front change. Figure 2.8 demonstrates in particular the effect when a parallel wave-front is travelling through an object purely affecting the X-ray's phase Φ.
Refraction in the non-parallel part of the penetrated sample causes a deviation in the propagation direction of the wave-front.
The concept of phase-contrast imaging is to retrieve the sample's index of refraction by measuring the angular deviation α. In order to detect even small changes in the propagation direction a grating interferometer is used, detecting α from the transverse displacement of the generated interference pattern.
The phase grating (G_1) acts as a phase mask, imprinting a periodical phase modulation onto the incoming wave front. Due to the Talbot effect [115] these phase modulations are translated into a linear periodic intensity fringe pattern, which spatially repeats along the direction perpendicular to the optical axes and parallel to the lines of G_1. The Talbot effect states that a wave-front will repeat its initial shape after a certain propagation distance, known as Talbot distance.
The precise detection of the spatial position of this interference pattern calls for a very high resolution of the employed detector, posing a huge challenge on the hardware. Alternatively, however, the interference pattern can be scanned step-by-step via a second grating (G_2 in Fig. 2.8). G_2 is designed in such manner, that its absorbing lines have the same periodicity and orientation as the Talbot fringes created by G_1, and is placed directly in front of the

detector at a distance d (Talbot distance) from the grating G_1. In order for the detector to sample one full period of the intensity modulation, the grating G_2 is scanned in steps over one grating period, resulting in an oscillating signal as a function of the grating position (cf. Fig. 2.9).
Note that the detected intensities in the top and bottom pixel of the detector in Fig. 2.8 are the same, although the according phases are different. Hence, the measurement if solely sensitive to a *differential phase shift*. The transverse shift of the interference pattern is given by:

$$S(x) = \frac{\lambda}{2\pi} \frac{\delta\Phi(x)}{\delta x} d \tag{2.58}$$

and the angular deviation by

$$\alpha \approx \frac{S(x)}{d} \tag{2.59}$$

The intensity $I(k, l, x)$ measured by the detector in pixel (k, l) oscillates as a function of the transverse direction x. Changes in this oscillation, induced by phase objects in the X-ray beam are the basis of the experiment and the phase contrast. In addition to conventional absorption images this method allows for the extraction of so called dark field images [116], as well as phase sensitive data. The presented work will concentrate on the reconstruction of phase contrast images.

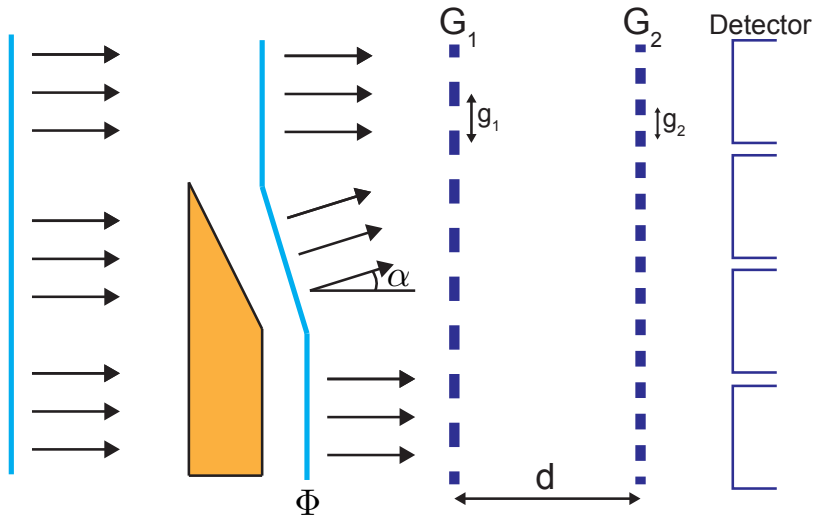

Figure 2.8: Phase shift of an X-ray wave-front penetrating an object. The wedge shaped part of the object introduces a phase shift, hence refraction of the wave-front by an angle α. This phase shift causes a detectable transverse shift of the interference pattern introduced by grating $G1$. The analyzer grating $G2$ is used to sample the interference pattern and identify differential phase shifts. Image adapted from [117]

2.3.3 Data analysis and image processing

The extraction of the introduced three-fold information is performed by fitting the following expression [116] for the intensity of the interference pattern pixel-wise to the measured data:

$$I(k,l,r_n) = \sum_i a_i(k,l)\cos[i\frac{2\pi}{p_2}r_n + \phi_i(k,l)] \tag{2.60}$$
$$\approx a_0(k,l) + a_1(k,l)\cos[\frac{2\pi}{p_2}r_n + \phi_1(k,l)]$$

Here a_i are the amplitude coefficients, Φ_i are the corresponding phase coefficients and p_2 is the periodicity of G_2. After one reference measurement (^{r}) without the sample and one with the sample within the beam (^{s}) measurement quantities can be defined as described in the following paragraph.
Figure 2.9 presents the three-fold alterations to the intensity pattern when penetrating the measured object. The average intensity value a_0^s corresponds to the transmission of X-ray

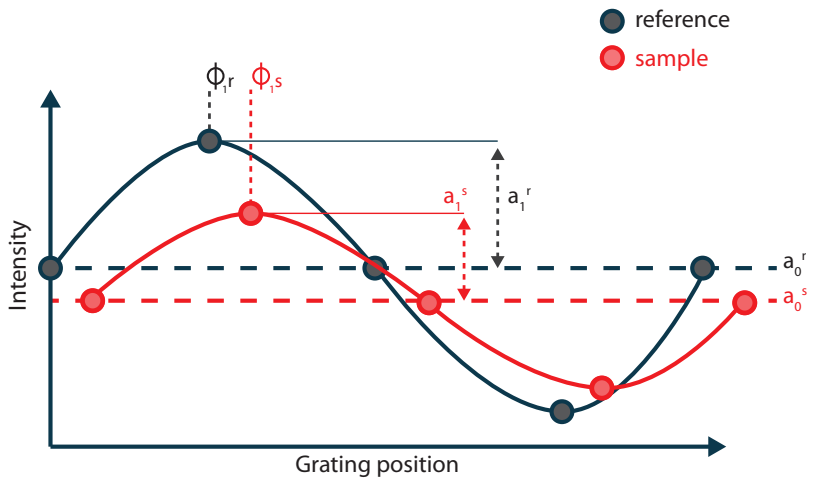

Figure 2.9: Signal characteristics at different positions of grating $G2$ without an object in the X-ray beam (reference) and after the X-ray penetrated the object (sample). The sample introduces alterations in the average intensity a_0, the amplitude of the modulation a_1 and the phase Φ when compared to the reference.

travelling through the sample. Together with the reference value a_0^r one can define the relative absorption $a_0 = a_0^s/a_0^r$. Similarly, the phase parameters $\phi_1^{r/s}$ allow for the definition of the relative phase shift $\phi_1 = \phi_1^s - \phi_1^r$. The third quantity, namely the dark field contrast, is derived from the reduction in amplitude of the first order Fourier coefficients, hence a_1^s and a_1^r. This decrease in visibility due to the specimen yields information about the scattering power of structure within the sample. Images with contrast computed from all three mentioned quantities are depicted in Fig. 2.10.
Again, when focusing on the phase shifting properties, the transverse pattern shift is given by:

$$S(k,l) = \phi_1(k,l)\frac{g_2}{2\pi} \tag{2.61}$$

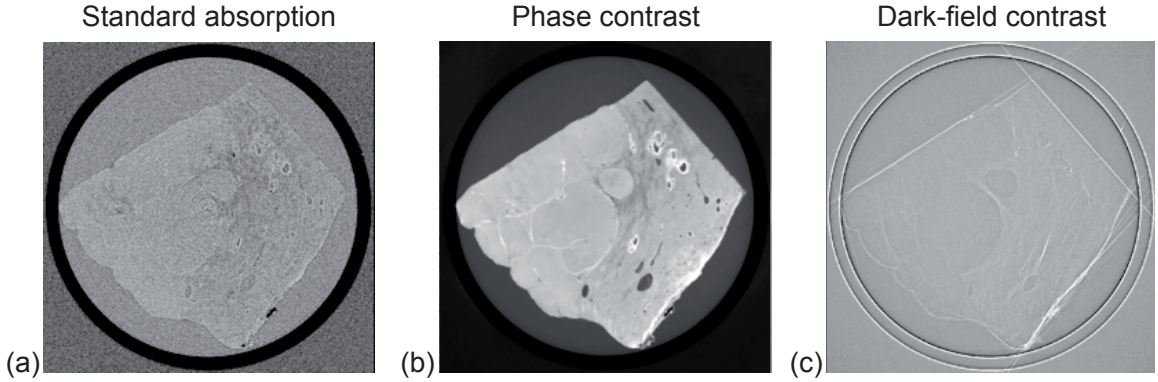

Figure 2.10: Three-fold contrast extracted from one PCCT measurement set of a human liver sample [118].

Using Equ. 2.58, the differential phase shift introduced by the penetrated object can be derived as

$$\frac{\delta\Phi(k,l)}{\delta x} = \frac{g_2}{\lambda}\frac{\phi_1(k,l)}{d}, \tag{2.62}$$

where λ is the X-ray wavelength, d is the distance between G_1 and G_2 and g_2 denotes the grating period of G_2.
Thus, in order to perform one single phase contrast CT measurement in one direction, the following steps are necessary:

- Perform reference scan without the sample at several (at least three) grating positions.
- Use the same geometry and grating steps as for the reference scan to image the actual sample. Both the reference and sample measurement result in a data matrix size of (*detector size*)×(*number of grating steps*)
- Perform pixel-wise fitting or Fourier analysis of the detected intensity modulation to extract the parameter ϕ_1
- Calculate the differential phase via Equ. 2.62

How the differential phase information is reconstructed into an image whose contrast is determined by the real part of the refractive index is subject of the following section.

2.3.4 Tomographic Reconstruction

The term tomography in X-ray CT refers to the approach of imaging the sample from different directions, in order to reconstruct volumetric information from the combination of all one-dimensional scans (projections). Mathematically, the projection of a sampled object $f(x, y)$ is expressed as the Radon transform [107]

$$\mathcal{P}(y', \theta) = \mathcal{R}f(y', \theta) = \int_{-\infty}^{\infty} f(x', y')dx', \tag{2.63}$$

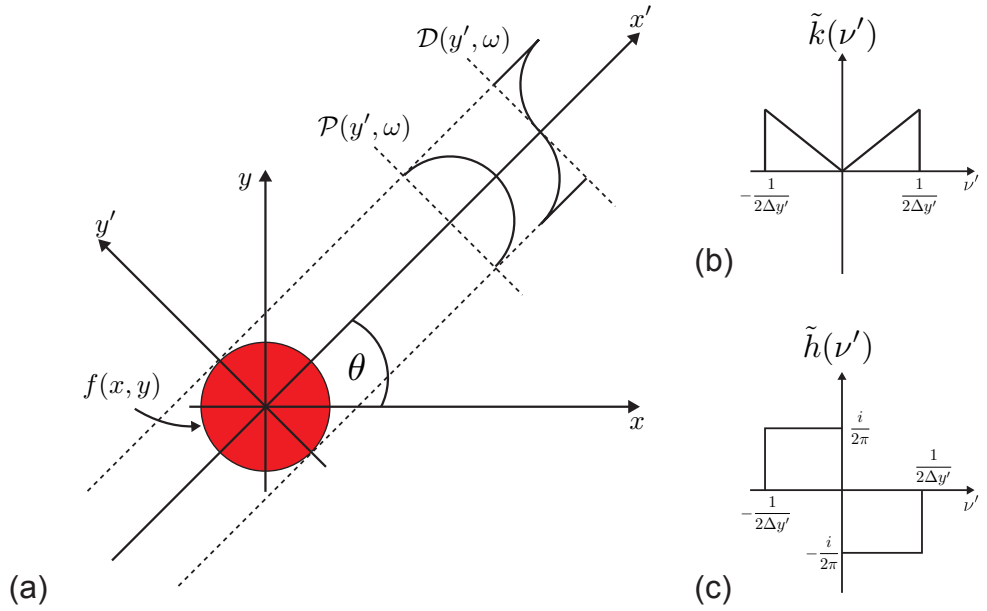

Figure 2.11: (a) Acquisition of the object $f(x,y)$ at a single angle θ resulting in a conventional absorption projection $\mathcal{P}(y',\theta)$ and in a differential phase shift projection $\mathcal{D}(y',\theta)$. (b) Ram-Lak filter function used in the reconstruction of absorption based X-ray tomography. (c) Imaginary valued Hilbert filter, employed to reconstruct differential phase-shift projections. (Images adapted form [85])

where x' and y' denote a coordinate system which is rotated by an angle θ. $f(x,y)$ either describes the distribution of the imaginary part β or the real part δ of the complex refractive index n, corresponding to absorption and refraction, respectively.
In conventional CT the reconstruction from a set of projections $\mathcal{P}(y',\theta)$, is realized via filtered back projection (FBP) [107, 119]. Essentially, the collection of acquired projections (also referred to as *sinogram*) are ran back through the image (hence back projection), constructively interacting at the actual sample position. Additional information smeared over the image is filtered out in a separate step. Mathematically this operation can be formulated as the convolution back projection integral

$$f(x,y) = \int_0^\pi \mathcal{FT}^{-1}[\mathcal{P}(y',\theta) * |\nu'|]d\theta, \tag{2.64}$$

where $\mathcal{FT}^{-1}$ is the inverse Fourier transform. The filtering process is realized by the convolution operator $*$ of the projection $\mathcal{P}(y',\theta)$ with the ramp filter function $|\nu'|$ (cf. Fig. 2.11):

$$\mathcal{P}(y',\theta) * |\nu'| = \mathcal{FT}(\mathcal{P}(y',\theta)) \cdot \mathcal{FT}(|\nu'|) \equiv \tilde{\mathcal{P}}(y',\theta)\tilde{k}(\nu') \tag{2.65}$$

While this approach is valid to reconstruct standard absorption images, as stated before PCCT yields *differential* phase information. Since performing a basic integration along y' is generally error-prone, due to the unknown integration constant, a different approach was

chosen to translate the differential information. Similar to the filtering step when reconstructing absorption data, a complex valued filter (see Fig. 2.11) can be used to reconstruct the actual phase shift

$$\tilde{h}(\nu') = \frac{1}{2}\pi i \; sgn(\nu'). \tag{2.66}$$

Thus, the procedure for tomographic reconstruction of phase shift data in real space is the same as the procedure to reconstruct absorption data, except for a different filter, called the Hilbert filter [85]:

$$f(x,y) = \int_0^\pi \mathcal{FT}^{-1}[\tilde{\mathcal{D}}(y',\theta)\tilde{h}(\nu')]d\theta, \tag{2.67}$$

2.3.5 Experimental set-up

Figure 2.12 displays the experimental assembly used for PCCT (see also [78–80]). It comprises a source grating G_0, a phase grating G_1 and an analyzer absorption grating G_2. The first grating (G_0) is only embedded into the measurement arrangement, when a conventional, non-coherent X-ray source is used. As explained before, grating based interferometry calls for high coherence of the X-rays. G_0 basically acts as a aperture mask, splitting the initial beam into an array of small line sources, each of very small extent, hence sufficiently coherent.

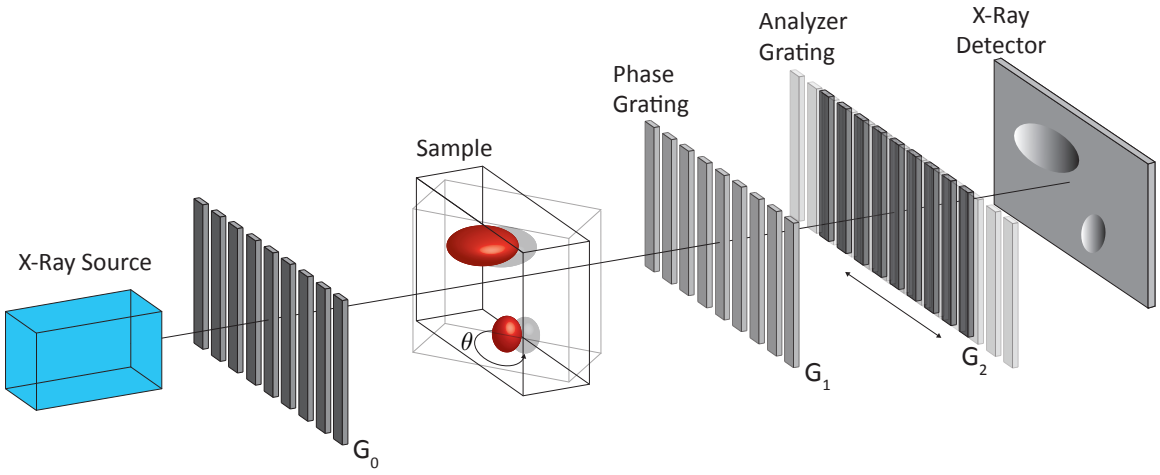

Figure 2.12: Schematic image of a grating-based phase-contrast CT set-up. Behind the source grating G_0, the X-ray beam penetrates the sample. Subsequently the phase grating imprints a phase modulation onto the incoming wave front, which is sampled by the detector employing G_2 as an analyzer grating.

While the phase grating G_1 is purely constructed from Si, G_0 and G_2 are silicon/gold absorption gratings [120]. When choosing the grating periods g_1, g_2 and g_3 the following considerations have to be taken into account. Starting from G_1, while the demand for the detector resolution might decrease with an increasing grating period, the necessary distance between grating and detector would simultaneously increase. This, in turn calls for a higher

transverse coherence of the X-ray beam. Typically, the grating period g_1 is in the order of a few micrometers.
Since the interference pattern after G_1 has half the period of the grating generating it and the analyzer grating period has to match the pattern, g_2 is given by g_1:

$$g_2 = \frac{g_1}{2}. \tag{2.68}$$

As already mentioned the grating G_0 is added to the set-up if the X-ray source is incoherent, which is the case for conventional X-ray tubes. It can be derived that the size of the beam source should not exceed s,

$$s = \frac{g_2 L}{2d}, \tag{2.69}$$

where L is the distance between source and grating G_1 and d is the distance between G_1 and G_2. For a conventional source to satisfy Equ. 2.69, G_0 splits the original beam in several single coherent sources. The grating period g_0 should be set to

$$g_0 = g_2 \frac{L}{d}. \tag{2.70}$$

3 Theory and Methods

3.1 Radial sampling of k-space

As described in Section 2.2 MR measurements acquire data in Fourier space, or k-space. Here, the respective k-values, hence the sampling points in k-space are defined by the applied frequency and phase encoding gradients during the measurement sequence. Conventionally, gradients are generated in order for k-space sampling points to be distributed on an equidistant Cartesian grid. Gradient hardware together with modern reconstruction techniques however allow for k-space trajectories to differ from the standard Cartesian sampling schemes. Most prominent among those alternative sampling strategies is the radial sampling trajectory [4], offering advantages in motion and flow artifact suppression, efficient use of gradients and fast acquisition. Since the standard reconstruction via Fourier transform ($\mathcal{FT}$) is not applicable to non-Cartesian data, the application of radial sampling calls for a different reconstruction approach.
The following chapter is intended to provide a comprehensive overview on the radial sampling scheme, its variations and on the reconstruction of non-Cartesian data. After the connection between CT and radial MRI is explained (cf. Subsection 3.1.1), the basic radial sampling scheme in MRI is introduced (cf. Subsection 3.1.2), followed by common variation in radial sampling (cf. Subsection 3.1.4). Subsequently in Subsection 3.1.3, the Nyquist sampling condition will be adapted to the case of radial sampling. The final sections will concentrate on the conventional reconstruction of polar k-space data (cf. Subsections 3.1.5 and 3.1.5), introduce the concept of the point spread function (cf. Subsection 3.1.6) and discuss advantages and disadvantages of radial sampling in MRI (cf. Subsection 3.1.7).

3.1.1 The Fourier slice theorem

While the physical basis of X-ray computed tomography and magnetic resonance imaging are of completely different nature, the structure of the acquired raw data in case of radial MRI are very closely related. In CT data is acquired as a projection, hence the radon transform $\mathcal{R}$ of the object, whereas MRI samples the Fourier domain during data acquisition. The relationship between both domains is described by the Fourier slice theorem (FST) [107].
The FST states that the one-dimensional Fourier transform of a function's projection is equivalent to one data line in a polar k-space generated from the source function (see Fig. 3.1). This statement shall be derived in short for the 2D case.

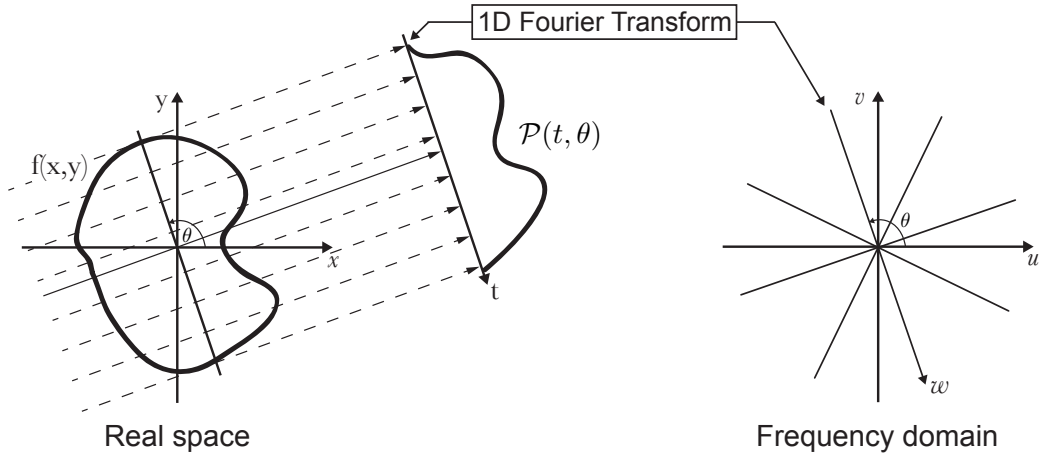

Figure 3.1: The one-dimensional $\mathcal{FT}$ of the Radon transform $\mathcal{P}(t,\theta)$ of an object $f(x,y)$ is equivalent to a radial line at angle θ in frequency domain.

Let $f(x,y)$ be the object function, subject to the measurement. Then

$$\mathcal{FT}f(u,v) = \int_{-\infty}^{\infty}\int_{-\infty}^{\infty} f(x,y)e^{-i2\pi(ux+vy)}dxdy \tag{3.1}$$

is the two-dimensional Fourier transform of the object function. Let

$$S(w,\theta) = \int_{-\infty}^{\infty} \mathcal{P}(t,\theta)e^{-i2\pi wt}dt \tag{3.2}$$

denote the 1D $\mathcal{FT}$ of the projection $\mathcal{P}$ (see Equ. 2.63).
The simplest example in this context is given for the angle $\theta = 0$. The 2D Fourier transform of $f(x,y)$ then is given by

$$\mathcal{FT}f(u,0) = \int_{-\infty}^{\infty}\int_{-\infty}^{\infty} f(x,y)e^{-i2\pi ux}dxdy = \int_{-\infty}^{\infty}\left[\int_{-\infty}^{\infty} f(x,y)dy\right]e^{-i2\pi ux}dx. \tag{3.3}$$

Comparing Equ. 3.3 with Equ. 2.63 it is evident that the expression in brackets complies the definition of the Radon transform at $\theta = 0$:

$$\mathcal{P}(x,0) = \int_{-\infty}^{\infty} f(x,y)dy \tag{3.4}$$

Consequently, by substituting expression 3.4 in Equ. 3.3 it follows:

$$\mathcal{FT}f(u,0) = S(u,\theta). \tag{3.5}$$

This expression of course is equivalent to the above statement and defines the interconnection between CT and radial MRI.
From this result one can deduct, that concepts for data analysis and reconstruction are interchangeable between CT and MRI via a simple 1D Fourier transform. Consequently, in the following most of the conclusions will be formulated in regards to k-space sampling, but can equivalently be applied to CT imaging.

3.1.2 Sampling pattern for radial MRI

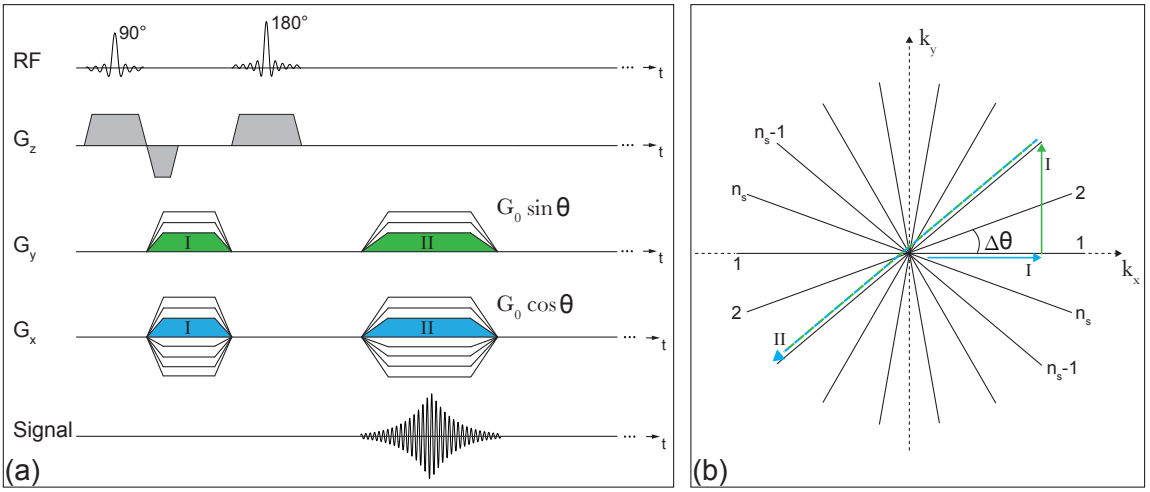

Figure 3.2: (a) Schematic representation of a typical MR sequence used to radially sample k-space (b) on the basis of a conventional spin-echo sequence. The x- and y-gradient are applied simultaneously, resulting in frequency encoding in both direction, setting k-values according to $k_x = k_r \cos\theta$ and $k_y = k_r \sin\theta$.

The basic sequence design to generate a polar sampling grid in k-space can be deduced starting from the central line in a Cartesian grid. As illustrated in Fig. 2.5(b) a rectilinear row in k-space is acquired by applying a dephasing gradient and subsequently engaging a readout gradient in the opposite direction while acquiring data. As evident from Fig. 3.2 and Fig. 3.3 the polar k-space line or spoke at the angle $\theta = 0$ is equivalent to the central line in the Cartesian case. The same holds for the gradient G_0 to be applied in both cases. The gradient design for subsequent spokes with $\theta \neq 0$ can be derived from the standard transformation between Cartesian and polar coordinates:

$$x = r\cos\theta \qquad y = r\sin\theta. \tag{3.6}$$

Hence, adapted for the k-space formulation and gradients in both directions:

$$\begin{aligned} k_x &= k_r\cos\theta & k_y &= k_r\sin\theta \\ G_x &= G_0\cos\theta & G_y &= G_0\sin\theta. \end{aligned} \tag{3.7}$$

Figure 3.2 depicts a basic spin-echo sequence with polar sampling of k-space. For a given readout it is possible to cover both positive and negative k-values. Hence, the angle interval can be limited to $\theta = [0 : \Delta\theta : \pi - \Delta\theta]$. The number n_s of uniformly spaced angles covered by the sampling is limited by the chosen number of different gradients:

$$n_s\Delta\theta = \pi \tag{3.8}$$

Once Δk_r (the distance between two sampling points on the same spoke) is chosen, the sampling density solely depends upon the number of radial spokes. The condition for the

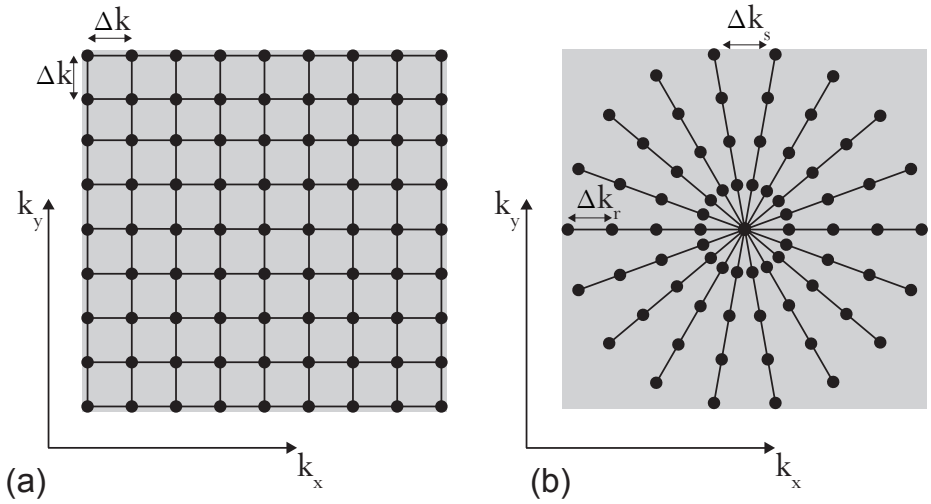

Figure 3.3: (a) Conventional Cartesian k-space with k-values at positions k_x and k_y separated by Δk. (b) Geometry of a polar k-space grid. The distance between single k-values is measured either in radial (Δk_r) or azimuthal direction (Δk_s).

k-space to be fully sampled as introduced for Cartesian sampling in Subsection 2.2.3 can be adapted to the polar case, which is subject to the next Subsection.

3.1.3 Nyquist condition for polar k-space sampling

The limitations regarding sampling density to match the Nyquist condition have to be reformulated for polar coordinates. The difference in the definition of sampling density when compared to Cartesian sampling completely changes the nature of aliasing in the image. Step sizes between k-space sampling points are, as illustrated in Fig. 3.3(b) denoted Δk_r in radial direction and Δk_s is the azimuthal distance between k-space points of the same k_r and neighboring spokes.
As already mentioned the spoke at $\theta \neq 0$ is equivalent to the central line in the Cartesian case. If the base resolution, hence the resolution defined by k_r is considered to be equivalent to the sampling density of a fully sampled Cartesian k-space, the distance Δk_r of two adjacent k-space points of the same spoke satisfies Equ. 2.50. Thus, for the radial k-space to be fully sampled also the maximal distance Δk_s between k-space points of different spokes has to be less or equal to Δk_r (see Fig. 3.3).
From basic geometry (see also [121]) one can derive

$$\Delta k_s \approx \frac{\pi}{n_s} k \leq \frac{\pi}{n_s} k_{max}. \tag{3.9}$$

Substituting k_{max} with

$$k_{max} = \Delta k_r \frac{n_r}{2}, \tag{3.10}$$

n_r being the number of radial sampling points per spoke, it follows

$$\Delta k_s \leq \frac{\pi}{n_s} \Delta k_r \frac{n_r}{2}. \tag{3.11}$$

Thus, for Δk_s to match Δk_r, hence to fully sample k-space, the number of spokes has to be set according to

$$n_s \geq \frac{\pi}{2} n_r. \tag{3.12}$$

Equivalent to the Nyquist condition in Cartesian sampling (Equ. 2.51) the radial step size is dictated by

$$\Delta k_r = 1/\mathrm{FOV}. \tag{3.13}$$

Consequently, the minimum number of radial sampling points is

$$n_r = \frac{2k_{max}}{\Delta k} \geq 2k_{max}\mathrm{FOV}. \tag{3.14}$$

Therefore the total number of points necessary to radially sample k-space according to Nyquist is

$$n_r n_s \geq 2\pi(k_{max}\mathrm{FOV})^2. \tag{3.15}$$

One major attribute regarding radial k-space sampling is the non-uniform sampling density. As evident from Fig. 3.3 the density of k-space samples varies inversely with the distance from the origin. The dense coverage of small k-values, hence low frequencies implies relatively more information about large image structures and image contrast, resulting in an image of higher signal to noise ration when compared to the Cartesian case.
However, when calculating the number of k-values in a Cartesian k-space with base resolution $n_x = n_y = n_r$

$$n_x n_y \geq 4(k_{max}FOV)^2 \tag{3.16}$$

it becomes clear from Equ. 3.15 ($2\pi > 4$) that there are more sampling points in a circle of diameter FOV than in a square of side length FOV. This fact results in a slightly higher acquisition time in radial sampling. An answer to this issue is discussed in Subsection 3.1.7. Again, equivalent to Cartesian sampling, undergoing the Nyquist limit results in aliasing or undersampling artifacts. However, undersampling artifacts in a polar acquisition scheme are of completely different nature when compared to Cartesian sampling. While the effect on the image and the differences of aliasing in both cases are discussed in section 3.2 it is worth noting at this point that radial undersampling artifacts have an impact on the whole image and appear as streak-like structures in the image. In the following the degree of undergoing the Nyquist limit will be referred to as undersampling or reduction factor $R = n_s/n'_s$, where n_s is the number of spokes according to Nyquist and n'_s is the actually acquired number of spokes.

3.1.4 Sampling scheme variations

In addition to the radial sampling scheme as illustrated in Fig. 3.2, in which consecutive spokes are sampled in a linear order, several sophisticated strategies have been developed [122–126] to sample k-space even more efficiently. While the number of spokes is always dictated by the Nyquist limit, the order of spokes can be design flexible. These sequence design variations are briefly introduced in this chapter.

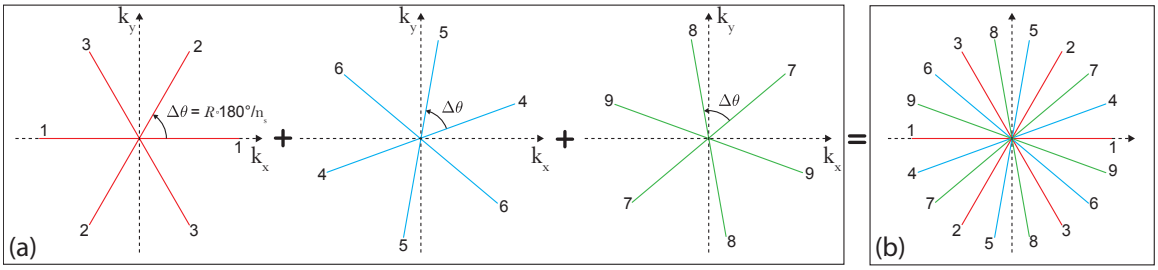

Figure 3.4: Interleaved sampling strategy. (a) Consecutive k-spaces are sampled at angles $R \cdot \theta$, starting at $\theta_1 = 0, \theta, 2\theta, \ldots, R\theta$. Subsequently the single k-spaces can be reconstructed to single images. (b) Alternatively, the composition of R consecutive k-spaces can be employed to reconstruct an images using the R-fold number of spokes.

Interleaved sampling and sliding window

A very flexible sampling strategy especially for dynamic radial acquisitions is the interleaved sampling scheme. In a series of angles $\theta = [0{:}\Delta\theta{:}\pi{-}\Delta\theta]$ where the number of spokes n_s satisfies Equ. 3.12, instead of acquiring subsequent spokes in a linear order, the according angles are reassigned in R groups of fewer but still uniformly distributed spokes. That is, the first n_s/R spokes are acquired at angles $\theta = [0 : R\Delta\theta : \pi - R\Delta\theta]$ (see Fig. 3.4(a)), while the second series starts from $\Delta\theta$ and so forth until all R groups of angles are acquired and the total number of spokes equals n_s (see Fig. 3.4(b)).
Since every set of angles out of the R acquired, covers k-space uniformly, R independent images of high temporal resolution, however R-times undersampled, can be reconstructed. Additionally, it is possible to calculate so called composite data using R consecutive k-spaces. By combining those R data sets, one can generate raw data satisfying Equ. 3.12. A reconstruction from the composite data results in an image of decreased temporal resolution but circumvents any undersampling artifacts.
Since in a dynamic acquisition the sequence of groups of angles is repeated over the duration of the measurement, starting again with $\theta = [0 : R\Delta\theta : \pi{-}R\Delta\theta]$ after the R-th time frame, the R consecutive k-space trajectories for composition can be chosen arbitrarily from the set of acquired data. This fact is used to reconstruct a continuous composite image *sliding* over the temporally resolved data acquisition. The reconstruction method is therefore termed *sliding window* reconstruction.

Golden angle

As introduced in the Subsection 3.1.2 and defined by Equ. 3.8, the angles between spokes covering a radial k-space are spaced uniformly between $\theta = 0$ and $\theta = \pi - \Delta\theta$. Using this constant angle increment of $\Delta\theta = \pi/n_s$, spokes are temporally succeeded in order to cover the whole k-space (see Fig. 3.5(a)). While this procedure guarantees a uniform coverage of k-space after the acquisition of n_s spokes, sampling points at an earlier point in time are in fact distributed non-uniformly. Recently a novel radial sampling strategy has been

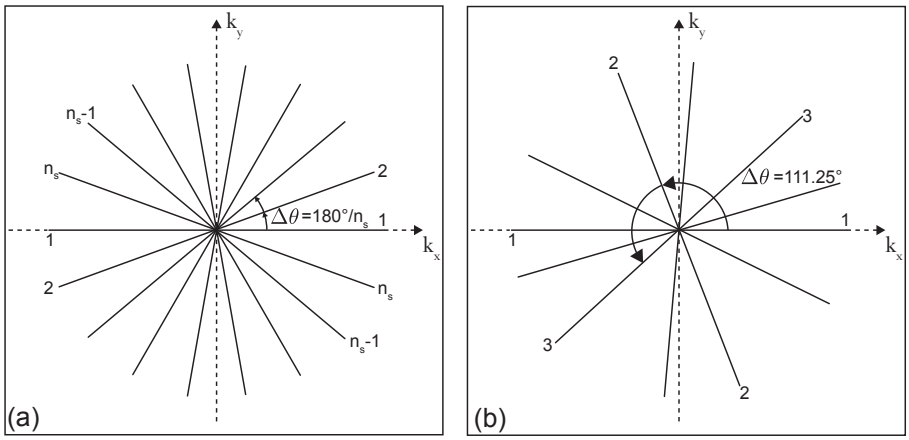

Figure 3.5: (a) Conventional polar k-space alignment, where consecutive spokes are acquired following an angle array in a linear manner. (b) Golden angle radial sampling scheme. Consecutive angles are separated by an angle following the golden ration (111.25°), resulting in a homogeneous coverage of k-space at any point in time.

introduced [127], which guarantees close to uniform coverage at any given point in time during the measurement.
Instead of using the conventional increment, the angle spacing is chosen according to the Golden Ratio (see Fig. 3.5(b))

$$\gamma = \frac{1+\sqrt{5}}{2} \approx 1.62, \tag{3.17}$$

resulting in an angle increment of 111.25°. In contrast to a conventional radial acquisition, during a *golden angle* acquisition every added spoke divides one of the largest azimuthal k-space gaps. Additionally, it can be derived that the maximal number of different angles in a golden ration series is three. Consequently, using a golden angle sampling scheme results in a very even distributions of sampling points over k-space.
Again, when focusing on dynamic acquisitions one feature of golden angle sampling is especially beneficial. Since the coverage of k-space is close to optimal at any given time point of the measurement, the temporal resolution of a dynamic acquisition can be adjusted *a posteriori*. That is, once the measurement is complete, the number of spokes used for the reconstruction of one single image can be chosen arbitrarily. Suppose n_s is the total number of acquired spokes. Then n_s images of high temporal resolution, but poor image quality, or one image without any temporal resolution but high image quality can be reconstructed from the very same measurement. In contrast to the interleaved approach introduced in the previous section, the number of spokes per time frame, hence the extent of the sliding window can be adjusted arbitrarily, even after the measurement.

Bit-reverse sampling

An approach to realize quasi-random radial sampling of k-space with the same benefits as described in the previous section for the golden angle strategy is based on a bit-reverse ordering of uniformly spaced angles [128–130]. While the angle increment is, as in the conventional case set to $\Delta\theta = \pi/n_s$, the order of subsequent spokes is altered (see Fig. 3.6). The term bit-reverse reordering refers to a permutation procedure demonstrated in table 3.1.

Spoke Index	Bits	Bit-Reverse	θ-index
0	000	000	0
1	001	100	4
2	010	010	2
3	011	011	6
4	100	001	1
5	101	101	5
6	110	011	3
7	111	111	7

Table 3.1: Bit-reverse permutation of linear spoke indices 0-7 with base-2 digits.

Similar to the golden angle acquisition, subsequent spokes are evenly distributed over the θ-interval $[0°:\Delta\theta:\pi-\Delta\theta]$, however with a constant increment of $\Delta\theta = \pi/n_s$. Again, after only a few spokes the first estimate of the image can be generated and in dynamic measurements the temporal resolution can be adjusted retrospectively.

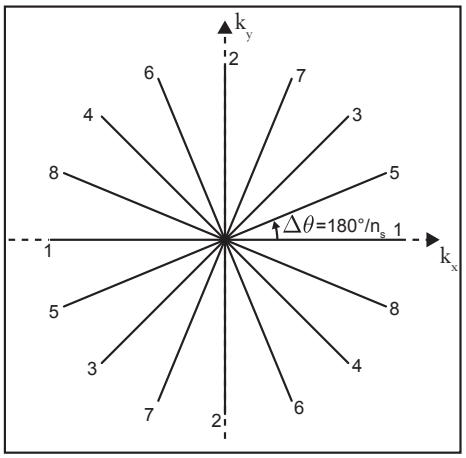

Figure 3.6: Radial sampling scheme in bit-reverse order. Acquisition angles are chosen from a set of equally spaced angels using the order calculated in table 3.1

3.1.5 Conventional Reconstruction of non-Cartesian data

Filtered back-projection

As explained in Subsection 3.1.1 the projection reconstruction or *filtered back-projections* (FBP) as introduced in Subsection 2.3.4 is both applicable for CT and radially acquired MRI. In fact, for a long time FBP has been the only possibility to reconstruct polar k-space data. Applied to MRI raw data, which is acquired in the frequency domain, the convolution filtering step in the FBP (Equ. 2.67) procedure reduces to a multiplication of polar k-space spokes with the ramp filter function $\tilde{k}(\nu)$ (see Fig. 2.11(b)) prior to the back-projection. Subsequently, a 1D $\mathcal{FT}$ is applied to each spoke, transforming k-space into a sinogram, which is reconstructed using the inverse Radon transform.
One major difference between CT and MRI raw data, however, is that data in k-space is complex valued. Consequently, FBP has to be applied separately to both the real and imaginary part of raw data, or as commonly performed in early radial MRI acquisitions, to the magnitude of the raw data. However, when using modern multi-coil arrays for imaging the loss of phase information results in phase artifacts in the reconstructed image. These limitations accompanying FBP, when applied to MRI led to the development of an alternative reconstruction method termed *resampling*.

Resampling method

In MRI the most widely used approach to reconstruct images from k-spaces sampled in a non-Cartesian manner, is realized by resampling data onto a Cartesian grid and subsequent 2D Fourier transform into image space [131]. This idea was first introduced to medical imaging by O'sullivan [132] and further developed by Fessler [35] under the acronym NUFFT (non-uniform fast Fourier transform). The resampling task can by achieved in different ways. The most prominent among those are the so called *grid driven* and the *data driven* approaches [37].
The grid driven approach generates a Cartesian grid with sampling values interpolated from the nearest neighbor non-Cartesian samples. While this method is very simple and easy to implement, one major disadvantage poses the fact that in general not all the non-Cartesian input data is used, resulting in a decreased signal-to-noise ratio (SNR). This problem is avoided in the data driven resampling, described next in more detail.
In simple terms data driven resampling 'smears' each data point over a circle in k-space and subsequently accumulates all contributing spread out data points in Cartesian grid locations. This procedure is commonly referred to as *gridding* or *regridding*.
The smearing or interpolating step is realized by convolving the input data with an interpolation kernel. The distinct appearance of this kernel has to be chosen carefully to avoid modulation effects in the image arising from the convolution. The complete process of regridding a non-Cartesian sampled k-space can be described in the following way.
Let $S(k_r, k_\theta)$ be the polar sampled k-space data

$$S(k_r, k_s) = \left(\frac{\pi}{n_s}\right) \Delta k_s \Delta k_r \sum_{p=0}^{2n_s-1} \sum_{q=0}^{n_r/2-1} \left[\delta\left(k_s - p\Delta k_s\right)\ \delta(k_r - q\Delta k_r)\right], \tag{3.18}$$

where n_s is the number of radial spokes and Δk_r denotes the increments between the n_r sample points along every spoke.
Equivalent to the filtering step in FBP, the inhomogeneous sampling density associated with radial sampling has to be compensated for. The most basic form of compensation is the multiplication with a ramp or Ram-Lak function $C(k_r, k_s)$ in the frequency domain:

$$S(k_r, k_s) \cdot C(k_r, k_s) \tag{3.19}$$

where the normalized compensation function $C(k_r, k_\theta)$ is defined as

$$C(k_r, k_s) = \begin{cases} |k_r|/n_s & \text{for } |k_r| \neq 0 \\ 1/2n_s & \text{for } |k_r| = 0. \end{cases} \tag{3.20}$$

Subsequently, the interpolation kernel has to be carefully designed and applied in order to spread out the radial sampling points. Ideally, the real space representation (referred to as apodization) of the k-space interpolation kernel would be a rectangular function, yielding a rectangular FOV in image space:

$$\text{rect}(\frac{x}{FOV})\text{rect}(\frac{y}{FOV}). \tag{3.21}$$

Equivalent to ideal RF-pulses the $\mathcal{FT}$ of a rectangle is given by the sinc function. However, since the sinc-function is of unlimited extent, in real applications it has to be truncated. The confinement of the sinc-function's bandwidth results in loss of FOV and thus aliasing. Consequently, an alternative compact kernel, approximating the sinc function has to be used. Based on the results of Jackson et al. [133] the close to optimal interpolation kernel is given by the Kaiser-Bessel function ($KB(k_x, k_y)$). Figure 3.7 presents the schematic convolution of one single radial sampling point (red circles) with the interpolation kernel

$$[S(k_r, k_s) \cdot C(k_r, k_s)] * KB(k_x, k_y) \tag{3.22}$$

resulting in a distribution over several Cartesian sampling points (yellow crosses).
The third step towards reconstruction is the actual sampling onto the Cartesian grid using a comb sampling function

$$\text{III}(k_x, k_y) = \sum_i \delta(k_x - k_{x_i}, k_y - k_{y_i}). \tag{3.23}$$

When designing the Cartesian grid, hence the comb function's $k_{x,i}$ and $k_{y,i}$, the sampling density of the grid plays an essential role. As aforementioned, instead of using the ideal *sinc*-function as interpolation kernel, a Kaiser-Bessel function is employed. While this reduces the problem of aliasing, the non ideal apodization of the $KB(k_x, k_y)$-function still causes minor folding artifacts of adjacent replicas. The solution to this problem is oversampling. Using typically twice the original matrix size, hence half the sampling distance ($\Delta k/2$), the FOV of the image doubles and replicas are shifted away from the actual reconstruction. Subsequently, the image simply has to be cropped to the original size.

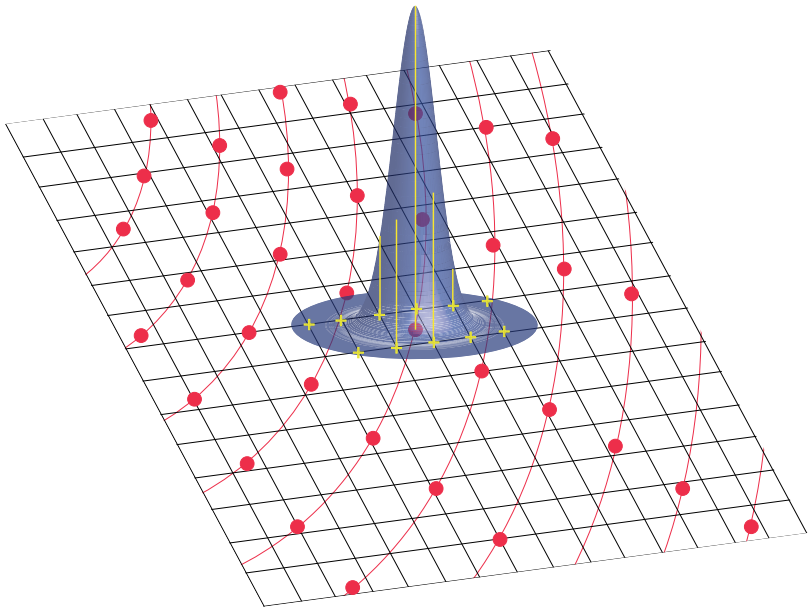

Figure 3.7: Kaiser-Bessel interpolation kernel used to 'smear' out the original radial k-space points (red dots) over several Cartesian k-space positions (yellow crosses).

As a final step, the basic 2D inverse Fourier transform is applied to reconstruct the image. The complete reconstruction from radial k-space data can consequently be summarized as:

$$\mathcal{FT}^{-1}[S(k_r, k_s) \cdot C(k_r, k_s) * KB(k_x, k_y) \cdot \mathrm{III}(k_x, k_y)] \tag{3.24}$$

Evidently, if $S(t, \theta)$ denotes projections generated via CT, $S(k_r, k_\theta)$ in Equ. 3.24 has to be substituted by $S(k_r, k_\theta) = \mathcal{FT}_1 S(t, \theta)$ where $\mathcal{FT}_1$ is the 1D Fourier transform.
The regridding method implemented for reconstruction in the following bases on the NUFFT algorithm introduced by Fessler et al. [35].

3.1.6 Point spread function

The *point spread function* (PSF) or respectively impulse response function of an imaging system characterizes how a point source is processed over the course of image acquisition and reconstruction [125, 126, 134]. The PSF can be computed as the $\mathcal{FT}$ of the systems sampling function (cf. Equ. 3.18):

$$\mathrm{PSF}(r, \theta) = \left(\frac{\pi \Delta k_r^2}{N_s}\right) \sum_{m=0}^{2N_s-1} \sum_{n=0}^{N_r/2-1} \left[n \ \exp\left(-2\pi i n \Delta k_r r \ \cos\left(\theta - \frac{m\pi}{N_s}\right)\right)\right] \tag{3.25}$$

Figure 3.8 demonstrates how the resulting image can be modelled from the original object and the PSF. If the point spread function of the imaging system is known, the result of the acquisition can be calculated via convolution of the object and the PSF. In the presented example the image depicts a blurry representation of the original object on account of the

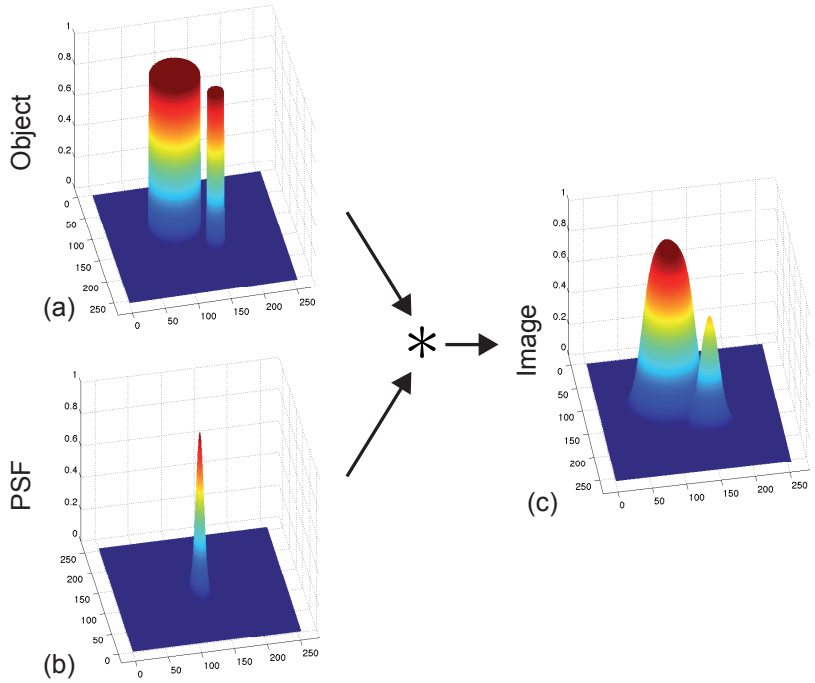

Figure 3.8: The convolution of the original object (a) with the point spread function (PSF) (b) of the imaging system results in a representation resembling the outcome of a actual measurement (c).

PSF being Gaussian shaped with a not negligible width. The width of the PSF is at the same time a measure for the spatial resolution of the imaging system.
The point spread function describes the impulse response of the imaging systems, hence how a single point object is processed by the imaging and reconstruction. If, for simplicity, relaxation and other effects are neglected, the PSF can be generated from the polar trajectory through k-space. Setting all sampling points to one and the rest of k-space to zero, the reconstruction yields the systems point spread function (see Fig. 3.9).

3.1.7 Advantages and disadvantages of radial sampling

The considerations regarding the Nyquist limit for radial sampling in Subsection 3.1.3 demonstrated that the number of samples necessary to fully sample a radial k-space is a factor of 1.57 higher when compared to Cartesian sampling. At first glance this is of course a disadvantage due to an increase in measurement time. However, because of the distinct nature of the radial sampling distribution this drawback can be diminished. As discussed in Subsection 3.1.3, at a fixed base resolution the sampling density satisfying Equ. 3.12 solely depends upon the number of acquired spokes or, respectively, the azimuthal distance of sampling locations. Consequently, if the number of spokes was set equal to the number of lines in the respective Cartesian setting, the outermost gaps between sampling points Δk_s^{max} undercut the Nyquist limit. However, since the sampling density in radial

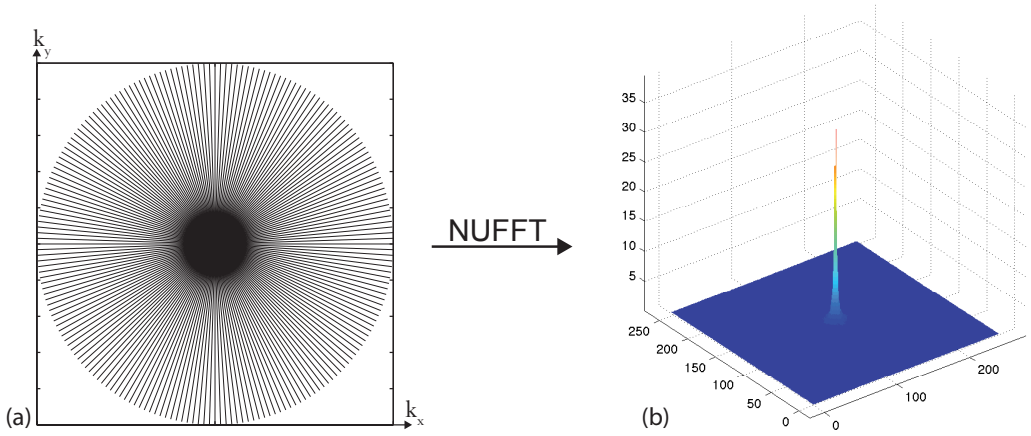

Figure 3.9: (a) k-values in a fully sampled radial k-space. (b) 2D point spread function of the k-space in (a) computed via NUFFT transformation.

acquisition is non-uniformly distributed over high and low frequencies, the impact of undersampling vastly differs. In a majority of the cases, objects measured in tomography, as all natural images are to a large degree piecewise smooth, that is, consisting of areas with constant intensity. Now, since minor undersampling in radial imaging merely affects high frequencies, there is no impact on low-frequency components, such as contrast properties. Consequently, even if a number of samples equal to the Cartesian case is used, the impact on the image, hence its diagnostic value is negligible.
Another consequence which can be drawn from the characteristics of radial spokes is the fact that every single line in k-space carries both high and low frequencies. This attribute can be of great importance in dynamic applications such as real-time MRI, where the measurement is confronted with moving objects and contrast variations. If those dynamic changes appear in Cartesian sampling while high frequencies are acquired the effect will be only minor. However, if motion occurs during the acquisition of contrast carrying low frequency lines, the impact on the reconstruction is drastic. While, spatial variations during radial acquisition have an impact on the image in any case, the overall effect is minor when compared to Cartesian sampling. Since every acquired spoke crosses the center of k-space, even if one or more spokes are corrupted, the subsequent spokes, which carry an equal amount of low-frequency information can compensate for those impairments.
The most prominent argument for radial k-space sampling in MRI is its motion robustness. Regardless of the exact nature (periodic, punctual, constant), motion in between two different phase encoding steps (view-to-view) translates into phase modulation in the Fourier domain. This results in phase errors which are translated into so-called *ghosting artifacts* - replicas of the moving parts, distributed over the whole image in the direction perpendicular to the read-out direction. Movement in between excitation and echo collection (within-view) on the other hand causes deviations in frequency direction, which manifest as noise like artifacts distributed uniformly over the image, posing less perceptual loss in image quality and diagnostic value. Since said phase encoding steps, which are necessary in Cartesian sampling are not part of radial sampling, these effects are completely prevented

when using a polar geometry, merely leaving minor frequency motion artifacts.
The fact that radial sampling solely comprises frequency encoding accounts for additional advantages. In Cartesian sampling a finite amount of time is used for the phase encoding step after each RF-pulse. Since this time is saved in radial sampling, sequences with shorter echo times can be acquired opening the possibility to image tissue with very short T_2. Furthermore, oversampling of k-space data, hence the extension of the FOV in order to avoid aliasing which is only applicable in frequency direction can be applied in all directions when using polar sampling. Additionally, the possibility to perform oversampled acquisitions without the issue of measurement time compensates for the necessity to acquire 1.57-times the number of k-values when compared to Cartesian sampling.
In conclusion, radial sampling might not be preferable to Cartesian sampling in general, however in a huge number of applications the introduced properties of radial sampling can either improve image quality, accelerate the acquisition or yield additional information. The latter is of special interest for the further argumentation of this work. The described variable density of polar k-space and the flexibility in designing the trajectory as introduced in Subsection 3.1.4 pose the chance of generating a great bandwidth of information from one single measurement. How this additional information can be employed to improve imaging will be explained in the following chapters.

3.1.8 Summary

After generalizing the sampling strategy of CT and radial MRI using the Fourier slice theorem, this chapter introduced major concepts of polar data acquisition. The sequence pattern used for radial sampling in MRI can be deduced fairly simple from the pre-existing Cartesian sequences by adapting the applied encoding gradients according to $G_x = G_0 \cos\theta$ and $G_y = G_0 \sin\theta$. One of the advantages of radial sampling is certainly the flexibility in the particular sampling strategy, resulting in variations such as the *interleaved*, *golden angle* or *bit-reverse* acquisition schemes. Since polar sample points are not homogeneously distributed over k-space, the Nyquist condition in radial acquisitions is given by a relation between the number of samples per spoke n_r and the total number of acquired spokes n_s ($n_s \geq \frac{\pi}{2} n_r$). If this condition is satisfied a conventional technique can be used to generate an image. Similar to CT reconstruction the filtered back projection is one approach to reconstruct the image. However, the complex valued nature of MR data led to the development of an alternative technique called *regridding*, in which the polar data is interpolated onto a Cartesian grid and reconstructed vie Fourier transformation.
Radial sampling offers several advantages over a Cartesian strategy, including a lower sensitivity to motion and the possibility to perform oversampling in all direction without severely prolonging the measurement. Additionally, the inhomogeneous nature of polar sampling points with a higher density in the k-space center leads to a completely different aliasing behaviour if the Nyquist limit is violated. Since the k-space center sampling density is much higher than the density at higher k-values, even if undersampling is performed the basic low-frequency contrast information is preserved in the image.

3.2 Iterative reconstruction from incomplete radial data

In previous sections the importance of satisfying the Nyquist limit in any k-space sampling case was addressed extensively. In order to be able to reconstruct an image without aliasing artifacts using a conventional reconstruction method, a certain number of samples have to be acquired. While this is the theoretically necessary case, in reality this prerequisite cannot be satisfied. In many real measurement settings, factors such as dose limitations in CT, the urge to temporally resolve physiological processes in real-time MRI or to acquire ultra-high resolution MRI are a demanding task for imaging modalities. Equivalent to dose limitations in CT in MRI the Specific Absorption Rate (SAR) [135] is often a restricting factor. Also, the hardware itself is bound to certain technical limits. Consequently, in these cases there is no alternative but to reduce the amount of data sampled in the measurement. The next chapter will focus on the effect of undercutting the Nyquist limit and introduce a novel reconstruction tool to circumvent conventional drawbacks associated with incomplete data. Subsection 3.2.1 will demonstrate the impact of undersampling in case of different sampling strategies and constitute the necessity of a different reconstruction approach formulated in Subsection 3.2.2. Subsequently, the concept of regularization is introduced on the basis of three prior knowledge terms (cf. Subsection 3.2.3). Here the focus lies on the novel concept of employing the image histogram entropy as universal measure of artifacts (see Subsection 3.2.3). Finally this chapter will explain the distinct implementation of an iterative reconstruction algorithm (cf. Subsection 3.2.4) including the computation of a histogram gradient (Subsection 3.2.4) and introduce a quantitative measure of image quality (Subsection 3.2.5) used to asses the performance of the novel reconstruction.

3.2.1 Impact of incomplete sampling

From the considerations regarding the Nyquist limit for different sampling trajectories it is clear that the consequences of undersampling can be of very different nature. The simplest case of aliasing can be observed for Cartesian sampling by increasing Δk while $|k_{max}|$ is fixed (Fig. 3.10(a)). That is, skipped sampling points are set to zero and the conventional FT is applied for reconstruction. Since the sampling density is not sufficient, the FOV does not cover the whole object. Hence, replicas of the object get folded back into the FOV overlapping with the original image. Figure 3.10(b) depicts folding artifacts if a reduction factor of $R = 2$ is used, where the FOV is half the original.
Recent developments in imaging and reconstruction led to the employment of variations in the Cartesian sampling scheme [38]. Figures 3.10(c/e) demonstrate two alternative trajectories through k-space. While the sampling points still lie on a Cartesian grid the coordinates are chosen pseudo-randomly from the set of possible k-values ($-k_{max} : \Delta\tilde{k} : k_{max}$ where $\Delta\tilde{k}$ is chosen randomly). As evident from Figs. 3.10(d/f) this procedure changes the appearance of aliasing in the image to a great degree. While equidistant undersampling results in folding of replicas of comparable intensity as the original at distinct positions, the randomness of k-space points in the latter cases causes the aliasing to distribute over the whole image. This results in artifacts which appear rather noise-like. This undersampling strategy and its aliasing artifacts are referred to as incoherent and are one of the foundations of novel

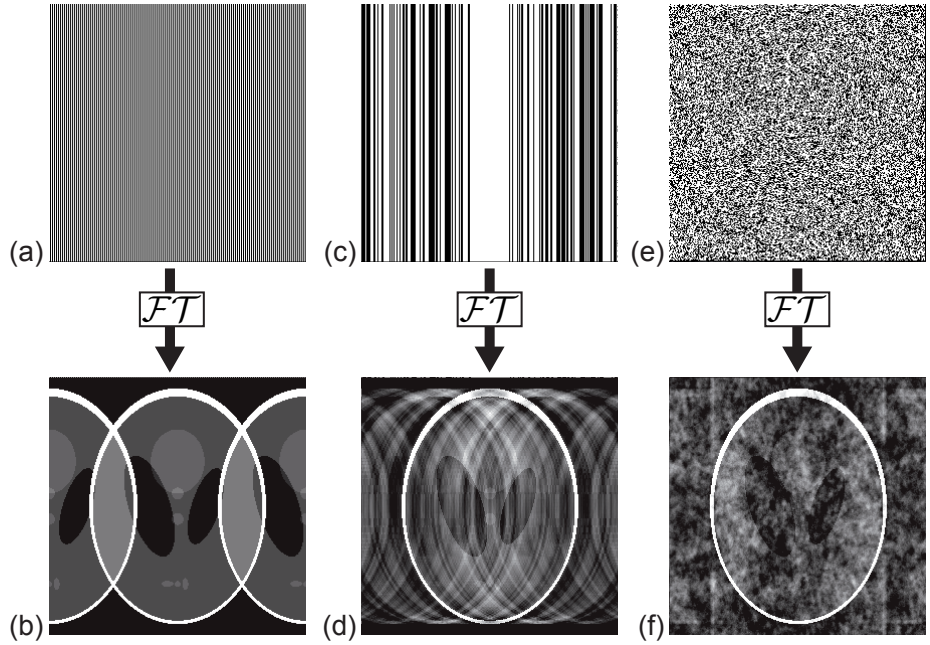

Figure 3.10: The effect of undersampling in Cartesian sampling. (a) Data reduction by skipping every second line results in folding artifacts after $\mathcal{FT}$ (b), due to the increase in Δk. (c) If the order of skipped lines is randomized in one direction (phase) the nature of artifacts (d) changes. (e) Randomizing the sampling in both directions causes the artifacts to appear almost noise like in the reconstruction (f).

reconstruction techniques such as *compressed sensing*. While there is no possibility to distinguish between original object and aliasing in the equidistant undersampling case (cf. Fig. 3.10(b)), incoherent aliasing offers the possibility to recover the actual image by separating signal from noise-like artifacts.

The impact of radial undersampling is exemplarily demonstrated on a simple regridding reconstruction of the Shepp-Logan phantom in Fig. 3.11. The radial acquisition was simulated with a base resolution of $n_r = 256$ pixels and a decreasing number of spokes from $n_s = 402$ to $n_s = 26$, where the first corresponds to full or Nyquist sampling according to Equ. 3.12 and the latter to a reduction factor of $R = 16$. Evidently, aliasing in case of radial sampling inherently manifests as incoherent undersampling artifacts. While comprehensive theoretical description of all visible effects is provided by references [134, 136], the key observations shall be discussed briefly.

Since the reconstruction of the image can be computed by convolving every single pixel with the PSF (see Subsection 3.1.6), the impact of undersampling is best observable in Fig. 3.11 on the PSF itself. The fully sampled measurement in the first column depicts no undersampling artifacts in the reconstruction. The corresponding PSF presents a narrow peak in the center accompanied by minor oscillations. Although the number of spokes in the presented case was set according to Equ. 3.12, the PSF in Fig. 3.11 show minor oscillations.

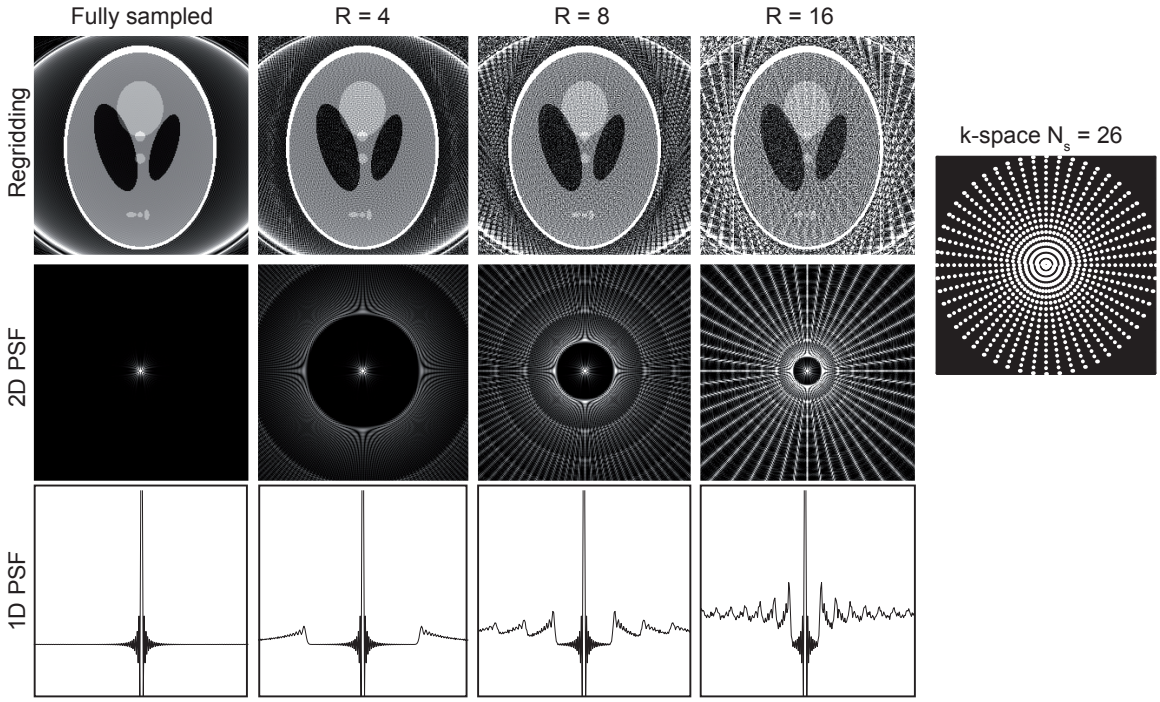

Figure 3.11: Impact of radial undersampling on the the reconstruction and the point spread function of the system. The first row depicts the reconstruction of a Shepp-Logan phantom sampled with a decreasing number of spokes, from fully sampled to a reduction factor of 16, hence only 26 spokes. Row two and three demonstrate the influence on the PSF, when the number of spokes is limited. The radius of the artifacts free circle decreases, while the number and amplitude of the oscillating streaks increases.

These can be ascribed to the finite FOV, respectively the truncated k-space and are termed truncation artifacts. As previously mentioned, the fact that the FOV is finite, hence the k-space is sampled over a limited extent can be understood if the used Cartesian sampling comb (Equ. 3.23, 3.24) is cut of at a certain value:

$$\text{III}(k_x/\Delta k_r) \cdot \Pi(k_x/(2M\Delta k_r)) \tag{3.26}$$

whose $\mathcal{FT}$ is

$$\text{III}(x\Delta k_r) * \text{sinc}(Mx\Delta k_r). \tag{3.27}$$

The rectangular function Π limits the comb function, however introduces sinc-like oscillations in the reconstruction.
With an increasing reduction factor additional sever streaking artifacts, starting from a certain circular distance are observable. The diameter of the streaking-free disc around the center peak is inversely proportional to the number of acquired spokes. It marks the maximum FOV which can be imaged with the number of acquired spokes, without considerable aliasing artifacts in the reconstruction. Vice versa, via $\Delta k = 1/FOV$, the radius of the disc

also yields the maximal base resolution, which together with the number of spokes satisfies the Nyquist limit.
From this example it is clear that a simple regridding reconstruction is insufficient when aiming for the full resolution, even at relatively small reduction factors. The information lost in large azimuthal gaps between sampled spokes prevents the reconstruction of the original object. Consequently, in order to recover a reconstruction result close to the fully sampled one, it is necessary to employ more sophisticated reconstruction approaches. These have to take the special nature of incoherent undersampling artifacts into account in order to be able to differentiate between true signal and artifacts. In which way and to which degree of undersampling the original object can be recovered will be introduced in detail in the next sections.

3.2.2 Inverse problem

To find a different approach for the undersampled reconstruction problem it is beneficial to formulate the measurement and reconstruction operation in a linear algebraic nomenclature. Let $f \in \mathbb{C}^N$ be a complex-valued, continuous, N-dimensional function representing the image subject to sampling. While measuring f directly is not possible, one can sample the image by applying the following forward operation:

$$y = \Phi f \qquad \begin{array}{l} y \in \mathbb{C}^M \\ \Phi \quad M \times N \quad \text{matrix.} \end{array} \tag{3.28}$$

Here y denotes the result of discretely sampling f using the $M \times N$ system matrix Φ. Measured data from all spokes are stacked in an M-dimensional complex vector. In MRI, for instance, Φ is a matrix of Fourier coefficients. More generally however, the system matrix comprises the linear combination of different operations, which becomes obvious when formulating the *inverse problem*, hence the reconstruction:

$$f' = \Phi' y. \tag{3.29}$$

Here Φ' denotes the adjoint matrix to Φ, comprising all steps necessary to translate the measurement vector y back onto f', a discrete estimate of the object. Within a conventional measurement one would choose $M = N$, which makes the reconstruction a well determined or in case $M > N$ even an over-determined system of linear equations, solvable with basic linear algebra, for instance by simple inverting Φ.
In the undersampled case, corresponding to $M < N$ however, the system of linear equations is under-determined or ill-posed (cf. Fig. 3.12). That is, the *correct* solution exists in a sub-space of dimension $(N - M)$. If the signal f is for instance of dimension $N = 3$ and one would perform 2 measurements, the solution f' lies anywhere in a line sub-space. Consequently, the task is to find the *true* solution from the infinite set of possible solutions in the $(N - M)$-dimensional space. Since this problem is ill-pose, very large and often corrupted by Gaussian noise, direct inversion is impractical. In this cases a reconstruction by iteratively estimating the image vector f' are the far better choice. Estimating the image in this context means to find the solution among all possible, that resembles the fully sampled

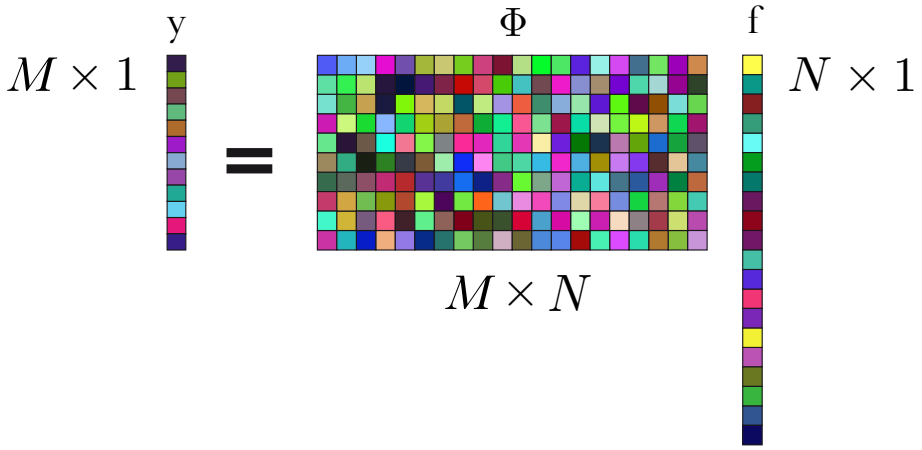

Figure 3.12: If the object function f of dimension N is sampled via matrix Φ of size $M \times N$ ($M < N$), solving the reconstruction problem for y yields an ill-posed system of linear equations.

one as closely as possible.
In reality, however, it is not possible to actually calculate the whole subset of solutions and subsequently choose the one best fitting the expectation. In fact it is more practical to reconstruct a *first guess* image f', for instance by regridding the undersampled data and alter that initial image in order to approximate the desired solution in an optimization process. Of course, one has to ensure that the resulting image still approximates the originally measured data as closely as possible. This *data fidelity* is realized by introducing the following term:

$$||\Phi f' - y||_2. \tag{3.30}$$

Here $||\ ||_2$ denotes the l_2 or Euclidean norm, quantifying the similarity of both vectors. While solving the optimization task of Equ. 3.30 results in an image closely resembling the measured data, it might still not be free of artifacts. In order to find the image with the least artifacts one has to employ more information in the iterative reconstruction. More precisely, if any attribute of an artifact-free image is known to be universally true it can be embedded in the iterative minimization. Let $R(f)$ be a certain feature of the target image, which is known to be minimal in the absence of artifacts. Then the task is to both maximizing data fidelity and choosing the image with minimal $R(f)$:

$$\begin{aligned} &\text{minimize} && R(f) \\ &\text{subject to} && ||\Phi f' - y||_2 = 0. \end{aligned} \tag{3.31}$$

Optimization problems of the form of Equ. 3.31 are commonly solved as a so called regularized or constrained optimization and can be rewritten in one single expression. The so called cost or object function

$$C(f') = ||\Phi f' - y||_2 + \sum_i \lambda_i \mathbf{R}_i(f), \tag{3.32}$$

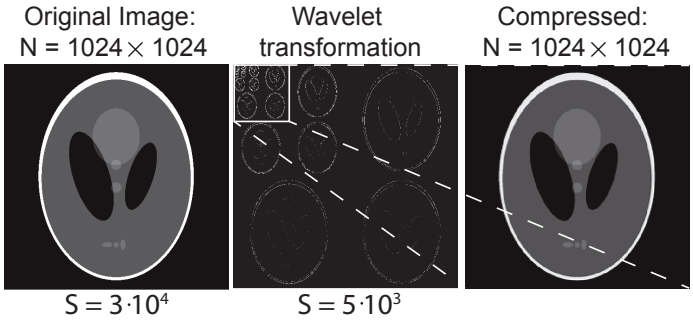

Figure 3.13: Wavelet analysis and compressed synthesis. The number of non-zero entries S, hence the number of pixels actually containing information decreases by a factor of 6 in the Wavelet domain. Merely 6.9% of the coefficients, result in an image hardly distinguishable from the original.

comprises both the data fidelity and the regularization term or a multitude of regularization terms. The regularization parameter λ gives a weighting, how strongly the minimization should incorporate the constraint. If $\lambda = 0$ the result solely resembles the measured data, if $\lambda = 1$ minimizing $R(f)$ is equally weighted as minimizing the data fidelity term.

3.2.3 Prior knowledge and artifact identification

In order to reconstruct an image without artifacts it is crucial to identify features of the image present in an artifact-free reconstruction or vice versa find a measure to separate artifacts from real image information. Once these features are determined, a regularization function R can be defined, which further restricts the search for the *true* image. Here the challenge lies in the demand of universality. The image attribute assumed to be *prior knowledge* has to be applicable to any measured object. The following chapter will introduce measures of artifacts and *a priori* known image features which can be employed as regularizer.

Sparsity

A sparse signal or object is populated primarily with zero entries and is by nature easily compressible. In tomography in rare cases, such as angiography, the image itself is sparse to begin with. Consequently, in the confined field of angiography sparsity can serve as general prior knowledge of the image. In general however, one has to find a representation in a certain well-chosen basis Ψ, which introduces sparsity to the data. This concept is well-known from image compression algorithms such as JPEG2000 [137]. The original image is decomposed in a well chosen basis, populating only few coefficients. Subsequently, coefficients with an energy below a certain threshold are cut off, resulting in a reduced amount of stored data. How effective an image can be compressed is strongly dependent on the basis functions Ψ.

A signal or vector f is called S-sparse in the basis $\Psi = \psi_1, \psi_2, \cdots, \psi_n$, if after decomposition

$$f = \sum_{i=1}^{n} x_i \psi_i \tag{3.33}$$

the sparse synthesis holds

$$f_S \approx f \quad \text{with} \quad f_S := \Psi x_S \qquad \#x_S = S \ll n. \tag{3.34}$$

Here f_S denotes the synthesis of the signal only using a subset x_s of cardinality S out of the original n coefficients x_i. In words, if the initial signal can be very closely approximated by only using a subset of coefficients ψ_i, it is referred to as S-sparse in the basis Ψ.
For natural images the most recent developments in compression demonstrated that the Wavelet transform (WT) [138, 139] is a very efficient sparsifying operation. Wavelets are a family of time-frequency base functions used to decompose the underlying signal. When compared to Fourier decomposition, the Wavelet transformation mainly benefits from its temporal resolution. The Wavelet transformation offers the possibility to capture both frequency and location in time. Hence, it adaptively samples the initial signal. While the family of Wavelets comprises numerous functions, the commonly and successfully used base are the Daubechies wavelets. Figure 3.13 depicts the Wavelet transformation of the Shepp-Logan phantom, occupied mainly with zeros. After discarding roughly 94% of the weakly populated Wavelet coefficients the reconstruction is almost not distinguishable from the original image. This simple example shows how effective the WT can sparsify natural images.
Another very effective sparsifying transformation, which has previously been adapted for noise cancellation [140] and image reconstruction [44] is the finite difference transformation, computed as the discrete gradient

$$\nabla f(m,n) = \sqrt{(D_x f)^2 + (D_y f)^2}, \tag{3.35}$$

where $D_x f = f(m+1,n) - f(m,n)$ and $D_y = f(m,n+1) - f(m,n)$ denote the discrete derivatives in x and y direction, respectively. Assuming again that natural images, hence tomographic reconstructions comprise mainly areas of constant, or marginally varying intensity, this transformation results in an image representation, where merely steps in the intensity have non-zero coefficients (see Fig. 3.14). Evidently, the Shepp-Logan phantom is an object perfectly fitting the prerequisite of piecewise smoothness. While real objects might not satisfy this requirement as perfectly, finite difference nevertheless serves as an effective sparsifying transformation.
Applying both transformations separately leads to an efficient sparsification of tomographic images, emphasising different image features, such as small details and edges.
Figure 3.15 demonstrates the sensitivity of finite difference and Wavelet sparsity to incomplete sampling of increasing severity. As the number of spokes decreases, hence the reduction factor used increases, artifacts appear in the image. These artifacts yield non-zero values at coefficients not populated with information in the fully sampled case. Employing sparsity

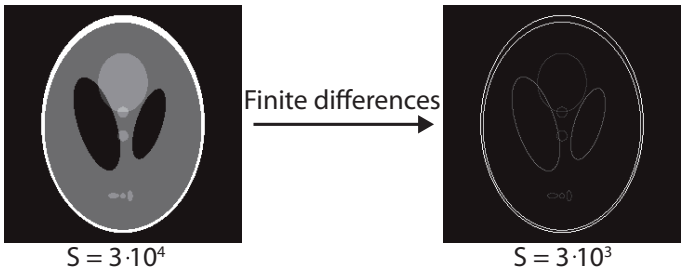

Figure 3.14: The Finite Difference transformation is almost perfectly tailored to sparsify images such as the Shepp-Logan phantom, hence images comprising only areas of piece-wise constant intensity. The number of non-zero entries S decreases by a factor of 10 when the Finite Difference transformation is applied.

in the iterative reconstruction means to transform the search for a solution into one of the introduced sparsity domains. That is, by applying a spasifying transformation prior to the iterations, the search task redefines to minimizing sparsity in the corresponding domain. After the solution of minimal sparsity is found, it is back-transformed into the image domain. As introduced, this secondary condition is implemented as a constraint during the iterations. The cost function, including both Wavelet sparsity and finite differences is given by:

$$C(f) = ||\Phi f - y||_2 + \lambda_{WL}\mathbf{R}_{WL}(f) + \lambda_{FD}\mathbf{R}_{FD}(f). \tag{3.36}$$

Here the regularizations $\mathbf{R}_{WL}$ and $\mathbf{R}_{FD}$ enforce the minimization of sparsity in the corresponding domains WL and FD. In order to reduce sparsity however, it is necessary to find a measure for sparsity. Theoretically, sparsity is simply quantified by counting the number of non-zero entries, which is equal to the so called l_0-norm

$$||x||_0 = \#(i|x_i \neq 0). \tag{3.37}$$

However, the minimization of the l_0-norm is a computationally very complex problem and almost impossible to solve, at least in a reasonable time. Donoho [40] was able to prove, that, when dealing with ill-posed systems of linear equations in a huge majority of the cases the solution that minimizes the l_1-norm

$$||x||_1 = \sum_i |x_i| \tag{3.38}$$

is also the sparsest solution. In contrary to the l_0-norm, the l_1-norm is a computationally less complex problem, solvable with standard optimization algorithms. Consequently, employing the l_1-norm as a measure of sparsity the regularizations are given by

$$\mathbf{R}_{WL}(f) = ||WL(f)||_1 \tag{3.39}$$

$$\mathbf{R}_{FD}(f) = ||FD(f)||_1. \tag{3.40}$$

The l_1-norm of FD, R_{TV} is commonly referred to as the *Total Variation* of f and is denoted $\mathbf{R}_{TV}$ in the following.

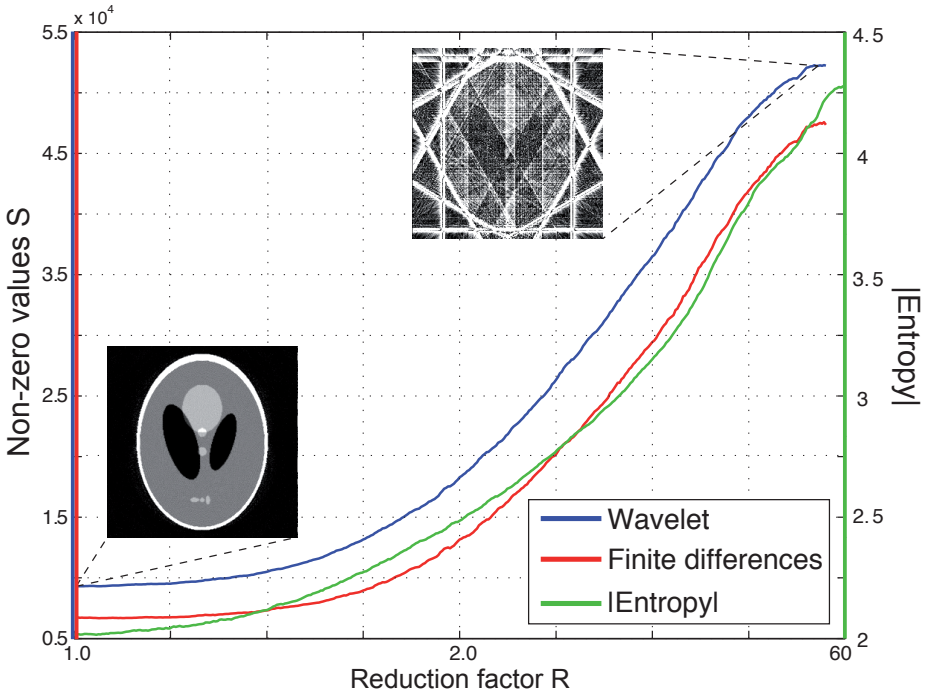

Figure 3.15: With an increasing reduction factor, hence a decreasing sampling density the abundance and severity of streaking artifacts causes the number S of non-zero values to increase in both the finite difference (solid/blue line) and Wavelet domain (dashed/green line). In the same way, with a decreasing amount of acquired data, from fully sampled to a reduction factor of 60, the Shannon entropy of the images increases from a value of approximately 2 to 4.6.

Shannon entropy

In information theory entropy is a measure of the uncertainty in a random variable. In the present context the term *Shannon entropy* denotes the expectation value of the information contained in an image.
The Shannon entropy [68] of an image A with intensities $\{a_1, \ldots, a_n\}$ is defined as

$$E(A) = -\sum_{i=1}^{n} p(a_i) log(p(a_i)) \tag{3.41}$$

where $p(a_i)$ denotes the probability of intensity a_i appearing in image A.
Piecewise smooth objects such as the Shepp-Logan phantom naturally have a very small entropy, since the image merely comprises 4 distinct intensity values. Each intensity species is highly populated, thus has a high probability of appearing when choosing a random pixel. Artifacts of any kind on the other hand introduce additional intensities in image space, hence increase the entropy of the image.
The right hand side scale in Fig. 3.15 demonstrates the impact of undersampling artifacts on the entropy of the Shepp-Logan phantom. The magnitude of the entropy increases from

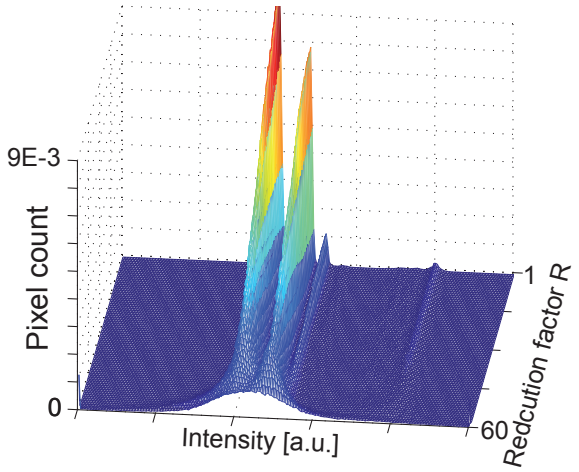

Figure 3.16: Impact of undersampling on the intensity histogram. An increase of the reduction factor, hence decrease in the number of spokes causes peaks in the histogram to spread out and overlap. In case of the peak with the highest intensity (right) even to a degree, where the peak is not visible any more.

a value of $E \approx 0.1$ to $E \approx 2.0$ when the number of spokes in the radial acquisition decreases and the severity of streaking increases.
These considerations demonstrate that, in addition to sparsity, Shannon entropy can serve as a measure of undersampling artifacts and noise. However, the application of entropy itself as a basis for image correction was found to be applicable only in certain cases [141, 142]. The following section will introduce an indirect way to measure the entropy of an image, feasible to embed into the iterative reconstruction as regularization.

Histogram entropy

The intensity histogram as a measure of entropy was successfully employed in the field of image registration [62] and artifact reduction in parallel imaging [69]. The Shannon entropy of an image A with matrix size N^2 can be computed directly from the image intensity histogram $H(A)$ via

$$p(x_i) = \frac{H(x_i)}{N^2}. \tag{3.42}$$

Hence, it is possible to employ the histogram to indirectly measure the entropy itself.
Small values of entropy correspond to a sparse histogram representation, i.e. few, highly populated peaks of narrow bin extent. Since different peaks can be ascribed to different pixel intensity species, in image space histograms of such appearance present as piecewise smooth. Vice versa, if the image is corrupted by noise or artifacts, such as the above mentioned, additional intensities appear in the image, which in turn cause histogram peaks to broaden and an increase in entropy. This potentially even results in the overlap or merging of peaks. Figure 3.16 depicts the impact of undersampling artifacts on the histogram of a Shepp-Logan phantom. While the total pixel count of course is constant, the distribution

over intensity bins changes drastically. The 4 major intensity peaks, visible up to an reduction factor of approximately 2 spread out and overlap to a degree where only one very broad peak is identifiable.
Evidently, the impact of undersampling on the entropy is translated even more drastically to the appearance of the image intensity histogram suggesting to employ the histogram of the image as a measure of artifacts in the image. Consequently, in addition to minimal sparsity one can employ minimal histogram entropy as regularization $\mathbf{R}_H$ in the reconstruction. In which way the proposed regularizations are implemented in the iterative reconstruction will be specified in detail in the next section.

3.2.4 Implementation

In the previous section a cost function was introduced, comprising a data fidelity term and additional constraints, enforcing certain image features, which serve as prior knowledge. The iterative reconstruction aims to minimize the entire cost function in order to find the solution closest resembling the acquired data and matching the prior knowledge terms as exact as possible. Among the numerous optimization algorithms for this case the *conjugate gradient* (CG) [143] approach has shown to generate the best results and is commonly applied in iterative reconstruction methods. Before introducing CG one experimental issue of modern MRI has to be addressed.

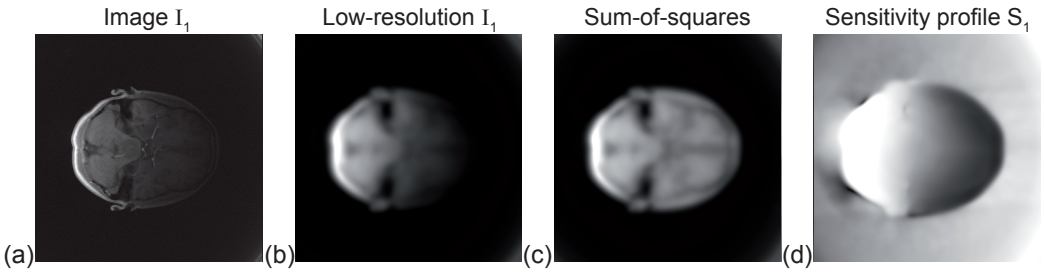

Figure 3.17: Generating a sensitivity map for the reconstruction of multi-coil data. The raw-data from the original single coil image I_1 (a) is used to compute a low-resolution image (b). Additionally the sum-of-squares (SOS) magnitude image from all single coils is calculated. Dividing the low-resolution image by the SOS image yields the coil sensitivity map necessary to weight each single coil image when computing the total image.

Processing of multi-coil data

The previous considerations concerning image reconstruction have disregarded one important experimental issue in MRI. Modern magnetic resonance imaging systems usually employ phased array coils for acquisition. That is, the specific array implemented for detecting the generated signal comprise a combination of single coil elements $c = 1 \dots N_c$, each acquiring a single image I_c (see Fig. 3.17) with an individual intensity and phase profile. While

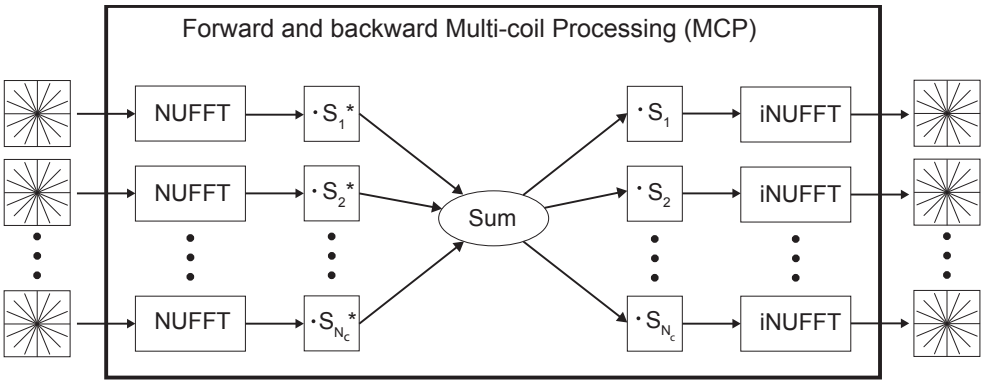

Figure 3.18: Reconstruction of multi-coil data: The single coil raw data is regridded via NUFFT, multiplied with the complex conjugate of the computed sensitivity maps and summed, resulting in the total image. Inverse transformation: The total image is multiplied by the sensitivity profiles and gridded onto a polar grid, resulting in multiple radial k-space trajectories.

this issue is usually resolved by calculating the magnitude image, hence the sum of squares (SOS) over all images, this approach is not possible for the iterative reconstruction. Since the SOS procedure is not reversible a back-transformation during iterations is impossible. Consequently, the complex valued nature of the image has to be maintained.
The common approach in order to combine images from multiple coils is to estimate the individual *sensitivity profile* S_c of each coil in order to take intensity and phase variations into account in the single reconstructions. While the determination of said profiles usually requires an additional acquisition, a different rudimentary approach suggests itself.
As briefly mentioned in Subsection 3.2.1 even if a radially sampled k-space is undersampled the reconstruction can be artifact-free if the k-space is constricted to the fully sampled circle around the center. This results in an image of decreased resolution (see Fig. 3.17(b)). In some cases reducing the resolution to a degree where only the basic low frequency intensity information is left, is even sufficient as sensitivity profile. However, in order to avoid any structural information in the sensitivity images it is advisable to employ the SOS reconstruction of the low-resolution representation (Fig. 3.17(c)) to further reduce structural information in the images. Since the SOS magnitude reconstruction does not show any intensity variations from the single coils, dividing the individual low-resolution coil images by the SOS eliminates residual structural information. The outcome (Fig. 3.17(d)) is a sufficient estimation of the actual sensitivity profiles of each coil without the necessity of an additional scan.
Once the sensitivities S_c are calculated the intensity and phase gradients in the single coil reconstructions are canceled out by multiplying with the complex conjugate S_c^*. Subsequently, the summation of all c single coil images produces the desired complex valued image. The inverse direction is realized in a similar manner. Starting from the complexed valued total image, single coil images I_c can be calculated by multiplication with the according sensitivity profile S_c. Figure 3.18 summarizes the conventional reconstruction of

data acquired with phased array coils.

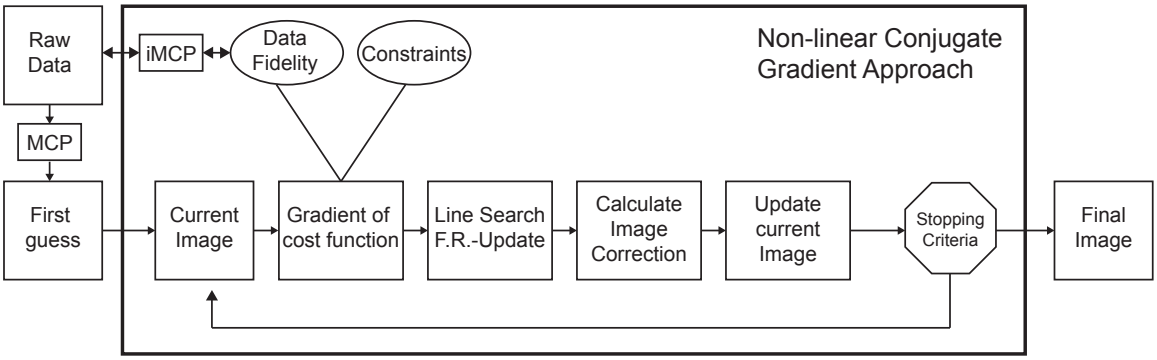

Figure 3.19: Non-linear conjugate gradient flow chart. Starting from the multi-coil raw-data forward multi-coil processing (MCP) is applied to reconstruct a first guess image, which serves as initial current image in the iteration steps. Subsequently the search direction is calculated via the gradient of the cost function, comprising general data fidelity, hence the difference between the original raw data and the back-transformed current image and possible constraints. During the line search the algorithm aims to detect the minimum of the cost function along the calculated direction with a certain step size. The step size is updated in order to refine the search via the Fletcher-Reeves method. Once the gradient is calculated the correction can be computed, whose image representation is applied to the image. If the stopping criteria is met (usually a minimal mean squared error) the iteration stop. In any other case the improved image becomes the current image and so forth.

Non-linear conjugate gradient

The implemented non-linear conjugate gradient (CG) algorithm is largely based on the implementation previously proposed by Lustig [38]. While reference [38] provides a detailed insight in the single steps of the algorithm, here an overview according to the flow chart in Fig. 3.19 of the CG method shall suffice.
Staring from the acquired radial raw data a multi-coil processed and regridded first guess image is reconstructed, which serves as current image estimate during the iterations. In order to find the minimal cost function, the algorithm calculates the direction of steepest descent as the gradient of the cost function. This gradient comprises the derivative of the data fidelity (difference to raw data) and the regularization terms. Subsequently, a line search in the gradient direction is performed using the Fletcher-Reeves update [143] to find the minimum in the corresponding direction. That is, the cost function is calculated in certain steps forth and back the search direction, while the step size is adapted according to the chosen update method. The calculated gradient is then translated into an image space matrix and applied to the current image. This procedure is repeated until the residual error satisfies a prior chosen limit or the maximum number of iterations is reached.
In case of data fidelity and Total Variation the gradient of the cost function is calculated

straightforward by differentiation:

$$\nabla C(f) = 2\Phi^*(\Phi f - y) + \sum_i \lambda_i \nabla ||\mathbf{R}_i||_1. \tag{3.43}$$

The calculation of both the l_1 and the histogram constraint requires additional consideration. As described in reference [38] the l_1-norm is not a smooth function, hence its derivative is not well defined. This is counteracted by introducing a smoothing parameter μ prior to the gradient computation, employing the relation $|x| \approx \sqrt{x^* x + \mu}$. In case of the histogram entropy constraint the calculation of the gradient is solved in a different manner which is explained in detailed in the following section.

Histogram gradient

As aforementioned, entropy itself might not serve the purpose of a feasible regularization. However, the intensity histogram of an image yields an applicable measure for undersampling artifacts and a basis for there suppression. For the intended purpose of reducing the histogram entropy of an image the following approach was developed.
Supposed X is the desired artifact-free target image, which is corrupted by undersampling artifacts dX. And let $h(X + dX)$ be the corrupted high entropy histogram of the impaired initial image. Given, it is possible to generate a low entropy reference histogram $h(Y)$, satisfying $h(Y) \approx h(X)$ (note, the source images Y and X do not necessarily have to be of the same appearance), the hypothesis is that artifacts dX can be compensated for by adapting $h(X + dX)$ to match the reference $h(Y)$. That is, the calculated correction reversing the effect of undersampling on the histogram can be projected into image space, yielding a matrix, suppressing the underlying aliasing artifacts.
Hence the histogram constraint is given by:

$$\mathbf{R}_H = \lambda_H ||H_{tar} - H_{ref}||_2, \tag{3.44}$$

where H_{tar} denotes the corrupted histogram of the current image during iterations and H_{ref} is the pre-calculated low entropy reference histogram. In order to illustrate the basic principle of the proposed idea, the histogram of the fully sampled reconstruction will serve as low-entropy reference.
As introduced in the previous section the non-linear conjugate gradient method serves as basis for the optimization. While the gradient for iterative backtracking line-search in case of the data fidelity term is calculated straightforward by calculating $G_{DF} = -\nabla(||\Phi(x) - y||^2)$, the descent direction G_H of the histogram regularization is computed using:

$$G_H = \mathcal{P}\left(\sum_i \frac{d}{dx_i} H \middle| \frac{\pi}{4}\right). \tag{3.45}$$

Here H denotes the 2D joint histogram generated from the target and reference image, comprising information from both 1D histograms. $\mathcal{P}$ is the intermediate projection of the derivative of H. An orthogonal projections $\mathcal{P}(H, 0)$ or $\mathcal{P}(H, \pi)$ of H result in the respective 1D histograms of the involved images, while a projection at an intermediate angle creates

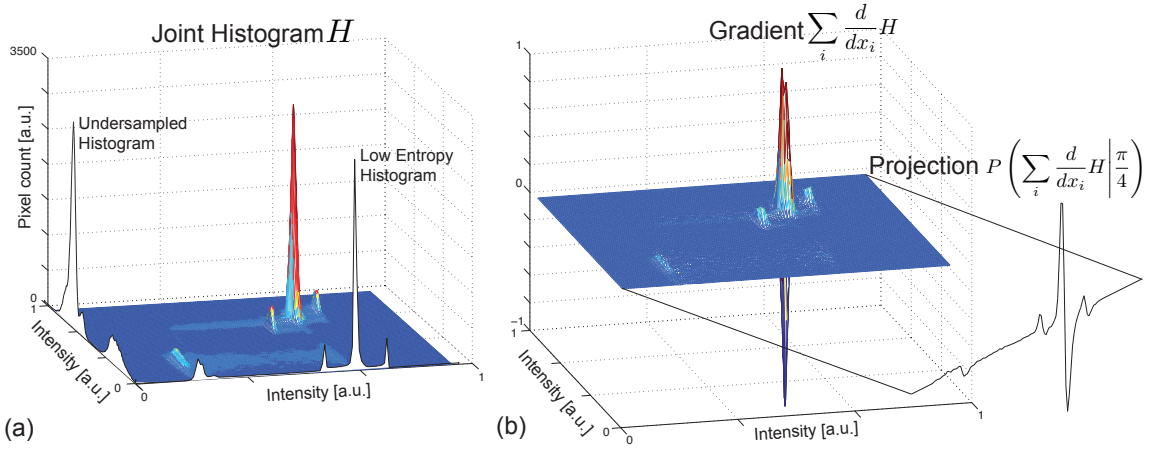

Figure 3.20: (a) Joint histogram computed from the artifact-impaired and the artifact-free reference image. (b) Schematic representation of the calculated gradient in order to find the descent direction for the histogram regularization.

a histogram of mutual information. Figure 3.20 present an example of a joint histogram computed from a a simple object with 4 different intensities. The low-entropy histogram is here generated from the fully sampled reconstruction. In a joint histogram each spatially coincident matching pixel pair in the two images is taken and the signal intensities from the two images are used as indices to place an entry into a two-dimensional array. After performing this operation for all pixel pairs, a 2D histogram is generated (cf. Fig. 3.20(a)). As described in Subsection 3.2.3 undersampling artifacts cause intensity peaks in the histogram to spread out and in many cases an overlap or even merging of previously separated peaks.
In order to find a correction for these changes it is necessary to know both the extent of the peak spreading and the correct peak position. Hence, information from both the corrupted and the reference histogram. The projection $\mathcal{P}$ of the derivative of H at $\frac{\pi}{4}$ generates a measure for the adaptation of $h(A + dA)$ to match the reference histogram $h(B)$ (Fig. 3.20(b)). The gradient G_H is a vector whose components provide the necessary intensity shift for the corresponding intensity value. That is, if the histogram was sampled with the intensity bin array $[I_{min}{:}\Delta I{:}I_{max}]$, $G_H(I)$ contains the shift for image pixels of intensity I. The transformation of $G_H(I)$ into an $(N \times N)$ matrix M with pixel positions $n, m \in 1 \ldots N$ in image space is realized via

$$M = \sum_{I=I_{min}}^{I_{max}} m(x_n, y_m) \cdot G_H(I) \tag{3.46}$$

where $m(x_n, y_m)$ is the normalized matrix with entries only at coordinates according to $X(x_n, y_m) = I$. Thus, the summation in Equ. 3.46 yields a matrix of size N^2 and each pixel contains the respective intensity shift provided by the gradient G_H. In case of complex valued MRI data the gradient matrix is calculated for both the real and imaginary part of

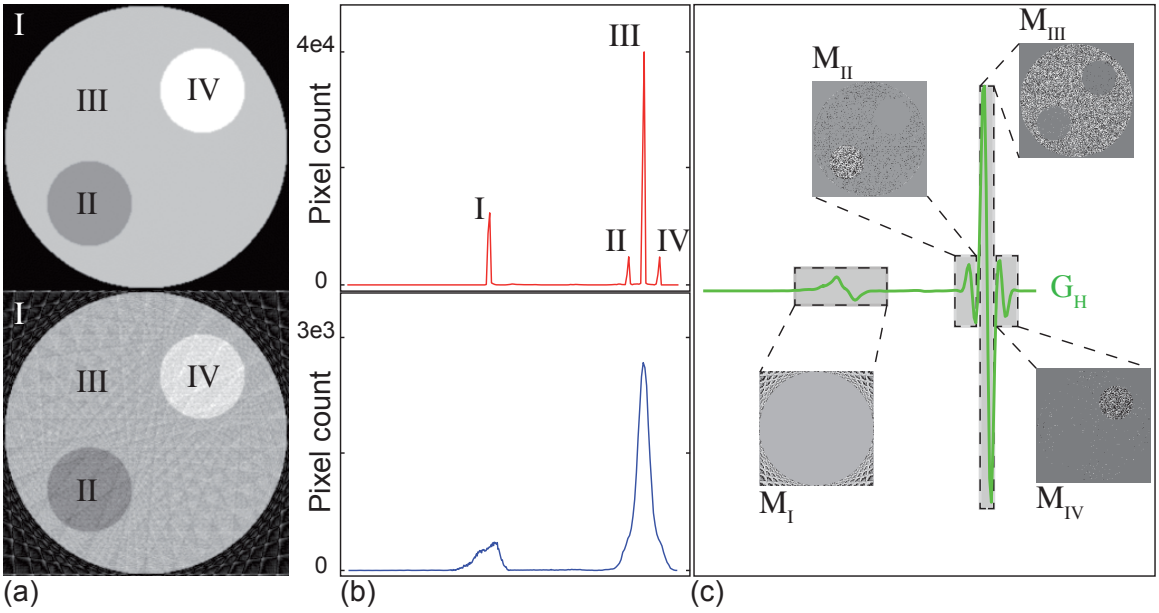

Figure 3.21: Computation of gradient matrix M. (a) Fully sampled (top) and undersampled ($R = 10$) reconstruction (bottom) of a designed numerical phantom. (b) Corresponding histograms. (c) Gradient G_H and single gradient matrices computed for each histogram peak.

the target image, resulting in the total gradient matrix

$$M_t = M_r + i \cdot M_i. \tag{3.47}$$

Figure 3.21 presents the computation of the gradient G_H and the corresponding matrix M_t on a simple undersampled phantom comprising four different intensities. The original phantom of matrix size 256^2 was first sampled satisfying the Nyquist limit and reconstructed (cf. Fig. 3.21(a) top). The corresponding intensity histogram is presented in Fig. 3.21(b) (top red line) delineating four distinct peaks. The undersampled ($R = 10$) reconstruction in Fig. 3.21(a) (bottom) results in a heavily distorted histogram (cf. Fig. 3.21(b) bottom), merely depicting two peaks. Figure 3.21(c) presents gradient G_H computed from the reconstruction in Fig. 3.21(a) according to Equ. 3.45, as well as single matrices computed according to Equ. 3.46. The matrices M_I to M_{IV} comprise corrections for all four single intensity peaks. Within the algorithm the summation of the depicted single matrices yields a global correction in image space.

Reference histogram

While the previous section introduced the possibility of computing a histogram-based correction for image space artifacts on the basis of a low-entropy reference, the source of such a reference histogram is still open. Since the acquisition of a fully sampled data set is to

be avoided in the first place, within this work the feasibility of two different approaches, tailored for non-dynamic and dynamic undersampled MRI are assessed.

Non-dynamic acquisition In contrast to conventional Cartesian sampling, the sampling density of k-space is non-constant when using radial sampling. While low frequencies can be fully sampled at a certain number of spokes, higher frequencies might be undersampled. Consequently, it is possible to either reconstruct a full resolution image, impaired with undersampling artifacts, or an artifact free low-resolution image from one single raw data set. By cropping the original k-space to lower frequencies, the base resolution can be adapted in order to, together with the number of spokes, satisfy the Nyquist limit. While both artifacts and the loss in resolution degrade image quality, the impact on the image entropy, hence the intensity histogram might be completely different. Results on the evaluation of alterations to the histogram due to undersampling and loss in resolution, as well as the feasibility of the low-resolution reconstruction to serve as basis for a reference histogram are presented in section 4.1.

Dynamic acquisition Typically, real time dynamic MR acquisitions reach a temporal resolution of approximately 5 frames per second (fps). At the expense of resolution or introducing artifacts one can further improve the temporal resolution by undersampling each time frame. A very effective sampling strategy in dynamic radial acquisitions is the interleaved sampling scheme, offering the possibility to additionally reconstruct a composite image from the combination of several consecutive k-spaces. A reconstruction from the composite raw data results in an image of decreased temporal resolution, however circumvents any undersampling artifacts. Both aliasing and the loss in temporal resolution corrupt the image quality to a comparable degree. The impact on the entropy and its histogram, however, might again be of completely different nature. Evaluations regarding the entropy and intensity histogram of the composite image are carried out in section 5.1.

Advanced implementations

As widely used in histogram entropy based image registration an adaptive bin size was utilized in the proposed method. Scaling the number of bins used to sample the histogram from coarse to fine over iterations results in a balance between accuracy and step size in search space, which in turn causes an acceleration of the computational calculation.

When calculating M_t, several issues have to be taken into account. In images which are of low contrast but heavily undersampled, artifacts can cause not only broadening of intensity peaks but also an overlap of otherwise separate peaks in the histogram. Additionally, small histogram peaks are possibly broadened to the extent where the corresponding peak cannot be detected in the overall histogram. Employing the fact that the intensity histogram is a non-local metric, that is, not depending on the actual pixel position, a patched version of the aforementioned correction was implemented. Here the image matrix is subdivided in a

certain number of images patches, each comprising a reduced number of different intensities. In a theoretically ideal case, this leads to a complete separation of single intensities into separate histograms, hence a perfect division of possibly merged peaks. While the summation of these image patch histograms evidently results in the histogram of the entire image, the non-local nature of the histogram allows for the computation of separate gradient matrices. Since the separation is performed in the histogram domain it is effectively a separation in the correction of intensities, similar to the schematic separation of M_t in Fig. 3.21. Subsequently, the joint histograms of the patch image areas are calculated. These image patch joint histograms are the basis of generating the gradient matrix M_t, which in turn is applied to the entire image. This patched correction method ensures that even small image details are recognized in the histogram. To guarantee that the reconstruction is not preliminarily biased by, for instance, the first several images patched, which possibly merely contain background noise, the current image position is chosen randomly from the set of patch positions.

3.2.5 Reconstruction quality assessment

In order to judge the performance of the resulting reconstruction it is crucial to define a universal measure of image quality. When performing evaluations of novel reconstruction methods for sub-Nyquist sampling usually a fully sampled scan is performed undergoing subsequent data reduction. Hence, after the iterative reconstruction it is possible to calculate the deviation to the fully sampled reconstruction.
Commonly, parameters such as the peak signal to noise ratio (PSNR)

$$\mathrm{PSNR} = 10 \cdot \log_{10}\left(\frac{\max(\mathrm{I}_1)^2}{\mathrm{MSE}}\right) \tag{3.48}$$

are used to assess the quality of a reconstruction. However, the PSNR is not feasible in all cases. While it is simple to calculate and has clear physical meaning, it is not very well matched to the *perceived* visual quality [144–146]. To overcome the limitations of PSNR Wang et al. [147] developed a measure of structural similarity (SSIM) that compares *local* patterns of pixel intensities for luminance and contrast and shows very consistent results. The SSIM-map of two images x and y is calculated via:

$$\mathrm{SSIM}(x,y) = \frac{(2\mu_x\mu_y + c_1)(2\sigma_x y + c_2)}{(\mu_x^2 + \mu_y^2 + c_1)(\sigma_x^2 + \sigma_y^2 + c_2)} \tag{3.49}$$

with

- $\mu_{x/y}$ the average of x and y, respectively
- $\sigma^2_{x/y}$ the average of x and y, respectively
- σ_{xy} the covariance of y
- $c1, c2$ variables to stabilize the division with weak denominator.

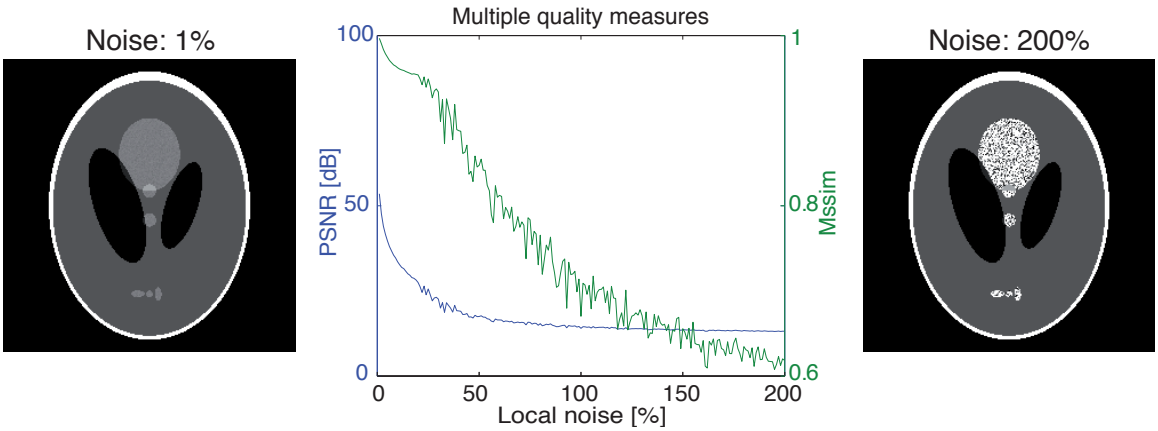

Figure 3.22: Comparison of the sensitivity of peak signal to noise ratio (PSNR) and structural similarity measure (MSSIM) for image quality assessment. The evaluated Shepp-Logan phantom was corrupted with noise of increasing magnitude for only one intensity. The MSSIM shows sensitivity to local changes in the image over a greater range of noise.

Within this work the SSIM value is always calculated as the mean of the SSIM map, hence:

$$\mathrm{MSSIM} = \frac{1}{mn} \sum_{i=0}^{m-1} \sum_{j=0}^{n-1} \mathrm{SSIM}(i,j). \tag{3.50}$$

Figure 3.22 demonstrates the quality assessment via MSSIM on a simple example.
Gradually increasing noise is introduced to the Shepp-Logan phantom. The described histogram regularization can affect single image intensities differently. Hence, it is crucial to detect local image errors, even if the rest of the image is reconstructed perfectly. To simulate such a situation, noise is merely added in the region of originally intensity 0.3. Using the original phantom and the noisy representation both the PSNR and the MSSIM index are calculated and plotted in Fig. 3.22. While both parameters show similar behavior up to a noise level of approximately 10%, the sensitivity of PSNR decreases at higher noise levels. The MSSIM in contrast detects differences in the images even at very high noise levels.
Consequently, in the following assessments, if appropriate, the MSSIM index was employed as a measure of reconstruction quality.

3.2.6 Summary

This chapter demonstrated the different appearances of aliasing artifacts depending on the used sampling scheme. Pseudo random sampling strategies result in artifacts manifesting comparable to noise in the image domain. Radial undersampling, hence the reduction of the number of spokes has a similar impact effecting the whole image, regardless of the magnitude of the reduction factor. The streak-like nature of polar aliasing artifacts can best be observed on the point spread function using the according number of used spokes. Each

single point in image space is surrounded by a artifact free disc, whose radius is determined by the Nyquist condition. Beyond this radius radial streak artifacts cover remaining image areas.
In order to reconstruct artifact free images even from incomplete data an iterative approach to finding the anticipated image representation was introduced. After finding universal attributes associated with an artifact-free image, it is possible to employ these image features as *a priori* information constraining the search for the 'correct' solution. In addition to known features such as Wavelet and finite difference sparsity, in this chapter the notion of Shannon entropy and histogram entropy was introduced as measure of undersampling artifacts. It was demonstrated that incoherent artifacts such as radial aliasing cause the entropy modulus to increase and more important peaks in the intensity histogram to spread out.
The incorporation of the intensity histogram as regularization in an iterative reconstruction framework involves the calculation of the descent direction when using the conjugate gradient approach to solve the optimization. In this chapter the concept of mutual information in a 2D histogram was introduced and it was explained how a intermediate projection of the differentiated joint histogram, calculated from the impaired image and a low-entropy reference can be used as gradient for the optimization task.
In order to assess the success of artifact suppression the structural similarity (MSSIM) index was introduced, which proofs to be more suitable for the evaluation of image quality than MSE or PSNR especially in the case of the introduced reference histogram constrained algorithm.

4 Reference Histogram Constrained Artifact Suppression (RHiCA) for Radially Undersampled Magnetic Resonance Imaging

As briefly mentioned in Subsection 3.2.4, the low-resolution or Nyquist reconstruction yields an aliasing-free representation of the acquired undersampled radial data. The following chapter presents results on the assessment of the impact of reduced spatial resolution on the entropy and the intensity histogram of a reconstruction in comparison to the effect of undersampling. Subsequently the performance of a Nyquist reference histogram based reconstruction on numerical simulations (cf. Subsection 4.2.1) as well as *in vivo* MRI head examinations of a healthy volunteer are evaluated (Subsection 4.2.2). In addition to the assessment of the iterative reconstruction solely based on a histogram constraint, the combination of different regularization functions is demonstrated.

4.1 Low-entropy Nyquist reference

In order to examine the impact of undersampling on the image entropy as universally as possible, the point spread function (PSF) of the employed radial sampling strategy is assessed (see Fig. 4.1).
Figure 4.1(a) depicts a cut through the PSFs when reconstructing to the full matrix size using a decreasing number of spokes n'_s. While the width of the PSF in the center complies with the full spatial resolution, heavy undersampling artifacts are introduced in the exterior areas, resulting in an early entropy increase, as observable in Fig. 4.1(c) (dashed line).
As aforementioned the radial acquisition schemes yields a non-constant sampling density in k-space. Consequently, a certain number of radial spokes specifies a circle around the center of k-space, within which $\Delta k_s = \Delta k_r$ holds, hence Equ. 3.12 is satisfied. Thus it is possible to calculate the maximum number radial k-value or the maximum number of radial sample points n_r^{max} via Equ. 3.12 together with the number of acquired spokes n'_s. The reconstruction results in an image of decreased resolution ($n_r^{max} \times n_r^{max}$).
While simply setting radial sampling points greater than n_r^{max} to zero reduces the resolution according to the Nyquist limit, it also causes undesirable truncation artifacts in the reconstruction. In order to avoid these additional artifacts it is necessary to generate a smooth transition in k-space by applying a Gaussian window rather than a simple rect-function.

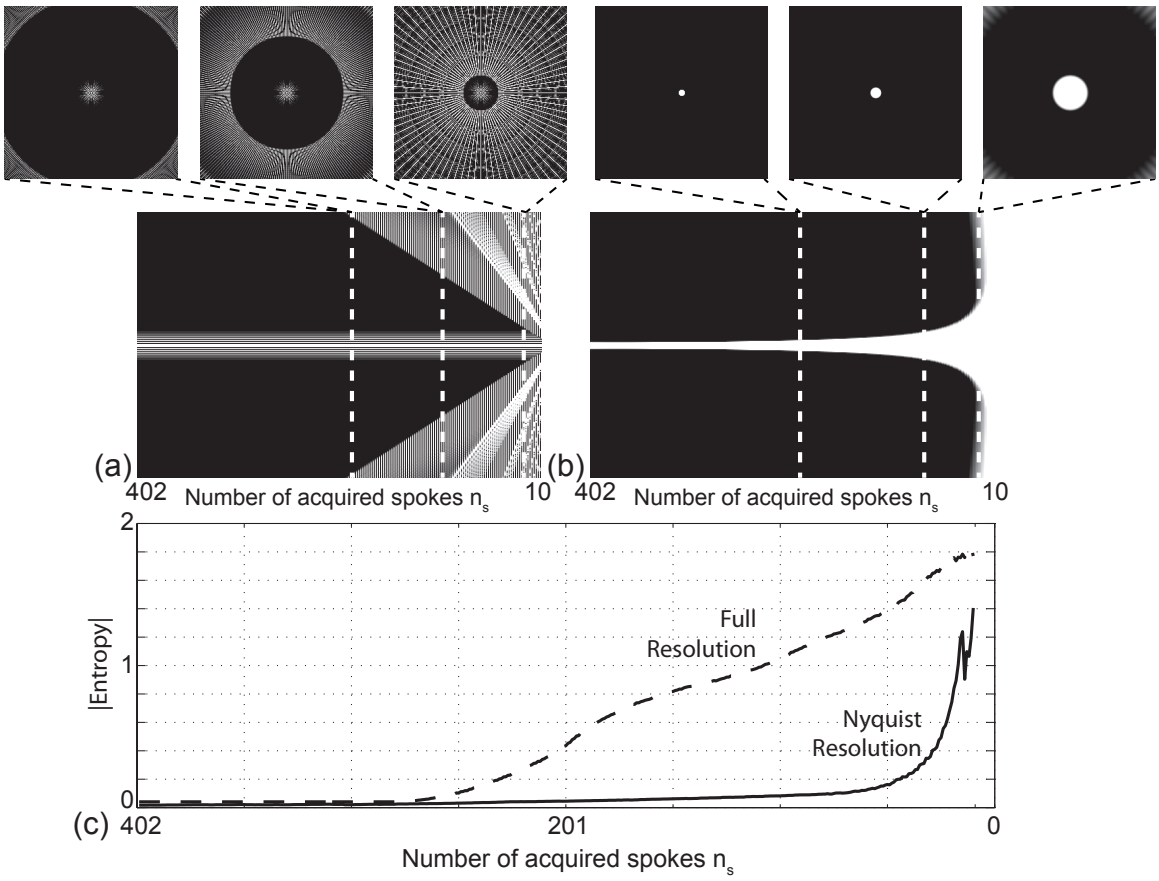

Figure 4.1: Point spread functions (PSF) with decreasing number of spokes. (a) Full Resolution (256^2) and (b) Nyquist Resolution PSF of radial sampling using 402 (full sampling) to 10 (undersampling factor of 40) spokes. (c) Increase of Shannon's entropy of the PSF with decreasing number of spokes for the full resolution and the Nyquist reconstruction.

Consequently, every single radial spokes is multiplied with the Gaussian function

$$e^{-\frac{1}{2}\left(\frac{k}{c}\right)^2}, \tag{4.1}$$

where the parameter c is set according to

$$c = \frac{n_r^{max}}{n_r \; 2\sqrt{(2\log(2)}}. \tag{4.2}$$

Hence, n_r^{max} yields the full width at half maximum of the Gaussian function. Hereby k-space is limited to a disc satisfying the Nyquist limit while avoiding truncation artifacts in the reconstruction.
Performing this procedure results in a completely different behaviour of the PSF when reducing the number of acquired spokes (cf. Fig. 4.1(b)). While the spatial resolution of the reconstruction (width of the central peak) clearly decays with a decreasing number of

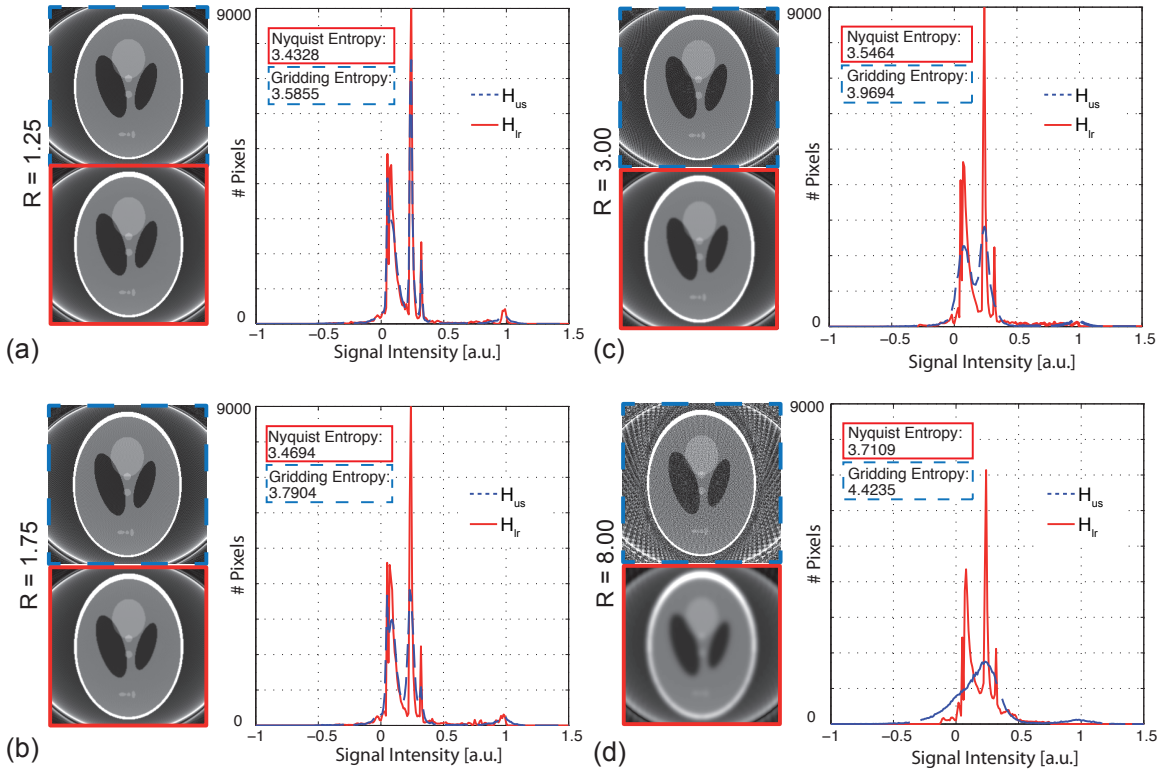

Figure 4.2: Effect of undersampling on the reconstruction and intensity histogram computed from the full resolution reconstruction (blue/dashed histogram) and the low resolution reconstruction according to Nyquist (red/solid histogram) for four different reduction factor from $R = 1.25$ to $R = 8.00$.

spokes, the effect on the image entropy is minor when compared to the effect of undersampling artifacts. The solid graph in Fig. 4.1(c) shows that the entropy of the Nyquist reconstruction is almost unaffected by the decreasing number of spokes up to an undersampling factor of 10 (40 spokes). Consequently, it can be stated that by adjusting the reconstruction's resolution according to the Nyquist limit, it is possible to generate a low-entropy representation of the undersampled raw data set.

The impact of undersampling and loss of spatial resolution on the intensity histogram is simulated on the Shepp-Logan phantom sampled with a decreasing number of spokes (cf. Fig. 4.2). Undersampled data is reconstructed to the full resolution depicted in the blue dashed framed images X_{us} and to a reduced resolution according to the Nyquist limit shown in the red framed images X_{lr}. The corresponding histograms H_{us} and H_{lr} are computed from each reconstruction. The reconstructions clearly demonstrate that, while the image quality of both X_{us} and X_{lr} decays severely with a decreasing number of spokes, the histogram H_{lr} as well as the entropy of X_{lr} are almost unaffected. Even at an undersampling factor of 8 (50 spokes), the Nyquist histogram is still comparable to the fully sampled histogram.

While H_{lr} computed from the entire image, as performed here, might serve as a sufficient reference for small reduction factors and simple objects, higher R-values combined with

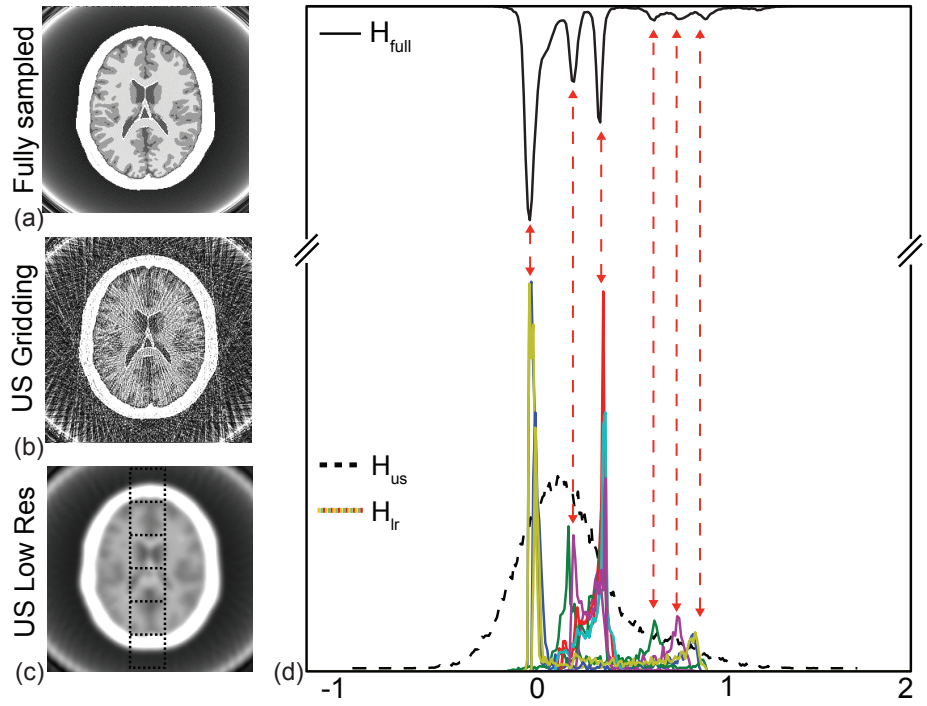

Figure 4.3: Low-resolution reference. (a) Gridding reconstruction from fully sampled (402 spokes) data. (b) Gridding reconstruction from undersampled data (R=10). (c) Gridding reconstruction with a base resolution of $n'_b = \frac{2}{\pi} n'_s$. (d) According histograms: upside-down from reconstruction (a), dashed line from reconstruction (b), coloured solid lines from one single column of image patches marked in (c).

more complex structures call for a more sophisticated computation of H_{lr}.
As introduced in Subsection 3.2.4 it is possible to subdivide the image in single patches, which serve as basis for the computation of separate histograms. The benefit of the introduced patch mode for the recovery of histogram peaks is assessed on a simulated head MRI. The numerical head phantom was developed by *Brainweb* [148–151]. The original phantom of matrix size 256^2 was radially sampled with a reduction factor of 10 and reconstructed using the NUFFT algorithm.
While the entropy of the fully sampled reconstruction (cf. Fig. 4.3(a)) yields a value of $|E| = 4.0$, undersampling artifacts in Fig. 4.3(b) cause an increase to a value of $|E| = 5.1$. The low-resolution reconstruction from the same data set, however, yields an entropy value of $|E| = 4.1$. Evidently, while the entropy of the low-resolution reconstruction might be comparable to the fully sampled reconstruction's entropy, the image quality is heavily degraded. Consequently, the low-resolution image itself is not feasible as reference for the reconstruction.
Figure 4.3(d) depicts histograms calculated from the three different normalized reconstructions using a bin size of 0.01. The single graphs are scaled for best visual appearance and comparability. The upside-down graph H_{full} resembles the histogram of the fully sampled

reconstruction (401 equally spaced spokes), presenting narrow highly populated peaks. In contrary, the histogram H_{us} of the basic NUFFT gridding reconstruction (Fig. 4.3(b)), depicted as dashed line merely consists of one broad peak, due to heavy aliasing in the image. The coloured solid line histograms (H_{lr}) computed from one example column of low-resolution image patches (see Fig. 4.3(c)) demonstrate the recovery of all major intensity peaks from the combination of single image patch histograms.
In conclusion the low-resolution Nyquist reconstruction yields not only an image space representation of reduced entropy, but also a histogram which is unaffected by undersampling up to a very high factor of reduction. Consequently, the Nyquist histogram is employed as reference for the histogram gradient G_H introduced in Subsection 3.2.4.

4.2 Application

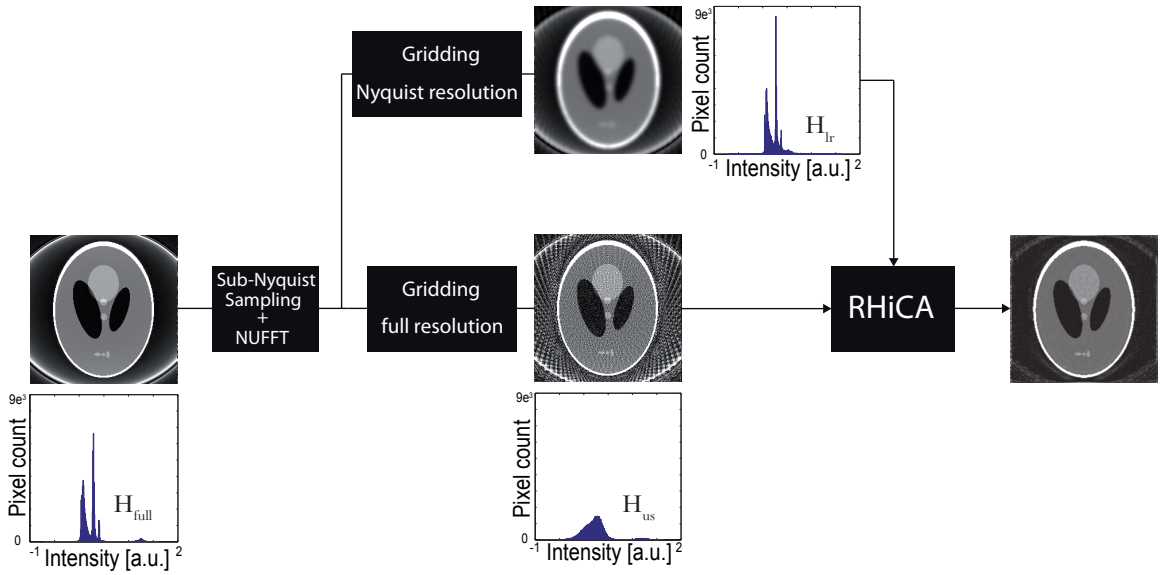

Figure 4.4: Graphical outline of RHiCA

The RHiCA algorithm is based on the correction of undersampling artifacts by adapting the impaired histogram to a low-entropy reference histogram. The reconstruction is obtained by solving the following constrained optimization problem:

$$\underset{X}{\operatorname{argmin}} \left(||\Phi(X) - y||_2 + \lambda_H \, \mathbf{R}_H \right) \tag{4.3}$$

$$\text{with} \qquad \mathbf{R}_H = ||H_{us} - H_{lr}||_2$$

Here y denotes the acquired multi-coil raw data, λ_H is the regularization parameter, weighting the histogram constraint $\mathbf{R}_H$, namely the similarity of the reference histogram H_{lr} and the target histogram H_{us} measured with the l_2-norm.

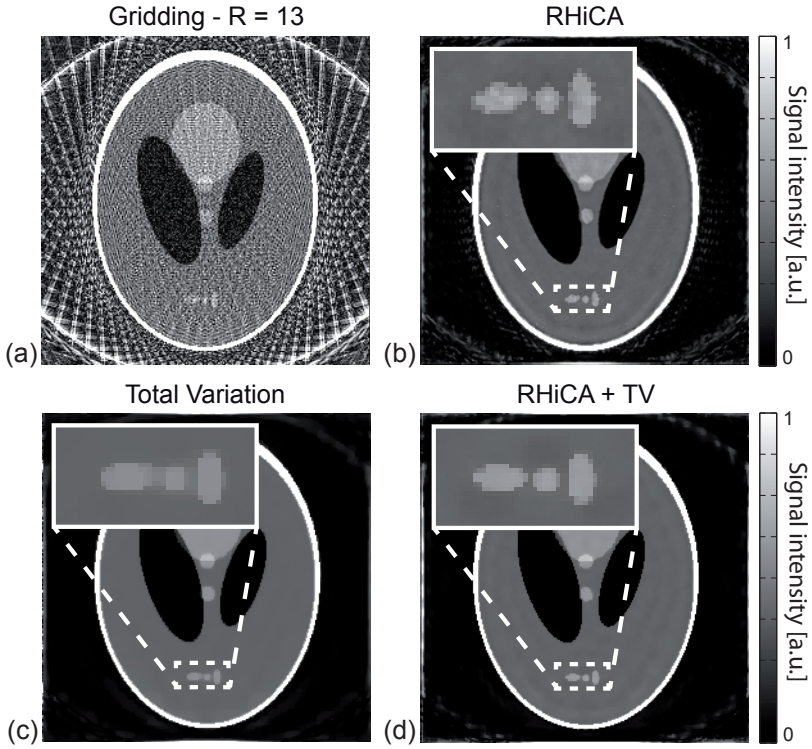

Figure 4.5: Application of RHiCA on a simulated multi-coil MR acquisition on the Shepp-Logan phantom. (a) Gridding reconstruction presenting severe undersampling artifacts. (b) RHiCA: Successful suppression of almost all of the aliasing artifacts, while maintaining details and edge fidelity. (c) Total variation: Superior image smoothness, while details get blurred and overlap. (d) Hybrid regularization: Both smoothness and detail fidelity.

The first term in Equ. 4.3 denotes the raw data fidelity, that is, the difference between the acquired multi-coil k-space data y and the back transformed resulting image X after each iteration step. The transformation Φ between image space and multi-coil k-space is realized using NUFFT and the coil sensitivity weighted complex summation of single coil images. The second term of Equ. 4.3 is a weighted regularization, maximizing the similarity between the corrupted target and the reference histogram.
The optimization is implemented using the non-linear conjugate gradient descent known from CS with Fletcher-Reeves update based on the implementation of Lustig et al. [38] in Matlab (Mathworks, Natick, US).
Figure 4.4 presents an overview of the iterative histogram constrained reconstruction, using the Nyquist reconstruction as reference.

4.2.1 Numerical simulations

In order to assess the performance of RHiCA on an object well-known and frequently used in the assessment of novel reconstruction methods, a radial multi-coil measurement

was simulated on a Shepp-Logan phantom of matrix size 256^2 with added complex-valued Gaussian noise ($\sigma = 0.02$). The data set was simulated by weighting the image with 8 pre-calculated coil profiles and using forward projection via NUFFT generating a dataset of size $256 \times 31 \times 8$, corresponding to an undersampling factor of 13. Angles for all radial simulations were chosen conventionally with increments of $\theta = \pi/n'_s$. The starting target image was reconstructed via NUFFT-regridding. The reference histogram was generated as described, according to Equ. 3.12. The RHiCA algorithm was applied in patch mode with a number of 16 image patches. Regularization parameters were chosen for best visual image quality and minimal mean structural similarity index MSSIM.
Figure 4.5 presents the results of the application of RHiCA on the undersampled Shepp-Logan phantom (Fig. 4.5(a)). The RHiCA reconstruction ($\lambda_H = 0.01$) in Fig. 4.5(b)

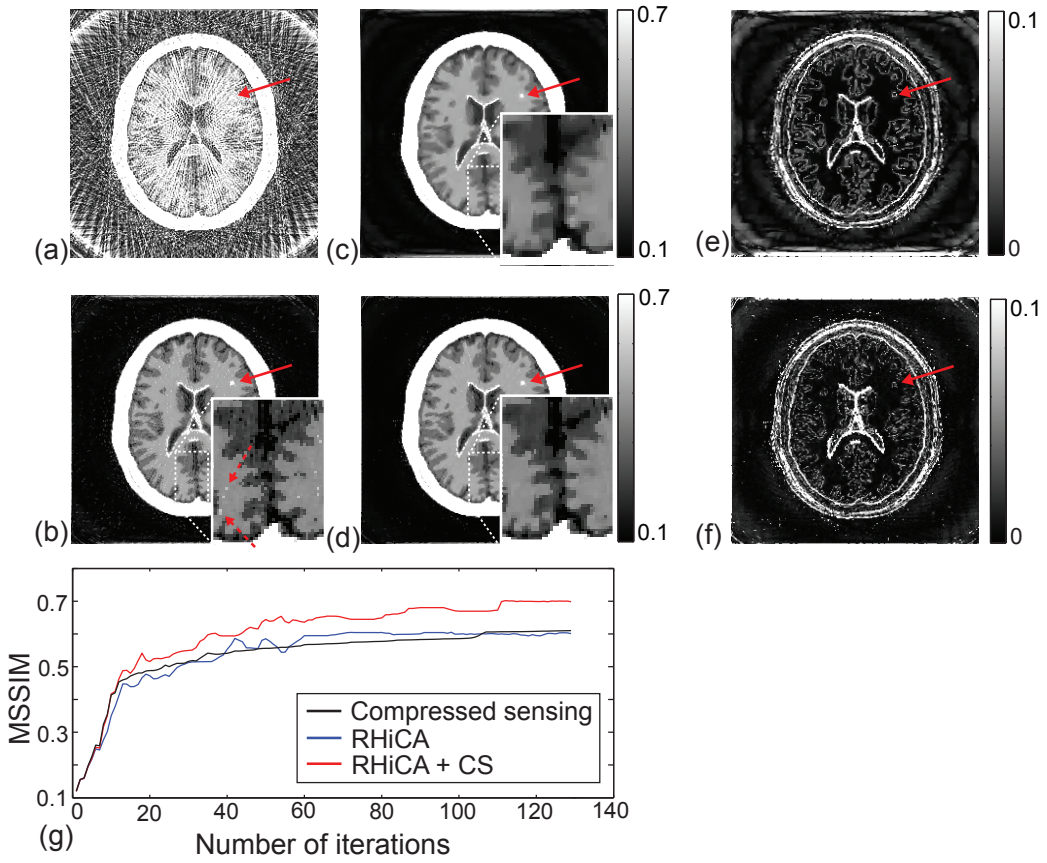

Figure 4.6: Application of RHiCA on a simulated multi-coil MR acquisition of a numerical head phantom. (a) Gridding reconstruction of an undersampled ($R = 10$) data set. (b) Iterative reconstruction using RHiCA ($\lambda_H = 5 \cdot 10^{-3}$). (c) Reconstruction using compressed sensing ($\lambda_{WL} = 8 \cdot 10^{-3}$, $\lambda_{TV} = 5 \cdot 10^{-3}$). (d) Reconstruction using RHiCA and CS ($\lambda_H = 1 \cdot 10^{-2}$, $\lambda_{WL} = 4 \cdot 10^{-3}$, $\lambda_{TV} = 2 \cdot 10^{-3}$). (e) Error map calculated as difference between (c) and the original. (f) Error map calculated from (d). (g) Structural similarity index versus iterations.

presents an almost complete suppression of aliasing artifacts and noise, paired with a high edge and detail fidelity (see enlarged area). While large areas of same intensity are presented smooth and artifact-free, details in the image, corresponding to small peaks in the histogram show residual artifacts and inhomogeneity.
In order to be able to rate the performance of RHiCA, the same data set was reconstructed on the basis of compressed sensing using total variation regularization ($\lambda_{TV} = 0.008$). Comparing the RHiCA-result to the CS-reconstruction (Fig. 4.5(c)) clearly exposes strength and weaknesses of both approaches. Especially when focussing on details, as depicted in the enlarged area, RHiCA presents high detail fidelity, while TV offers good homogeneity in the image, however reduced spatial resolution. Since these attributes are complementary, the resulting reconstruction from the combination ($\lambda_H = 0.01$, $\lambda_{TV} = 0.005$) of both constraints (Fig. 4.5(d)) shows the best visual results in delineating small structures and smoothness in the depicted intensities.
An additional numerical simulation was carried out on the head phantom introduced in section 4.1. The original design of the phantom was additionally corrupted with complex valued Gaussian noise ($\sigma = 0.02$). A small (radius = 2.5 pixels) hyper-intense structure of unique intermediate intensity was added to the phantom in the upper right corner of the white brain matter (red arrow), simulating a pathological finding, not part of any other major intensity peak. Again a multi-coil data set was generated by weighting the image with 8 pre-calculated coil profiles and using forward projection via NUFFT generating a dataset of size $256 \times 41 \times 8$, corresponding to a reduction factor of $R = 10$. The initial guess image (cf. Fig. 4.6(a)) was reconstructed via NUFFT-regridding and sensitivity weighted summation of single coil images.
Figure 4.6 presents the results of the application of RHiCA on the undersampled head phantom. Undersampling artifacts are successfully suppressed in the histogram entropy constrained reconstruction in Fig. 4.6(b), when compared to the conventional result (Fig. 4.6(a)). While correct intensities, details and edges are recovered, the reconstruction also shows single pixels of residual artifacts, as indicated by dashed arrows. The compressed sensing reconstruction using both total variation ($\lambda_{TV} = 5 \cdot 10^{-3}$) and wavelet sparsity ($\lambda_{WL} = 8 \cdot 10^{-3}$) (Fig. 4.6(c)) again presents as a result of superior image smoothness, however looses details and introduces blurring at intensity steps. Combining RHiCA and CS ($\lambda_H = 1 \cdot 10^{-2}$, $\lambda_{WL} = 2 \cdot 10^{-3}$, $\lambda_{WL} = 4 \cdot 10^{-3}$) (Fig. 4.6(d)) shows the best results in the recovery of small structures and smoothness in the depicted intensities. The added small structure simulating a pathological region of unique intensity (red arrow) was successfully recovered in all reconstructions, demonstrating the feasibility to recover both details in image and histogram space.
These findings can also be observed on the error maps (Figs. 4.6(e/f)) calculated as difference between the fully sampled reconstruction and the results in Figs. 4.6(c/d). Figure 4.6(f) demonstrates reduced errors especially around intensity steps, the included pathology and in the background. Figure 4.6(g) presents the MSSIM values for all three reconstruction approaches versus the number of iterations, demonstrating equal image quality in the RHiCA (MSSIM = 0.60) and CS (MSSIM = 0.61) reconstruction and superior quality in the combination of both yielding a value of MSSIM = 0.71.

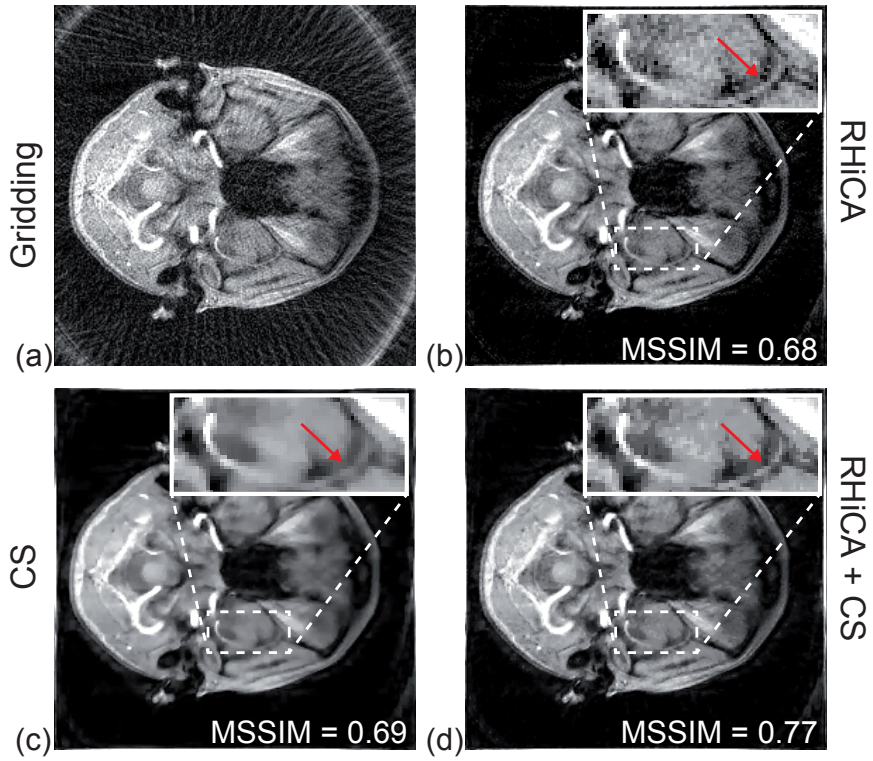

Figure 4.7: Results of RHiCA on an MRI slice of a human head. (a) Gridding reconstruction. (b) RHiCA ($\lambda_H = 8 \cdot 10^{-3}$). (c) Compressed sensing reconstruction ($\lambda_{TV} = 5 \cdot 10^{-3}$, $\lambda_{WL} = 8 \cdot 10^{-3}$) (d) Hybrid regularisation ($\lambda_H = 1 \cdot 10^{-2}$, $\lambda_{TV} = 3 \cdot 10^{-3}$, $\lambda_{WL} = 5 \cdot 10^{-3}$).

4.2.2 *In vivo* experiments

The performance of RHiCA on MRI measurements was assessed on a 3D head MRI measurement of a healthy human volunteer (see Fig. 4.7). Data was acquired with a 3.0T MR-scanner (Biograph mMR, Siemens AG, Healthcare Sector, Erlangen, Germany) at the Klinikum Rechts der Isar (Munich, Germany) using a radial VIBE sequence acquired as 'stack of stars' scheme and bitreverse reordering of radial spokes (TR = 4.44 ms, TE = 2.21 ms, slice thickness = 12 mm, matrix = 352×352, FOV = 249×249 mm, #spokes = 1024) with a 6-channel head coil. The RHiCA algorithm was applied on subsets of the fully sampled data set with a reduction factor of $R = 8$, using a number of 36 images patches. RHiCA (Fig. 4.7(b)) shows high fidelity in maintaining image details and contrast properties. Aliasing and noise in the background as well as within the measured object are suppressed efficiently, without perceptual loss in spatial resolution. CS (Fig. 4.7(c)) presents superior image smoothness, however accompanied by image blurring, hence loss in effective spatial resolution. Similar to the simulations, when combining both regularizations, the reconstruction (Fig. 4.7(d)) result is simultaneously homogeneous and shows high detail fidelity as demonstrated in the enlarged area. The marked blood vessel (red arrow) within this slice is delineated most accurately in the hybrid constraint image. These visually ap-

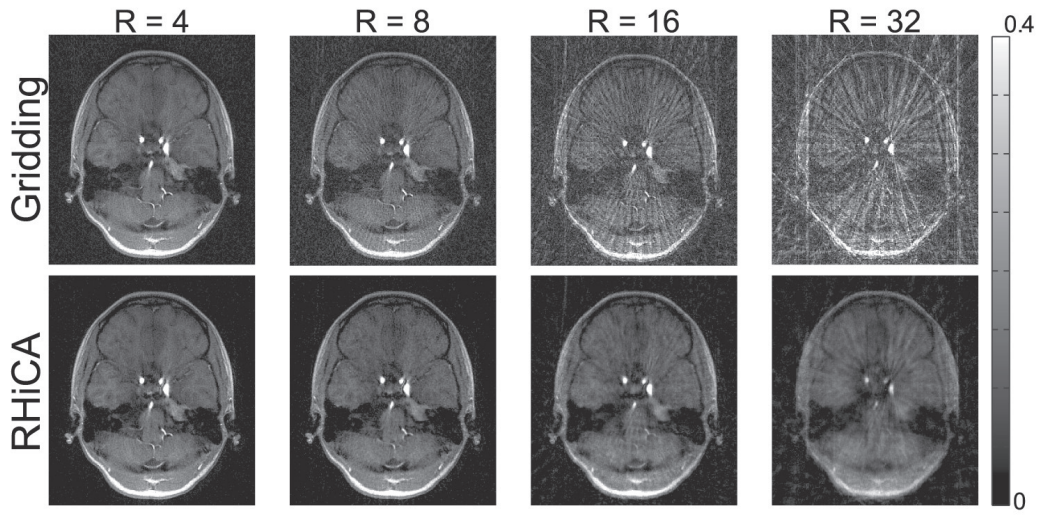

Figure 4.8: Results of RHiCA on a MRI slice of a human head. First Row: Gridding reconstruction of undersampled data sets with a decreasing number of used spokes from 128 to a number of merely 16. Second Row: Results after RHiCA application ($\lambda_H = 7 \cdot 10^{-3}$).

parent results are confirmed by the calculated MSSIM values, which increase from 0.68 for the RHiCA case, over 0.69 using CS to a maximum value of 0.77 when combining all regularizations.
Figure 4.8 presents the result of RHiCA applied to an additional acquisition on the same volunteer with a reduced resolution of matrix = 320×320, to avoid the corruption with noise. All other measurement parameters were chosen equivalent to the first measurement, except the ordering of sampling angles, which was set to *golden angle* in this acquisition. The evaluation focusses on how RHiCA manages to correct for increasing reduction factors. While the first row displays the gridding reconstruction of k-space data utilizing a decreasing number of spokes, the second row presents the respective reconstruction using RHiCA. According to Equ. (3.12) the number of spokes corresponds to reduction factors of $R = 4$ to $R = 32$. The gridding reconstructions suffer from increasingly strong streaking artifacts. In contrary, when applying the RHiCA algorithm, artifacts at reduction factors of $R = 4$ and $R = 8$ are completely removed and noticeably reduced at higher reduction factors.

4.3 Summary

This chapter demonstrated that in addition to the artifact impaired image, a low-entropy representation can be generated from the same initial raw data set. By reducing the spatial resolution of the reconstruction it is possible to fabricate an image, whose histogram very closely resembles the histogram of a fully sampled reconstruction. This low-resolution reconstruction histogram is used as reference in order to correct for the effect of under-

sampling on the histogram and as a result suppress aliasing in the image domain. The performance of the histogram constrained reconstruction for single image acquisition MRI when using the Nyquist resolution reconstruction as low-entropy reference was assessed on several different objects. As proof of principle the algorithm was applied on two numerical simulations. The complementary impact of RHiCA and compressed sensing, results in the image of best perceivable quality. Especially image details are nearly perfectly recovered while still enforcing image smoothness in the remaining image areas.
In the *in vivo* experiments two different slices were acquired comprising several intensities as well as fine detail such as hyper-intense vessels. Again the results demonstrate the best performance on suppressing artifacts while recovering detail when employing the hybrid regularization of RHiCA and TV. In the final experiment the effectiveness of solely RHiCA was evaluated at increasingly severe undersampling. Up to a reduction factor of 8 perfect recovery could be achieved. At higher factors of 16 and 32 artifacts are still corrected for to a large degree, however, images show remaining streaks especially in the background as well as minor residual blurring.

5 Rapid Dynamic Radial MRI via Low-Resolution Image Enforced Histogram Constrained Reconstruction (RHiCA-LR)

In the context of dynamic MRI, radial interleaved sampling has proven to be a very effective sampling strategy. Starting from one dynamic data set it is possible to reconstruct three separate images of different information content. An aliasing impaired reconstruction (X_{us}) of *full temporal* and *full spatial* resolution can be generated from each single undersampled k-space by basic regridding. In addition, cropping each radial spoke to a base resolution $n'_b = 2/\pi \; n'_s$, hence satisfying Equ. 3.12 yields the basis of an aliasing-free reconstruction X_{lr} of *full temporal* but *low spatial* resolution as introduced for the RHiCA algorithm. Finally, the composition of n_s/n'_s consecutive k-spaces generates a fully sampled raw data set resulting in an aliasing-free reconstruction X_{comp} of *full spatial* but *low temporal* resolution. The final reconstruction task is to utilize both latter reconstructions in order to correct for artifacts in the initial reconstruction without incorporating temporally averaged structures. The following chapter comprises a detailed evaluation of the impact of temporal averaging on the intensity histogram, hence the image entropy in comparison to the effect of aliasing artifacts. The feasibility of the composite histogram as low-entropy reference will be demonstrated on the basis of a point spread function evaluation and numerical simulations (cf. section 5.1). In addition an image space regularization utilizing a single frame low-resolution reconstruction X_{lr} is implemented to guarantee overall contrast fidelity. In order to assess the performance of both regularizations, the developed method is applied on numerical simulations and *in vivo* data. The reconstruction is first assessed on two numerically simulated temporally resolved MRI measurements (cf. Subsection 5.2.1). Subsequently, two native dynamic cardiac MRI acquisitions of healthy volunteers are reconstructed using the iterative histogram constrained method and compared to a standard iterative SENSE algorithm (cf. Subsection 5.2.2). The approach using X_{lr} as image space reference and H_{comp} as histogram reference is termed RHiCA-LR in the following.

5.1 Low-entropy composite reference

Equivalent to the static case in RHiCA, the effect of dynamic undersampling can be observed in a universal manner, when calculating the point spread function of the imaging system. Since the aim is to image dynamic objects the point spread function is simulated to be moving one pixel per frame. The simulation comprehends 40 frames of the PSF of matrix

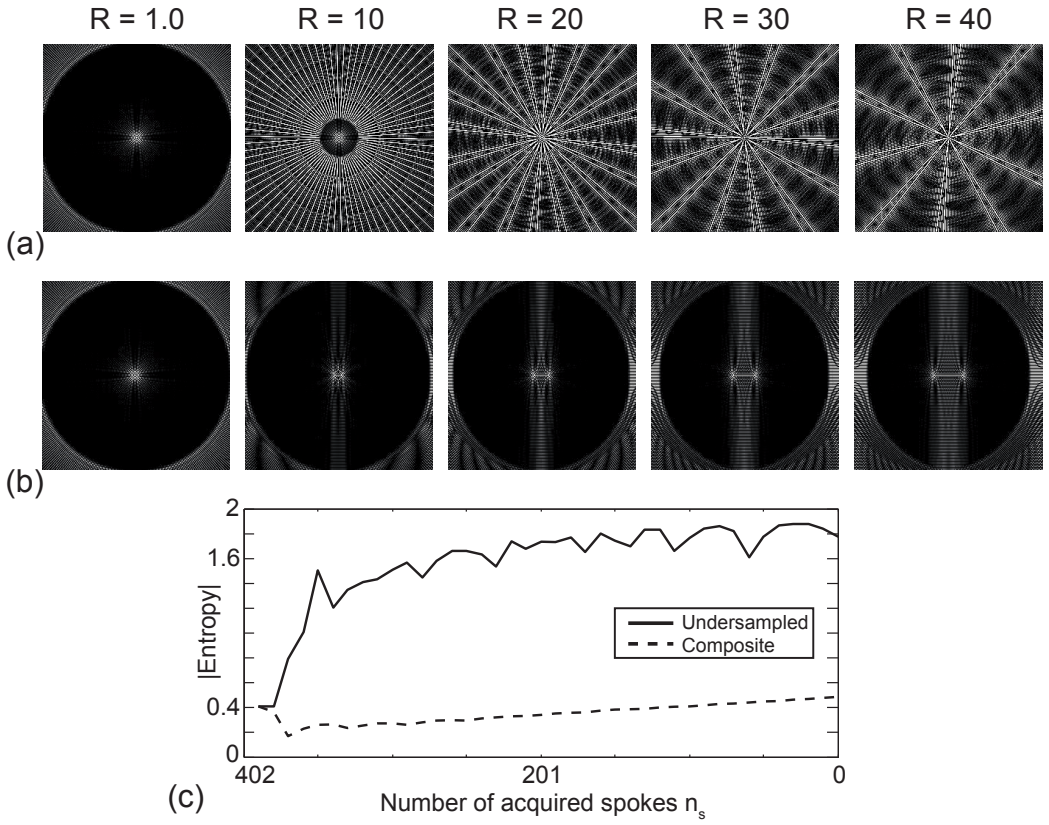

Figure 5.1: Evaluation of the point spread function of a dynamic system sampled radially interleaved with an increasing reduction factor R. (a) Reconstruction of single time frames to the full base resolution, introducing strong undersampling artifacts. (b) Composite reconstruction, combining R consecutive k-spaces. Images are free of aliasing artifacts, however lose temporal resolution, resulting in blurring of the dynamic image areas. (c) Impact of both image corruptions on the Shannon entropy.

size 256^2. The single frames were radially interleaved sampled and reconstructed separately and as a composite image in a sliding window manner at an increasing rate of the reduction factor R. When reconstructing every single k-space separately (see Fig. 5.1(a)), a decreasing number of spokes results in increasingly severe streaking in the reconstruction. Additional pixel intensities due to undersampling artifacts cause the entropy of the image (see Fig. 5.1(c) solid line) to increase very rapidly. When composing consecutive k-space trajectories (see Fig. 5.1(b)), images show poor temporal resolution, however no undersampling artifacts. As evident from Fig. 5.1(c) the impact of decreased temporal resolution in the image is negligible when compared to the effect of undersampling. Hence, by composing k-spaces in order to satisfy Equ. (3.12), it is possible to compute a low entropy representation of the undersampled data set.
The impact of incomplete sampling on both the reconstruction and the respective histograms

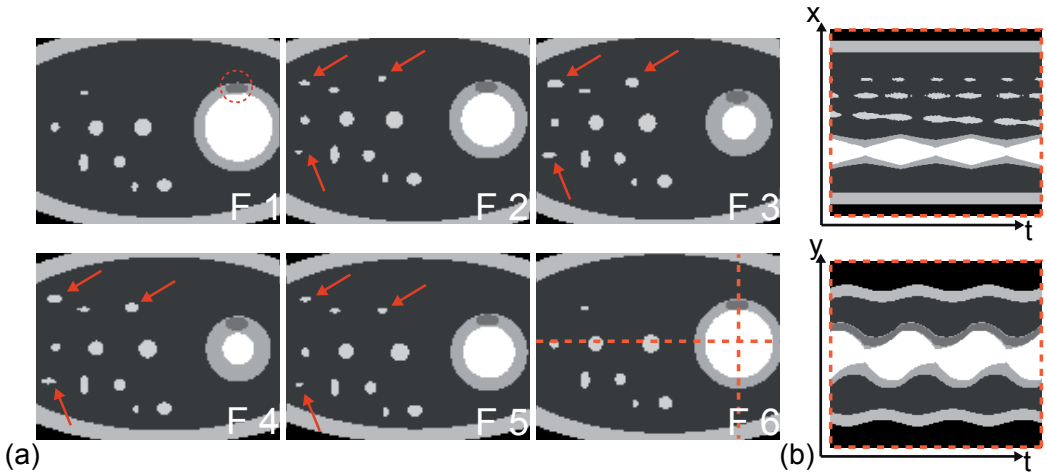

Figure 5.2: (a) Anatomical setting used for simulation. Red arrows mark vessels which vanish from the simulated slice due to respiratory motion. (b) Time-dependent evolution of slices, running horizontally (top) and vertically (bottom) through the phantom as indicated in F6.

is assessed on a numerical simulation. The designed phantom (see Fig 5.2(a)) aims to simulate an axial slice of the human thorax during a dynamic acquisition. It comprises a ring of fatty tissue, pulmonary vessels (arrows mark vessels of temporally varying diameter) and a schematic cut through the myocardium. Figure 5.2(b) depicts a time-dependent horizontal (top) and vertical (bottom) cut along the dashed lines marked in frame F6. The simulation covers 3 cardiac cycles with respiratory and cardiac motion.
Figure 5.3 presents reconstructions of data sets with an increasing reduction factor from $R = 1.0$ (Fig. 5.3(a)) to $R = 16$ (Fig. 5.3(d)) to single time frames (top) and composite images (bottom). The right column in 5.3 depicts the according histograms calculated from the reconstructions in comparison to the original histogram calculated from the fully sampled reconstruction.
Artifact-free images, hence, images of small entropy correspond to a histogram with narrow, highly populated intensity peaks (cf. Fig. 5.3(a) - H_{full}). In contrary, additional pixel intensities due to undersampling artifacts in the image cause histogram peaks to spread out and overlap (H_{us} in Fig. 5.3(b)) or even merge (H_{us} in Fig. 5.3(c/d)). Evidently also the composite reconstruction is heavily corrupted by blurring and temporal averaging (cf. arrows in Fig. 5.3), prohibiting the use of X_{comp} as image space reference. The corresponding histograms (H_{comp} - red/solid lines) in Fig. 5.3, however, demonstrate that the impact of loss in temporal resolution on the intensity histogram is only minor when compared to the aliasing corrupted histograms (H_{us} - blue/dashed lines). Since position and extent, hence intensity and intensity variation of H_{comp} are comparable to the fully sampled case, the composite image histogram serves as a low-entropy reference for the correction of H_{us} and as a consequence of artifacts in the high temporal resolution single frame images.

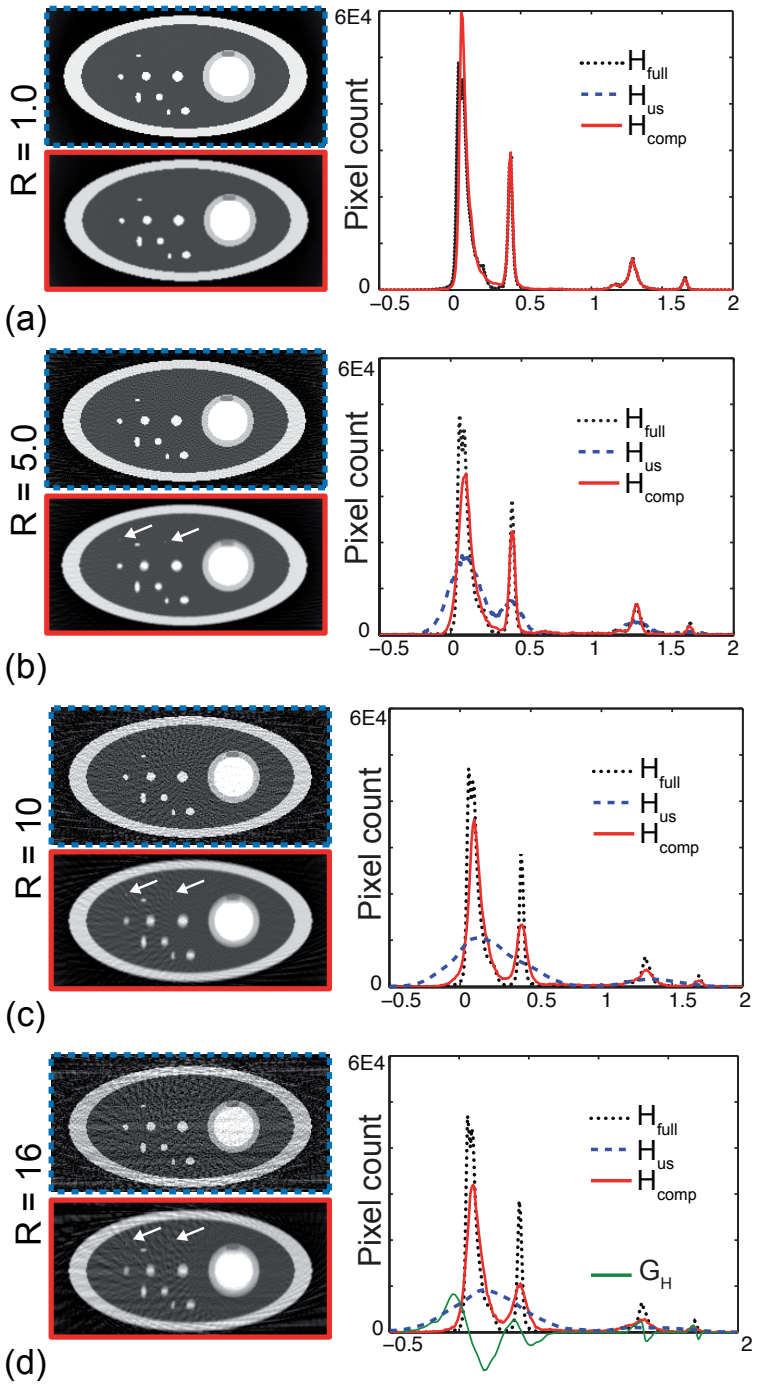

Figure 5.3: Left column: Reconstructions from dynamically acquired data sets with increasing reduction factor ($R = 1.0$ - $R = 16$). Top image: Full temporal resolution. Bottom images: Composite images, arrows mark structures appearing due to temporal averaging. Right column: Corresponding histograms in comparison to the true full resolution image histogram (H_{full}). G_H denotes the gradient calculated from H_{comp} and H_{us}.

5.2 Application

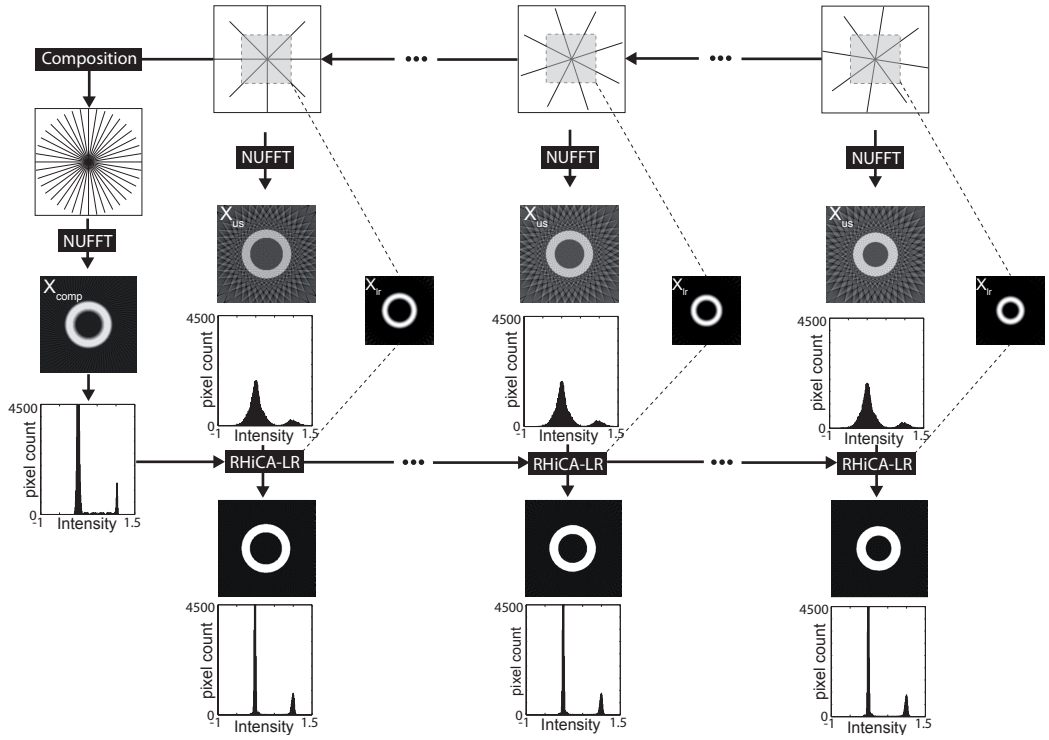

Figure 5.4: Graphical outline of dynamic RHiCA-LR

Equivalent to the basic RHiCA algorithm, the core of the RHiCA-LR reconstruction is the regularization utilizing a low-entropy reference histogram H_{comp} computed from the composition of consecutive temporally resolved radial k-space trajectories. In addition, comparable to the PICCS [58] algorithm the proposed method employs a separate image to constrain the iterative reconstruction. In contrast to PICCS however, not X_{comp} but the low-resolution reconstruction X_{lr} is employed as reference image in order to avoid the translation of possibly faulty time dependent information into single time frames. While details may be lost in X_{lr}, the intensity and location of major image structures is unchanged providing the basic aliasing-free image composition.
The reconstruction is obtained by solving the following constrained optimization problem:

$$\underset{X}{\operatorname{argmin}} \left[||\Phi(X) - Y||_2 + \lambda_{lr} \, \mathbf{R}_{lr} + \lambda_H \, \mathbf{R}_H \right] \tag{5.1}$$

$$\begin{aligned} \text{with} \qquad \mathbf{R}_{lr} &= ||\Psi(X - X_{lr})||_1 \\ \mathbf{R}_H &= ||H_{us} - H_{comp}||_2 \end{aligned}$$

The optimization is implemented again as a non-linear conjugate gradient approach based on the code introduced in reference [38] implemented in Matlab (Mathworks, Natick, US). Figure 5.4 depicts a comprehensive overview of the iterative histogram constrained reconstruction using the composition of consecutive k-spaces as reference.

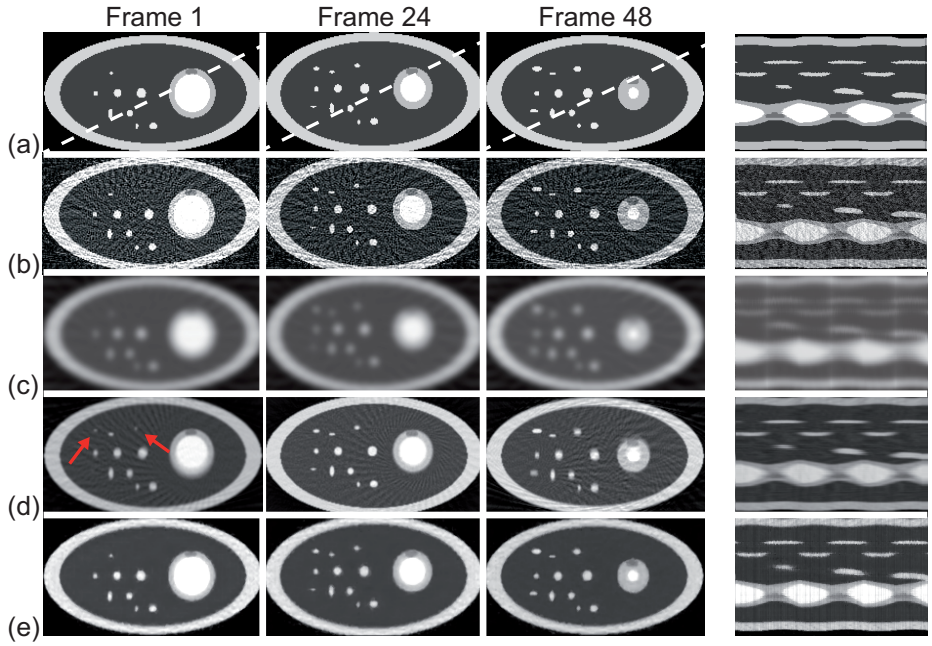

Figure 5.5: Representative results of the numerical dynamic MRI simulation. First three columns: Three different frames (1/24/48) out of the reconstructed set of 96 frames from the original phantom (a), the single frame undersampled (b), the low-resolution (c), the composite (d) and the RHiCA-LR reconstruction (e). Rightmost column: Respective temporal cuts along the direction marked in (a).

5.2.1 Numerical simulations

First the reference histogram constrained algorithm (RHiCA-LR) was assessed on the numerical phantom introduced in section 5.1 with a matrix size of 256^2. The simulation comprises respiratory and cardiac motion affecting all parts of the phantom and additional linear and random motion of blood vessels. The radius of three different simulated vessels (cf. arrows in Fig. 5.2(a)) was altered with respect to respiratory motion, causing the vessels to vanish in a certain number of frames and the occurrence of temporal averaging effects. A small pathology of unique intermediate intensity was added to the myocardium in order to assess the recovery of minor peaks in the histogram (cf. dashed circle in Fig. 5.2(a)). The dynamic evolution was sampled with a rate of 96 frames per heart cycle and 25 spokes ($R = 16$) per interleaved acquisition. Thus, 16 consecutive raw data sets combined represent a radially, fully sampled reference data set. The reconstruction was carried out with regularization parameters $\lambda_{lr} = 0.008$ and $\lambda_H = 0.01$. The proposed algorithm was applied on the basis of 16 image patches.
Figure 5.5 depicts representative results of the proposed reconstruction applied to the numerical phantom. Three time frames from diastole to systole are presented, comparing the original phantom (Fig. 5.5(a)) to the undersampled gridding reconstruction (Fig. 5.5(b)), the low-resolution reference (Fig. 5.5(c)), the composite reconstruction (Fig. 5.5(d)) and the RHiCA-LR iterative reconstruction (Fig. 5.5(e)). Temporal profiles, chosen as indicated in

Fig 5.5(a) are presented in the rightmost column. The results show that aliasing artifacts due to undersampling with a factor of $R = 16$ can be almost completely be corrected for using the reference histogram constrained reconstruction. Additionally, the simulation shows that the algorithm recovered both details in the image (vessels) and small peaks, hence details in the histogram (pathology). When focussing on frame 1 the results illustrate the major benefit when utilizing the histogram rather than the composite image itself as reference. Vessels reoccurring in the composite image due to temporal averaging (see arrows in Fig. 5.5(d)) are not translated into the reconstruction, since exclusively structures present in the initial image (Fig. 5.5(b)) get corrected for. The time dependent profiles show no sign of temporal averaging or blurring in direction of time. Respiratory and cardiac motion are both completely recovered.

5.2.2 *In vivo* experiments

The reconstruction of dynamic *in vivo* data was investigated on two time resolved functional cardiac MRI examination of healthy volunteers.
Data was acquired with a 3.0 T whole-body MR-scanner (Siemens Magnetom Trio, Siemens AG, Healthcare Sector, Erlangen, Germany) at the German Cancer Research Center (Heidelberg, Germany) using an untriggered 2D radial gradient echo sequence in breath-hold with a 12-channel body array and 24-channel spine coil. (Parameters of first acquisition: TR = 1.82 ms, TE = 1.12 ms, slice thickness = 5 mm, FOV: 450×450 mm^2, Resolution: 1.56×1.56 mm^2, flip angle = 10°, 15 frames per second, 5-fold interleaved, 30 spokes per time frame ($R = 13$); Parameters of second acquisition: TR = 2.02 ms, TE = 1.28 ms, slice thickness = 8 mm, FOV: 475×475 mm, Resolution: 1.86×1.86 mm^2, flip angle = 8°, 17 frames per second, 5-fold interleaved, 25 spokes per time frame ($R = 16$)). The algorithm was again applied on the basis of 16 image patches.
The first evaluation of an *in vivo* data set focuses on a visual comparison of reconstruction quality to a regularized iterative SENSE reconstruction, using the Matlab implementation included in Jeffrey Fessler's image reconstruction toolbox [152], which is based on a quadratic penalized weighted least square minimization via a preconditioned conjugate gradient algorithm. The RHiCA-LR reconstruction was carried out using regularization parameters $\lambda_{lr} = 0.01$ and $\lambda_H = 0.01$ determined by best visual appearance and a maximum MSSIM-value.
Figure 5.6 illustrates the results of artifact reduction using RHiCA-LR on a time resolved functional cardiac MRI. The displayed time frames (see Fig. 5.6(a)) were chosen at the beginning of the diastolic phase (frame 1), during the systolic phase (frame 10) and at the end of the systolic phase (frame 20). While the iSENSE reconstruction (second column) is impaired by blurring and residual artifacts, especially in the background, the RHiCA-LR reconstruction in the third column shows almost no remaining artifacts. Even strongly corrupted areas are recovered while small details such as pulmonary vessels are preserved (see enlarged area Fig. 5.6(a) - frame 20). Figure 5.6(b) and 5.6(c) present time dependent cuts along the marked dashed lines. In both cuts a strong suppression of undersampling artifacts as well as noise can be observed, while iSENSE depicts remaining artifacts and loss of image details due to blurring.

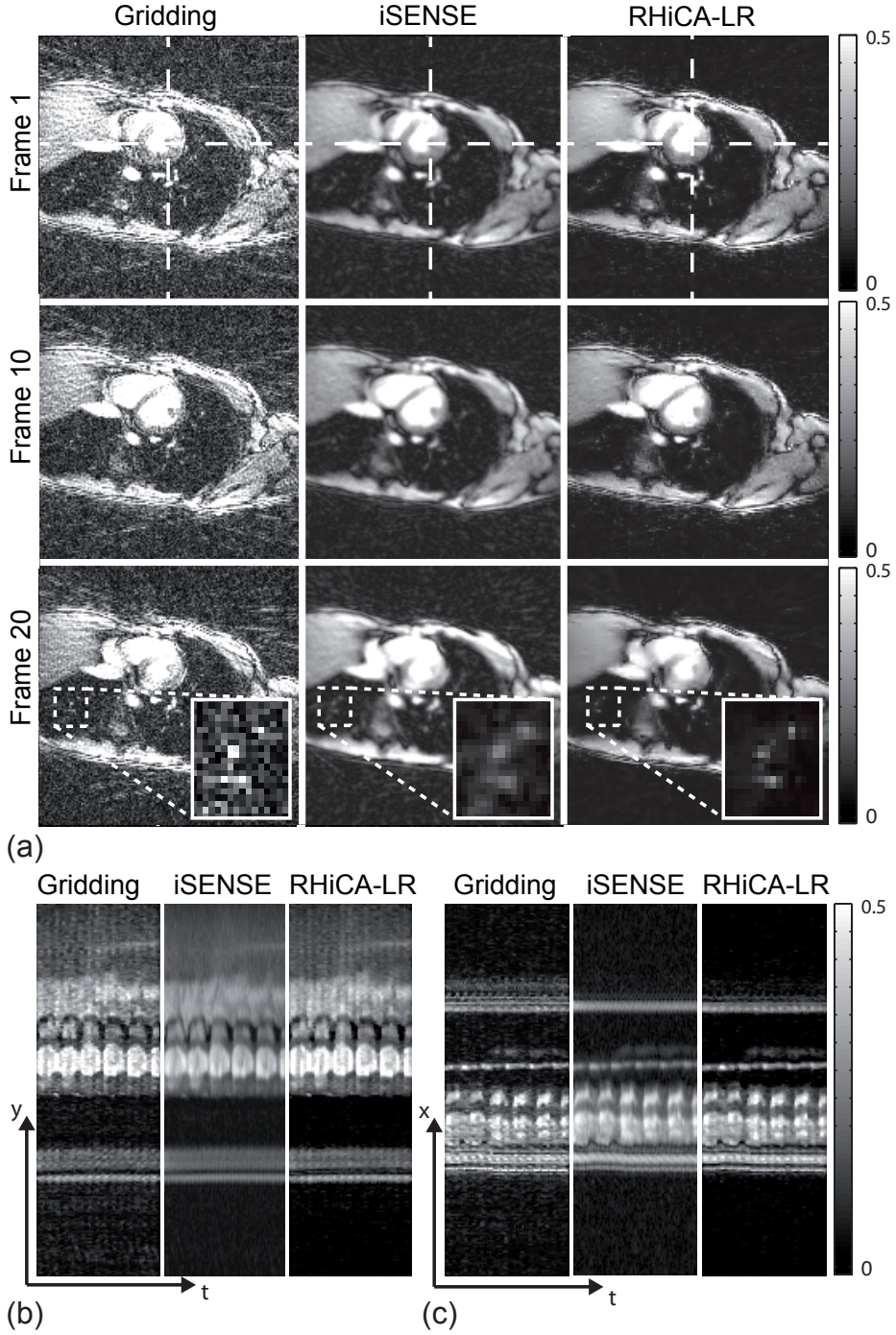

Figure 5.6: (a) Three different time frames within one single cardiac cycle are displayed. (Frame 1) Start of the diastolic phase. (Frame 10) During systolic phase. (Frame 20) End of systolic phase. The chosen section includes a short axis view of the heart, as well as a part of both liver and a large portion of the pulmonary parenchyma. The dashed lines mark the direction of cuts ((b) left-right, (c) anterior-posterior) through every single time frame.

In order to assess the limitations of the proposed approach the sampling density of the cardiac data set was decreased from $R = 3.0$ to $R = 28$ and subsequently reconstructed. The reconstruction is quantitatively evaluated using the MSSIM progress over iterations on data sets with a decreasing number of spokes. The MSSIM was calculated relative to the corresponding sliding window composite image and evaluated as a function of iterations. Regularization parameters were chosen according to the degree of undersampling ($R = 3.0$: $\lambda_{lr} = 0.002/\lambda_H = 0.005$; $R = 6.3$: $\lambda_{lr} = 0.005/\lambda_H = 0.008$; $R = 18$: $\lambda_{lr} = 0.008/\lambda_H = 0.01$; $R = 28$: $\lambda_{lr} = 0.01/\lambda_H = 0.02$).
The gridding reconstruction in the first column of Fig. 5.7(a) depicts increasingly severe aliasing artifacts up to an almost complete loss of image information in the 28-times undersampled reconstruction. The iSENSE reconstruction shows good results at small reduction factors. However, aliasing due to undersampling with a factor of $R = 18$ or higher can not be suppressed effectively. In turn, while evidently the result is not equal to the fully sampled reconstruction, heavy aliasing artifacts get almost completely suppressed in the RHiCA-LR reconstructions, whereas image information is preserved (see arrows). Temporal profiles along the indicated direction of the RHiCA-LR reconstruction (cf. Fig. 5.7(a)) show an increase in temporal resolution and a very effective suppression on aliasing artifacts. The MSSIM-values in Fig. 5.7(b) demonstrate an overall improvement when using RHiCA-LR instead of iSENSE and faster convergence in all used reduction factors.

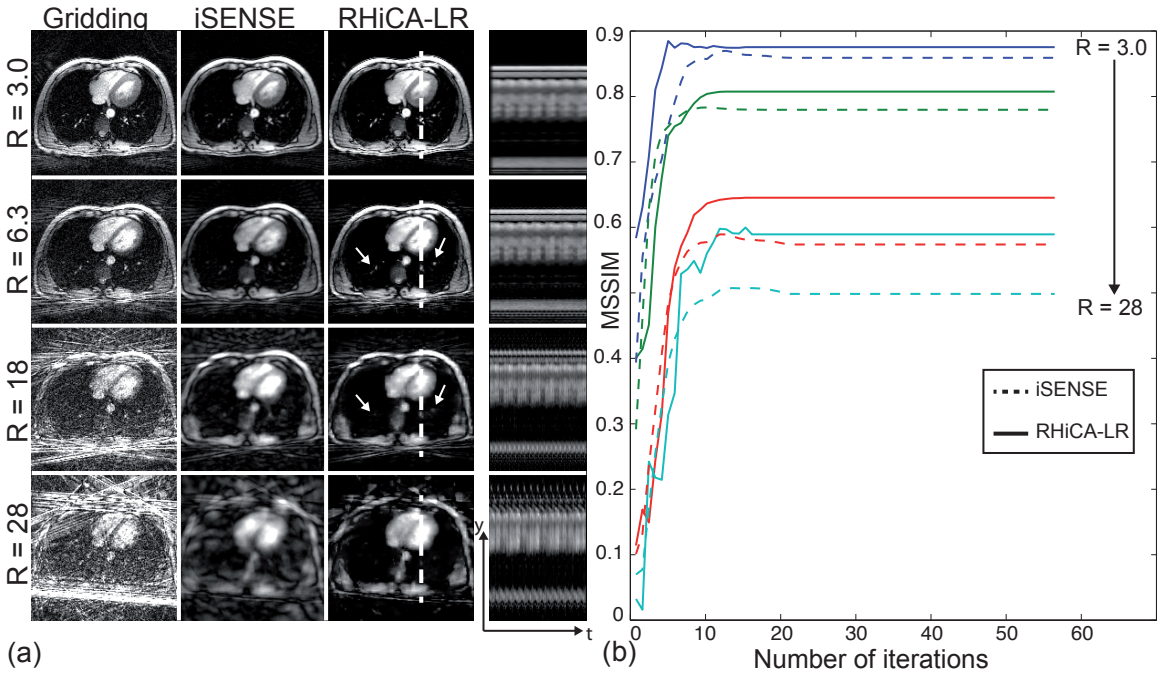

Figure 5.7: (a) Comparison of reconstructions of increasing reduction factor: Initial gridding reconstruction (column 1), regularized iterative SENSE reconstruction (column 2), results using RHiCA-LR (column 3) including temporal y-t cuts (column 4) along the lines indicated in the RHiCA-LR reconstruction. (b) MSSIM characteristics versus iterations for all performed reconstructions.

5.3 Summary

This chapter demonstrated the possibility to compute a low-entropy reference histogram H_{comp} from the composite image within a temporally resolved MRI measurement. PSF evaluations and the assessment of undersampled reconstructions could prove that both the entropy and the histogram of composite reconstructions very closely resemble the fully sampled case even at high acceleration factors. Subsequently, the feasibility of employing H_{comp} as a histogram space constraint together with an image space regularization utilizing the low-resolution reconstruction X_{lr} was assessed on numerical simulations as well as *in vivo* data.

The first assessment comprised a numerical thorax phantom, simulating a functional cardiac MRI in free-breathing. Extensive motion in the time-resolved data resulted in an enhanced distortion of the composite image. The reference histogram H_{comp} however was successfully used to suppress aliasing artifacts and recover details at an acceleration factor of 16. Aside from minor residual artifacts in the ventricle the introduced algorithm managed to suppress aliasing completely without any loss in temporal or spatial resolution.

The reconstruction of two native dynamic cardiac acquisitions demonstrated the feasibility of the introduced algorithm even when confronted with moving small image details such as the pulmonary vessels and heavily moving areas as the myocardium. The resulting images showed almost no residual artifacts while maintaining details and contrast properties. The time dependent cuts through the data set demonstrated no temporal averaging, hence the full temporal resolution was available after reconstruction using RHiCA-LR.

The comparison to a standard iterative SENSE reconstruction demonstrated the superior ability of noise and artifact suppression when using composite histogram regularization.

6 Further Evaluations

6.1 Influence of algorithm parameters

The following chapter is intended to provide deeper insight regarding different parameters within the RHiCA algorithm. First the MSSIM dependency on the number of bins per histogram (see Subsection 6.1.1) and on the number of image patches (see Subsection 6.1.2) is evaluated on the reconstruction of an undersampled Shepp-Logan phantom. Since both parameters affect the reconstruction duration it is crucial to find the optimal balance of image quality and number of bins/image patches. Furthermore, as introduced in section 3.2 theoretically there is no limit on the number of constrains included in the cost function. Whether it is beneficial to employ a multitude of constraints and which weighting should be used is evaluated on a specially designed phantom (cf. Subsection 6.1.3). In order to find the optimal combination of constraints for a pure RHiCA reconstruction, the three introduced regularization functions R_H, R_{TV} and R_{WL} are applied with varying weightings lambda. Similarly, both regularizations within the RHiCA-LR algorithm are varied separately in a different evaluation. The resulting reconstructions are evaluated on the basis of the MSSIM index in order to find the maximum image quality.

6.1.1 Influence of bin size

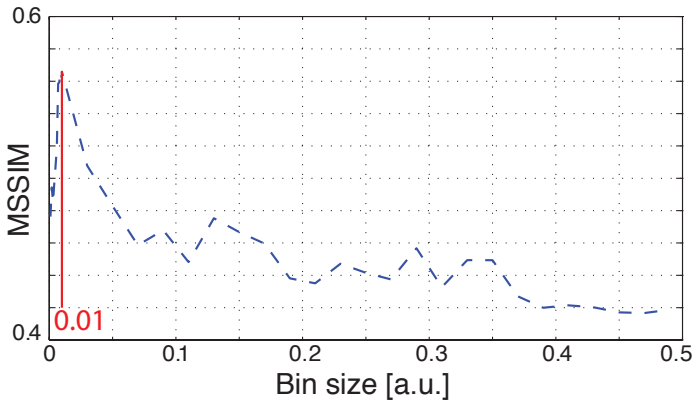

Figure 6.1: MSSIM-value as a function of the bin size used to compute the histogram. The MSSIM has a distinct maximum at a bin-size of 0.01 for data normalized to 1.

The first step and basis of the histogram-based correction is the computed of the intensity histogram of the involved images. The parameter that decides upon how coarse or fine

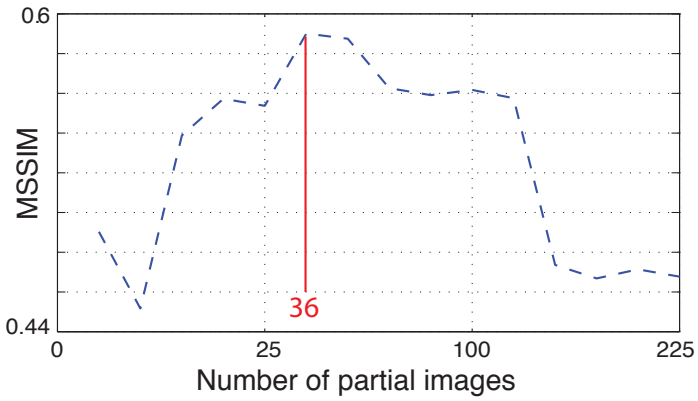

Figure 6.2: MSSIM-value as a function of the number of image patches used to compute the histogram. The MSSIM has a distinct maximum at 36 image patches.

the histogram is sampled is called the bin-size, hence the intensity interval comprising pixels counted in the same bin. When choosing the bin-size it is crucial to find a balanced representation. Very small bins can result in a histogram with a large number of small peaks, comparable to noise corrupting a smooth curve. A large bin size on the other hand can cause separated intensity peaks to overlap or merge and hence reduce the information contained in the histogram. While a bin size too small is likely to cause the reconstruction to present with noise-like artifacts, a coarse sampling results in the loss of single intensities in the image representation.
In order to find the optimal bin-size the MSSIM index of a reconstructed undersampled Shepp-Logan phantom (matrix: 256^2) is evaluated with varying bin size of the histogram. The phantom was normalized prior to sampling and the number of bins was varied between 2 and 1000. Figure 6.1 presents the MSSIM values of the final reconstruction as a function of the bin-sizes. The results clearly show a maximum quality of the reconstruction at a bin-size of 0.01, corresponding to a number of 100 bins. Histograms using intensity intervals of 0.01 present with the optimal combination of smoothness to avoid false peaks and accuracy for the detection of small peaks.

6.1.2 Influence of the number of image patches

As introduced in Subsection 3.2.4 the histogram entropy based iterative reconstruction algorithm was implemented as a patched approach. That is, in order for the method to detect intensities with only a small number of pixels in the image, the total image matrix is rastered prior to the reconstruction. Subsequently, the histogram gradient is calculated only from the single raster parts, so image patches. Due to the limited extent of the histogram gradient over intensities, the correction calculated from the partial image can be applied to the whole image merely adjusting intensities also contained in the initial partial image. This procedure is performed for each raster position.
For this strategy to be successful it is important to choose the optimal grid size, hence the

number of partial images, the original is separated in. Evidently, a grid size equal to the number of pixels would hinder the introduced algorithm from working and a grid size of 1 corresponds to the basic form of the correction. In order to find the optimal number the algorithm was applied to an undersampled Shepp-Logan phantom (256^2) with an increasing number of partial images from 1 to 225.
In the case of the Shepp-Logan phantom with a matrix size of 256^2 the simulation shows a clear maximum at a number of 36 partial images, each with a number of $43^2 = 1849$ pixels. However, while the maximal MSSIM suggests to use a grid of size 36, the computational time is an issue which has to be taken into considerations when selecting the number of patches. If the number of iterations is assumed constant for each image patch application, the computational time increases by a factor of 36. Taking this fact into account the reconstructions demonstrated in this work were performed using a grid size of 16, which yields the second highest MSSIM among the reconstructions with a smaller grid size then 36. The trade off in MSSIM is easily countervailed by the saving of reconstruction time.

6.1.3 Optimal weighting for RHiCA

As aforementioned the numerical Shepp-Logan phantom can be used as an objective simulation in many cases, however the presence of merely piece-wise smooth areas unrealistically favors a hard total variation constraint. Hence, in order to also include structures such as vessels and other small object the phantom depicted in Fig. 6.3 was designed. The numerical phantom comprises areas of constant intensity of different magnitude and small structures in the bottom section. The star-shaped details in the phantom were designed in the style of known spatial resolution phantoms, such as the Siemens star. The hypo-intense lines with a width of only one pixel give insight to which degree single narrow objects can be recovered from undersampled data. Additionally, the decreasing distance between the line profiles demonstrate to which degree the true resolution of the image can be recovered. The measurement was again simulated as a 8-fold multi-coil acquisition of the 256^2 matrix with complex Gaussian noise ($\sigma = 0.02$), radially sampled with a reduction factor of 13.
In order to measure the quality of the reconstruction the MSSIM index, as introduced in Subsection 3.2.5 was employed, comparing the reconstruction result with the original phantom. The basic image characteristics of the respective constraints $R_{H/TV/WL}$ can be observed best, when applying a heavy weighting of typically $\lambda = 0.1$. Figure 6.3 presents the results of the iterative reconstruction, applying the three regularizations separately. The reconstruction in Fig. 6.3(a) demonstrates the features associated with a hard Total Variation constraint. While smooth image areas are recovered almost artifact free, which explains the high MSSIM value of 0.6, fine structures and intensity steps appear blurry and washed out in the reconstruction. This effect is clearly visible in the line profile in the bottom row of Fig. 6.3. The red profile depicts a complete suppression of noise and undersampling artifacts, however the single peaks in the original profile are not recovered properly. The histogram constrained reconstruction in Fig. 6.3(b) depicts complementary features when compared to Fig. 6.3(a). Artifacts in smooth areas are not as effectively suppressed as with the TV constraints, however the overall image appearance is less blurry and small details are recovered correctly. Especially the line profile demonstrates how well RHiCA preserves

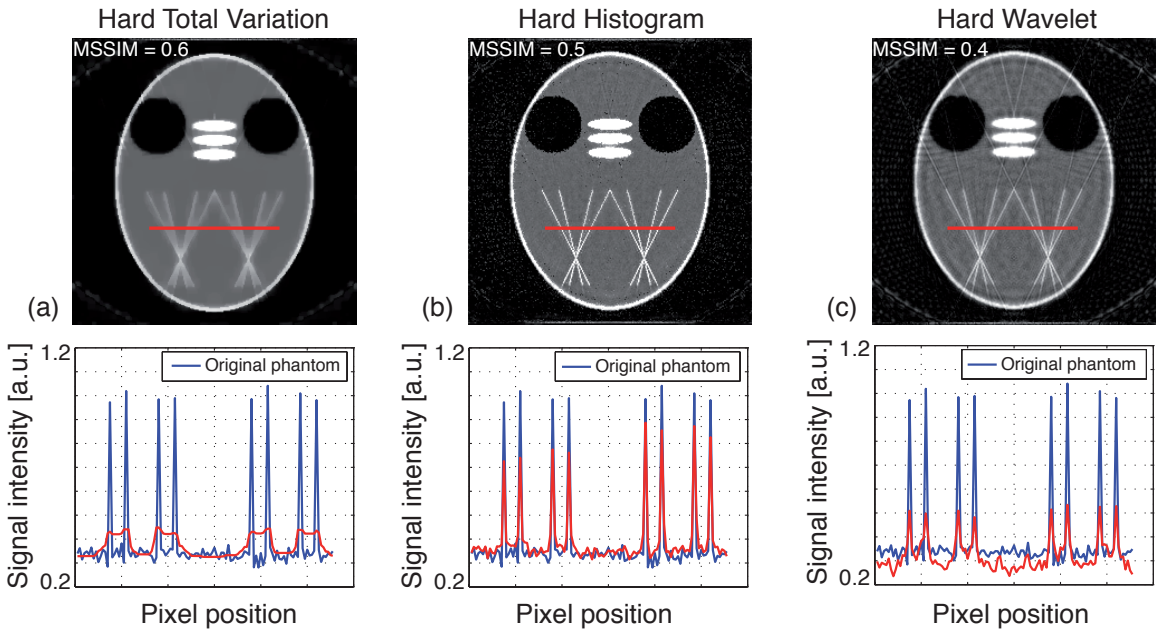

Figure 6.3: Reconstruction from undersampled data using only one constraint, each weighted with $\lambda = 0.1$. (a) Total Variation reconstruction, resulting in a very smooth image, however with poor spatial resolution and an MSSIM index of 0.6. (b) Histogram entropy constrained reconstruction with very good recovery of spatial resolution, however still corrupted by residual image noise and with an MSSIM index of 0.5. (c) Wavelet sparsity seems not to have great success as prior knowledge. The reconstruction is corrupted by noise and the original intensities are not properly recovered resulting in an MSSIM of only 0.4.

resolution, intensity and position of the star-shaped lines within the phantom, resulting in a MSSIM value of 0.5. The least effective artifact suppression is achieved by the Wavelet constrained iterative reconstruction. Both the reconstruction and the profiles show neither an effective artifacts suppression, nor recovery of details, suggesting that, in the case of this phantom Wavelet sparsity is not a favorable choice of prior knowledge.
The results from this first basic evaluation again suggest that a combination of constraints might be beneficial for the reconstruction. In order to find the optimal combination of regularization weightings, the iterative reconstruction was successively applied with varying weightings $\lambda_{WL/TV/H}$. In a first evaluation the three constraints were applied separately with different lambdas ($\lambda = 0, 1 \cdot 10^{-4} \cdots, 1 \cdot 10^{-1}$) and the MSSIM was calculated for each iteration step. Figures 6.4(a-c) present plots of the MSSIM versus the number of iterations. The graphs demonstrate for all three cases, that the iterative reconstruction converges if the weighting is chosen within limits.
Figure 6.4(a) presents the quality assessment for varying weightings of the Wavelet sparsity regularization. The Wavelet regularization results in almost the same MSSIM (MSSIM$\approx$ 0.48) value in three of the chosen values for λ_{WL}, whereas the heaviest regularization with

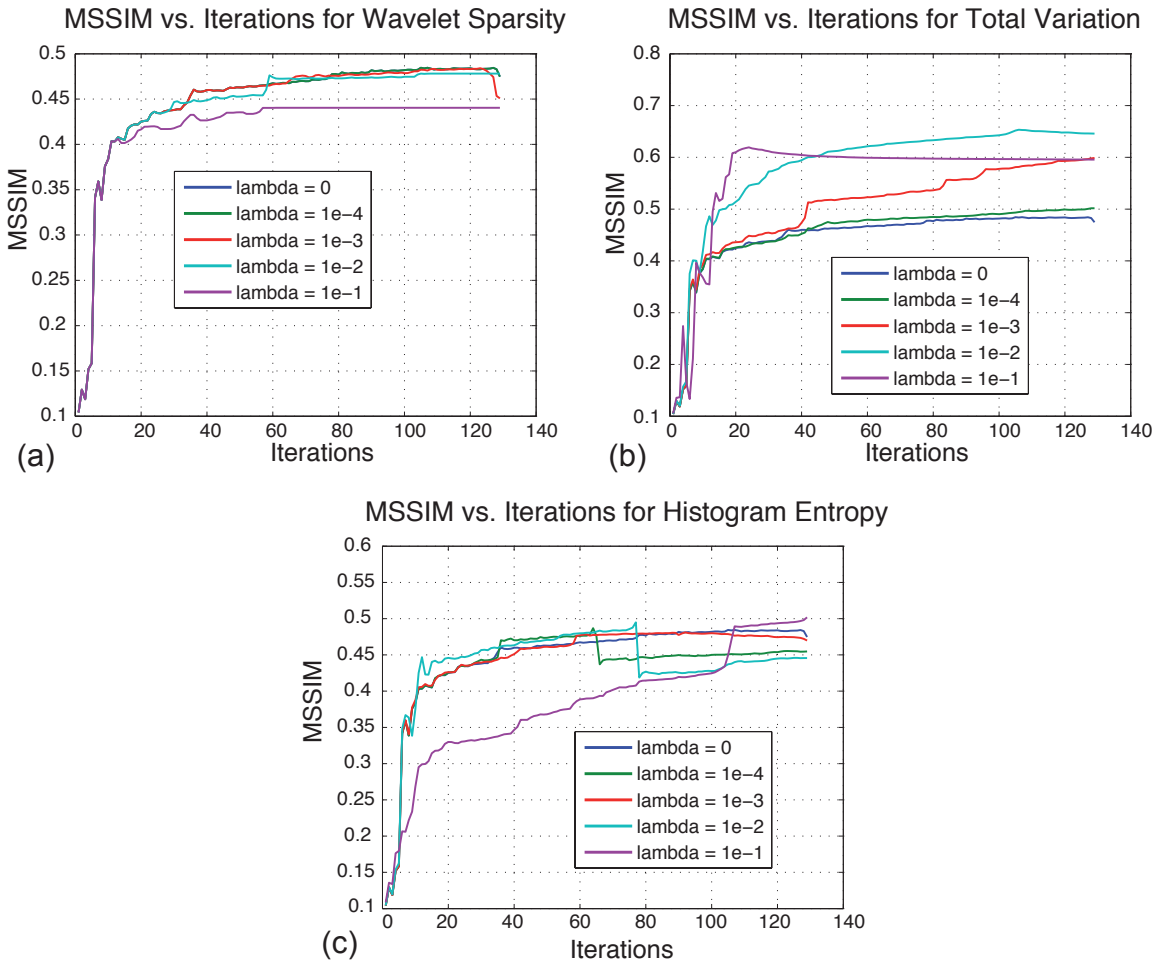

Figure 6.4: MSSIM versus the number of iteration for each constraint using different λ-values from 0 to 0.1. Almost all plots show an increase in the MSSIM with the number of iterations. Exceptions can be ascribed to an overly constrained situation (see (a) at $\lambda = 0.1$ and (b) at $\lambda = 0.1$) and the rastered version of the histogram entropy constrained reconstruction (c). The simulations yield a maximum MSSIM at λ-values of $\lambda_{WL} = 1 \cdot 10^{-4}$, $\lambda_{TV} = 1 \cdot 10^{-2}$ and $\lambda_H = 0.1$

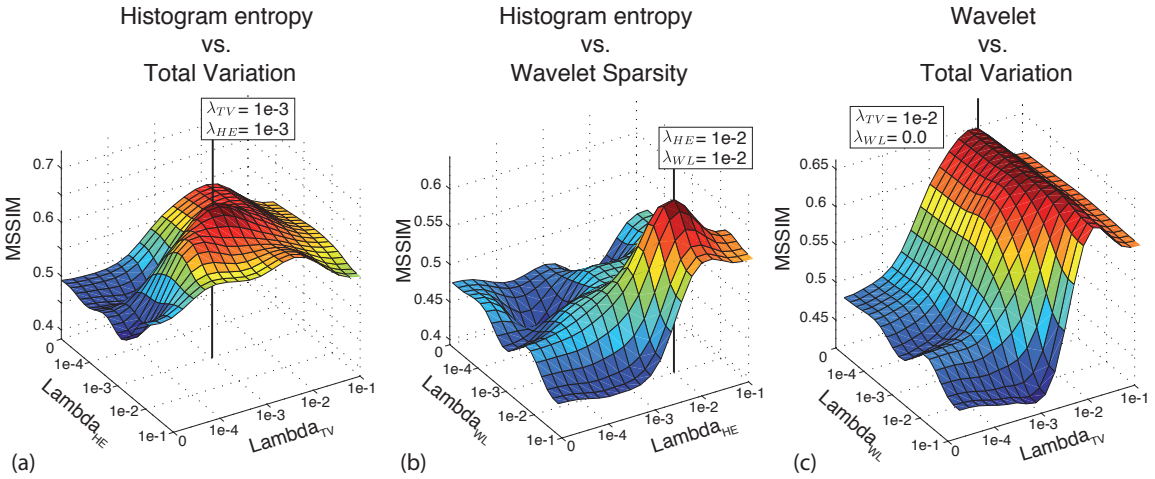

Figure 6.5: Simultaneous variation of λ-values in the constrained RHiCA reconstructions. (a) Regularization with R_{TV} and R_H: The maximum MSSIM is achieved when using $\lambda_{TV} = \lambda_H = 1 \cdot 10^{-3}$. (b) Regularization with R_{WL} and R_H: The maximum MSSIM is achieved when using $\lambda_{TV} = \lambda_H = 1 \cdot 10^{-2}$. (c) When combining R_{TV} and R_{WL} the Wavelet sparsity constraint has only minor impact on the reconstruction. The maximum MSSIM is achieved at $\lambda_{TV} = 1 \cdot 10^{-2}$ and $\lambda_H = 0$.

$\lambda = 0.1$ results in a reconstruction of lower quality. Constraining the iterative reconstruction too heavily can, as in this case, cause the optimization to hit a local minimum, preventing the reconstruction to further improve, as apparent from iteration step 57 onward. The MSSIM values of the R_{TV} regularized reconstructions are depicted in Fig. 6.4(b). The final MSSIM values after 130 iterations increases with λ_{TV} up to $\lambda_{TV} = 0.01$. Similar to the Wavelet regularization constraining with $\lambda_{TV} = 0.1$ prevents the reconstruction to further improve and in contrary causes the image quality to decrease. Hence, with a maximum MSSIM of 0.64 a Total Variation constraint of $\lambda_{TV} = 1 \cdot 10^{-2}$ results in the reconstruction of best perceivable quality. The maximum final MSSIM value of 0.5 for the R_H constrained reconstruction is achieved using $\lambda_H = 0.1$ (see. Fig. 6.4(c)). The MSSIM evolution over iterations in the case of the histogram constraint present a different characteristics when compared to Wavelet or Total Variation. Occurring steps in the MSSIM values can be ascribed to the patched application introduced in Subsection 3.2.4. While the gridded version of the algorithm increases the chance of detecting details in the image, it can also result in local minima as apparent for $\lambda_H = 1 \cdot 10^{-4}$ and $\lambda_H = 1 \cdot 10^{-2}$.
The result of combining regularizations in terms of MSSIM is evaluated in Fig. 6.5. The surface plots describe the evaluation of the MSSIM after 130 iterations depending on the chosen λ of two respective constraints. Figure 6.5(a) presents the simultaneous application of TV and histogram entropy with a maximum MSSIM of 0.7 at $\lambda_{TV} = \lambda_H = 1 \cdot 10^{-3}$. Constraining with both R_H and R_{WL} results in a distinct MSSIM maximum of 0.6 at $\lambda_{TV} = \lambda_H = 1 \cdot 10^{-2}$. The simultaneous application of R_{TV} and R_{WL} as commonly used

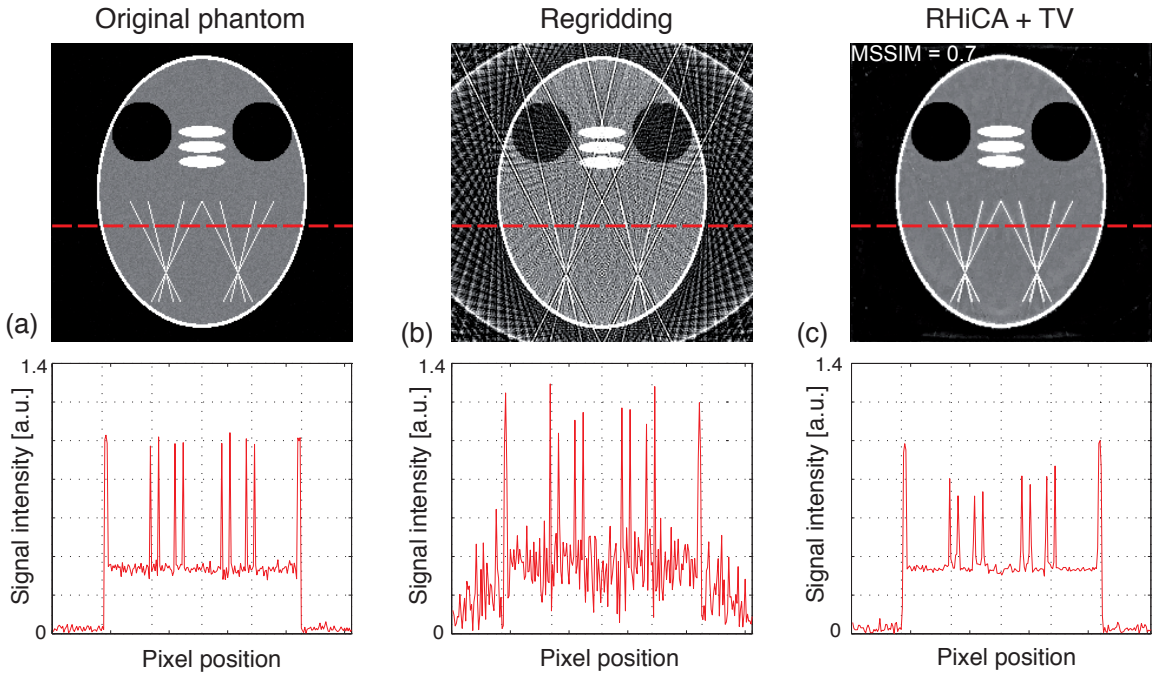

Figure 6.6: (a) Originally designed phantom with complex Gaussian noise. (b) Gridding reconstruction from a 13-fold undersampled data set. (c) Final reconstruction using a hybrid regularization with R_H and R_{TV} and weightings $\lambda_H = 1 \cdot 10^{-3}, \lambda_{TV} = 1 \cdot 10^{-3}$.

in compressed sensing applications again shows that the Wavelet sparsity constraint does not improve the reconstruction quality on this object and results in a reconstruction with a MSSIM value of 0.65 at $\lambda_{TV} = 1 \cdot 10^{-2}$ and $\lambda_{WL} = 0$. The global maximum of the 3-dimensional parameter space of the R_H, R_{TV}, R_{WL}-variation yields a constraint combination $\lambda_H = 1 \cdot 10^{-3}, \lambda_{TV} = 1 \cdot 10^{-3}, \lambda_{WL} = 0$, hence the result depicted in Fig. 6.5(a).
Figure 6.6 presents the final reconstruction using the assessed optimal weighting combination. Fig. 6.6(a) depicts the original noisy phantom of matrix size 256^2 which was sampled using 31 spokes. The line profile in the bottom row shows a cut through the star-shape lines within the phantom with the introduced random noise. The regridded reconstruction in Fig. 6.6(b) is corrupted by heavy streaking artifacts throughout the whole image. Especially the line structure cause heavy aliasing presenting as elongation of the original structure. The result of the constrained iterative reconstruction depicted in Fig. 6.6(c) shows an almost complete suppression of undersampling artifacts and noise, while recovering both width and intensity of the hypo-intense line structures. Smoothness and the MSSIM are comparable to the optimal TV reconstruction, whereas the detail fidelity and resolution is equal to the reconstruction solely using R_H as regularization, demonstrating the complementary character of both constraints. Consequently, it can be concluded when acquiring images from objects similar to the appearance of the designed phantom the combination of R_H and R_{TV} results in the reconstruction of highest perceivable quality.

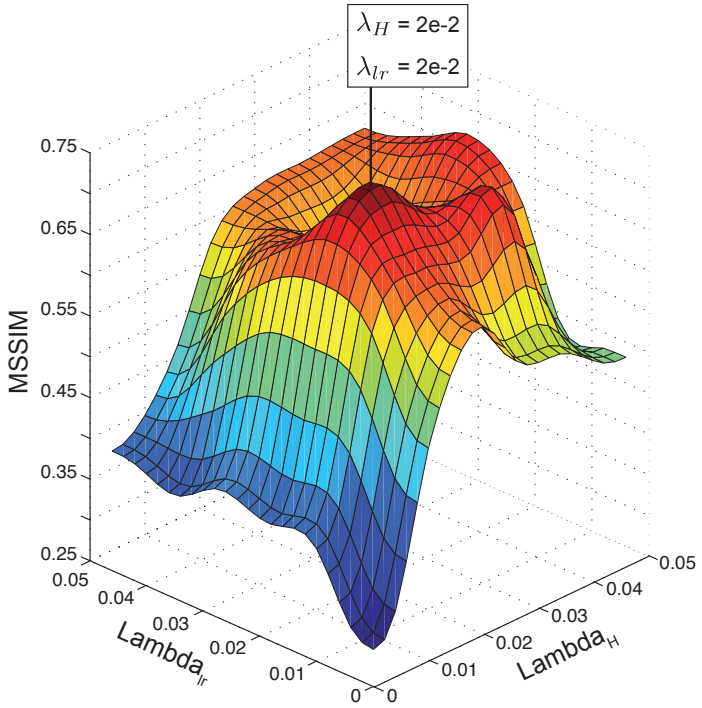

Figure 6.7: Simultaneous variation of λ-values in RHiCA-LR. A maximum MSSIM-value of 0.74 is achieved at $\lambda_H = \lambda_{lr} = 2 \cdot 10^{-2}$.

6.1.4 Optimal weighting for RHiCA-LR

Equivalent to the assessment of regularization parameters of RHiCA, also the influence of parameters within the RHiCA-LR algorithm was evaluated. On the basis of the numerical functional cardiac MRI simulation, introduced in Chapter 5, one 16-fold undersampled frame was reconstructed using RHiCA-LR with variable λ_{lr} and λ_H. The regularization parameters were chosen in an interval from 0 to 0.05. The result of the iterative reconstruction was compared to the original phantom on the basis of the structural similarity value. Figure 6.7 depicts the MSSIM value as a function of λ_{lr} and λ_H.
While the R_{lr}-constraint by itself improves the image quality only to a small degree, in combination with R_H a clear increase in the MSSIM was achieved with a maximum value of 0.74 at $\lambda_H = 2 \cdot 10^{-2}$ and $\lambda_{lr} = 2 \cdot 10^{-2}$.

6.1.5 Summary

Within this chapter the best settings for the basic parameters of the iterative reconstruction were evaluated. The quality and computational time of the reference histogram based method is primarily determined by the number bins per computed histogram and the number of used partial images the original image is separated into. In order to optimize both parameters a reconstruction solely constrained by the histogram regularization was simulated on an undersampled normalized Shepp-Logan phantom with varying bin size and

number of partial images. The simulation resulted in a distinct maximum in the MSSIM index at a bin size of 0.01 corresponding to 100 equally spaced bins for each histogram. The assessment of the influence of the chosen number of image patches yielded a MSSIM maximum value at a number of 36 partial images. However, when taking the overall computational time into account a smaller number of partial images is favourable. Hence, a grid size of 16 with the second highest MSSIM index of grid sizes lower than 36 was employed as a balance between reconstruction duration and quality.
Since the iterative reconstruction can be equipped with a multitude of regularizers R the second part of this chapter concentrated on the evaluation of the best combination of constraints and corresponding weightings. For this purpose a phantom was designed, comprising both piecewise smooth areas and small structures. In order to be able to assess the real spatial resolution of the reconstruction the mentioned small structures were arranged similar to the known Siemens star resolution phantom.
The application of the three constraints separately resulted in the highest MSSIM (0.6) for the Total Variation constrained reconstruction. The resolution and detail fidelity, however, was clearly superior in the reference histogram constrained result (MSSIM = 0.5), while regularizing with Wavelet sparsity showed to be of minor success in case of this phantom. The MSSIM evaluation of different weightings on the separately applied constraints over iterations demonstrated the feasibility of all three approaches, since most characteristics showed convergence. Additionally, the assessment proves the importance of choosing the correct weighting for the respective regularization. Effects such as a declining MSSIM are signs for an overly constrained optimization.
The analysis resulted in an optimal weighting combination of $\lambda_{TV} = 1 \cdot 10^{-3}$ and $\lambda_H = 1 \cdot 10^{-3}$, hence a regularization with both the reference histogram and the TV constraint. The MSSIM of the final reconstruction yielded a value of 0.7. Additionally, the visual inspection of the reconstruction and especially a pixel profile through the star-shaped image details demonstrated superior smoothness and simultaneous detail fidelity, confirming the expected complementary character of the two regularizations.
The optimization of both regularization parameters employed in the RHiCA-LR framework resulted in a distinct maximum MSSIM at $\lambda_H = 2 \cdot 10^{-2}$ and $\lambda_{lr} = 2 \cdot 10^{-2}$. While this result still is dependent of the underlying object, it still shows that the reconstruction benefits from both regularizations.

6.2 Performance assessment

Since the introduced reconstruction algorithm is based on artifact detection in histogram space yielding a correction in the image domain, it is confronted with limitations in both domains. On the one hand the question arises to which degree images with a small contrast to noise ratio can be reconstructed (see Subsection 6.2.1), which simultaneously corresponds to the separations of the according intensity peaks in histogram space. On the other hand the sensitivity of the algorithm to image details of unique intensity is of great interest, corresponding to a variation of peak height in the histogram domain (see Subsection 6.2.2). In order to approach these limits the algorithm was applied to two specially constructed phantoms, varying the according parameter.

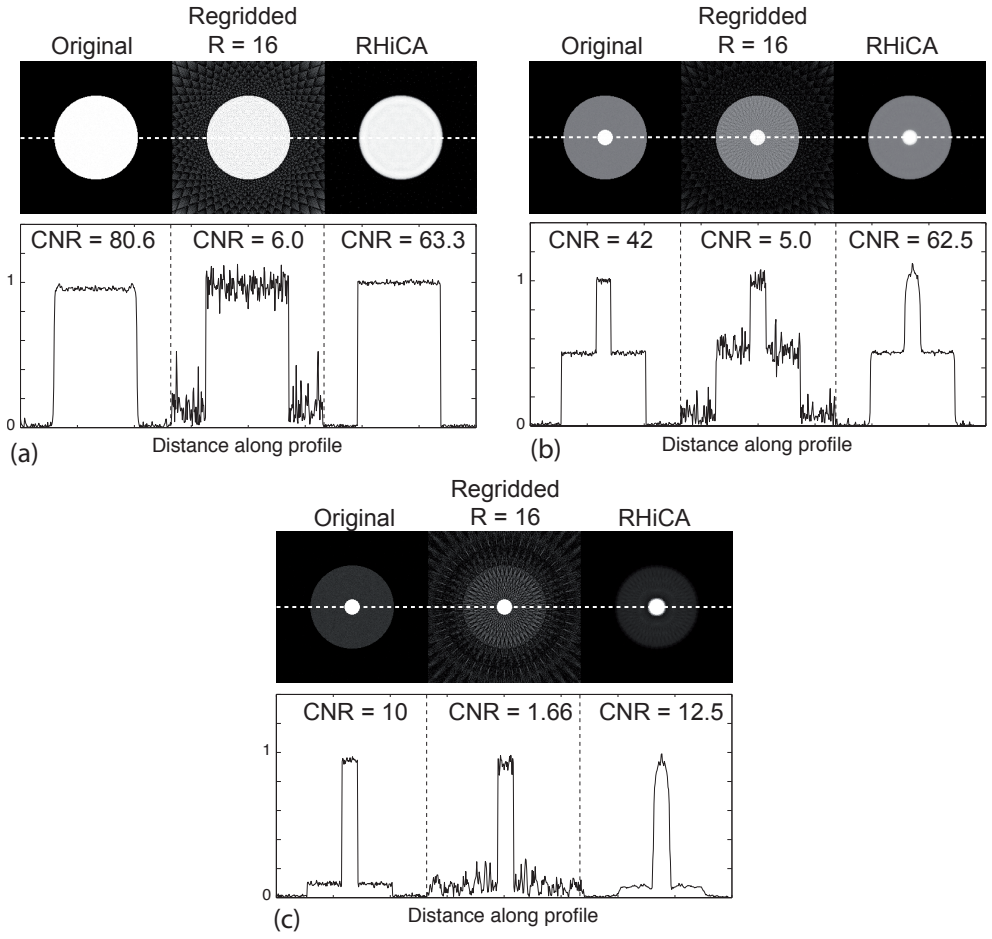

Figure 6.8: Performance evaluation with decreasing contrast to noise ratio (CNR) on a phantom with gradually reduced intensity. The central peak was added in order to ensure constant magnitude of artifacts and for reasons of normalization.

6.2.1 Contrast to noise dependency

Since the basis of the introduced algorithm is the image histogram, the feasibility of the algorithm largely depends upon the peak separation in histogram domain. That is, in case different regions of the image show only low contrast, the reconstruction is challenging even if the object only comprises few different intensities. In image representation, the reconstruction task might then seem simple, however, separating neighboring intensity peaks in histogram domain might be challenging. In order to assess this matter, a phantom was designed comprising 3 different intensities (see. Fig. 6.8), namely $I_1 = 0$, $I_2 = 0, 0.1, \cdots, 1$ and $I_3 = 1$. The crucial intensity difference is defined as the step from the zero valued background and the designed ring of varying intensity. Since the number of pixels for both intensities is almost equal, the success of the reconstructions solely depends upon the distance of the intensity peaks. The centred circular structure was introduced to the phantom to ensure undersampling artifacts as independent from the main intensities as possible and to simplify the normalization of the image. The intensity separation was gradually decreased from 1 (Fig. 6.8(a)), over 0.5 (Fig. 6.8(b)) to 0.1 (Fig. 6.8(c)), corresponding to contrast to noise (CNR) values in case of the regridded reconstruction of 6.0, 5.0 and 1.66. The reconstructions in all CNR cases proof to recover the intermediate intensity with only minor residual artifacts. The CNR of the RHiCA reconstruction leads to a CNR improvement to a value comparable or even better to the noise corrupted original. The line profile within the result at the lowest CNR of 1.66 shows minor blurring at the edges of the inner circle. However, when taking the severity of artifacts into account the reconstruction and

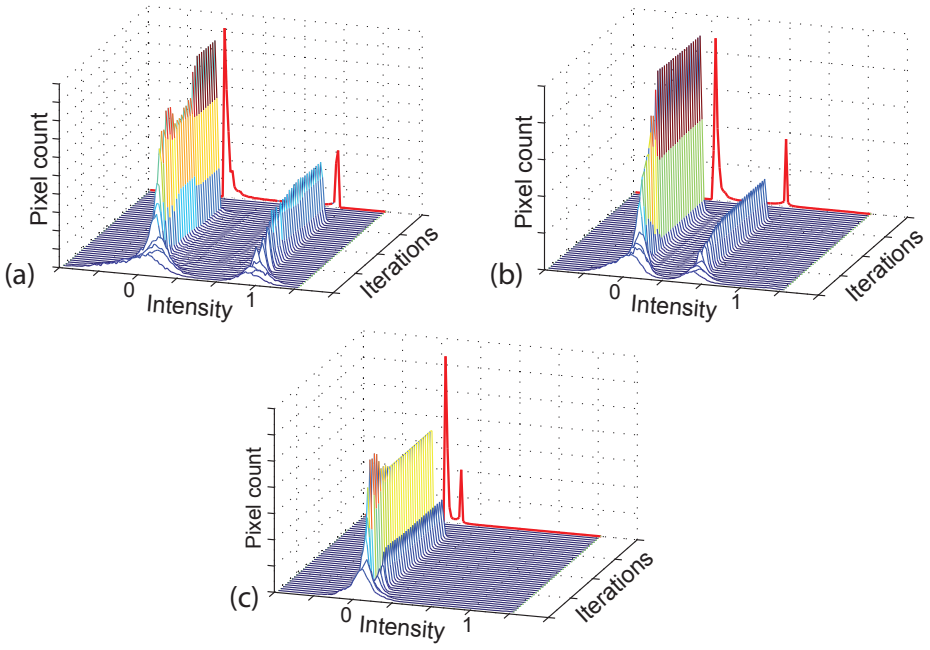

Figure 6.9: Histogram evaluation over iterations during the reconstruction of the three CNR cases in Fig. 6.8. (a) CNR = 6.0 (b) CNR = 5.0 (c) CNR = 1.66. A separation and narrowing of the displayed peaks was achieved in all three cases.

its CNR pose a successful recovery.
Figure 6.9 demonstrates the histogram evolution over iterations for the mentioned cases depicted in Fig. 6.8. The initial histograms in Figs. 6.9(a/b) are heavily broadened, however still separated. Over the iteration steps the algorithm succeeds in reversing the spreading of the peaks almost perfectly resembling the fully sampled histogram (red). Evidently from the initial histogram in Fig. 6.9(c) the peaks originally separated only by 0.1, completely overlap forming one single peak. Nevertheless, the algorithm manages to separate the original peaks. While the peaks are at the original position, hence the intensities in the image are reconstructed correctly, the height of the peaks is not exactly according to the fully sampled reconstruction, which manifesting as residual artifacts in the image.

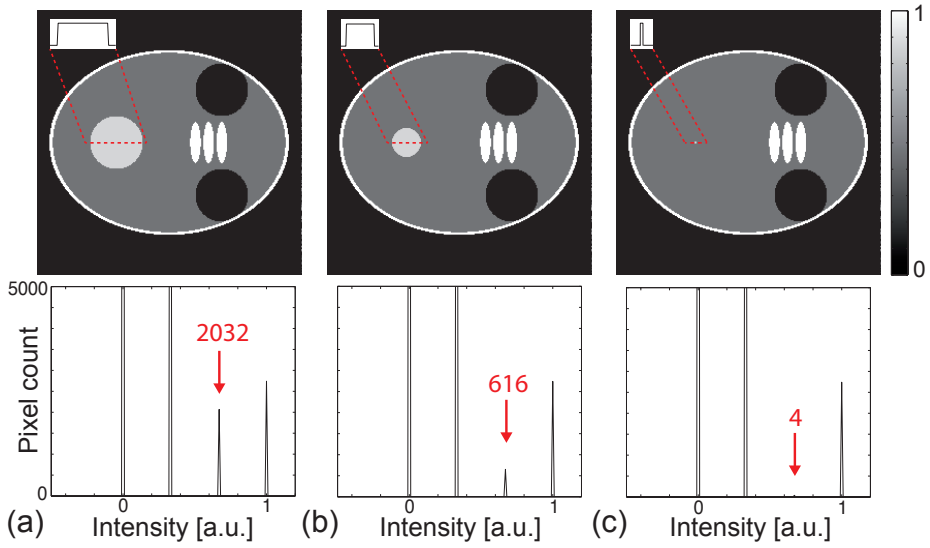

Figure 6.10: Phantom constructed for the sensitivity evaluation of the histogram constrained reconstruction. A circular structure of intermediate intensity and decreasing diameter was set on the left side of the phantom. The pixel count of the structure is gradually reduced from (a) 2032 pixels over (b) 616 pixels to only 4 pixels (c).

6.2.2 Sensitivity evaluation

One major concern that comes to mind regarding the histogram entropy regularization is the question of sensitivity, that is, can image details be successfully recovered. Here one has to differ two cases. If the detail in the image, for instance a small vessel, is part of a bigger pixel intensity pool, the corresponding pixel intensity is comprised in an easily detectable peak in the intensity histogram. In these cases the structure subject to reconstruction is merely a detail in image space, but not in the underlying histogram space and hence does not pose an increased challenge for the reconstruction. However, if the detail is not part of a bigger intensity species, it corresponds also too a small peak in the intensity histogram, which poses the risk of an inefficient correction.

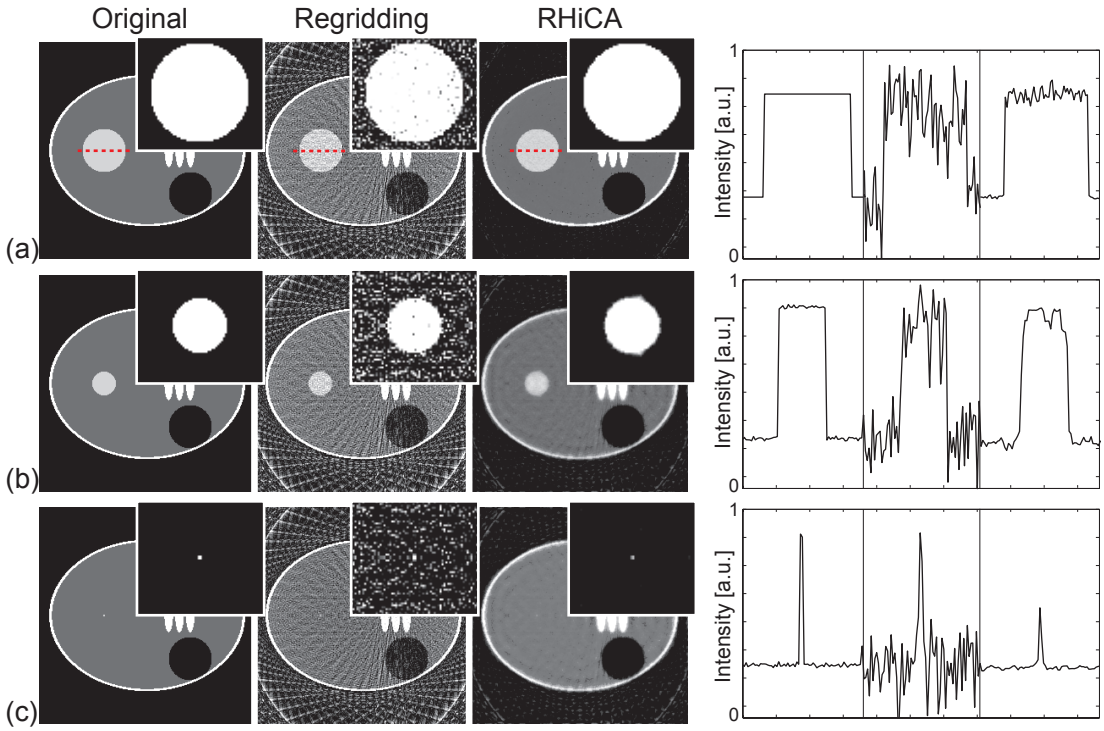

Figure 6.11: Exemplary results from the sensitivity evaluation corresponding to the cases depicted in Fig. 6.10. The position of the line profiles in the right column is indicated in (a). The enlarged cut-outs are scaled for best visual appearance.

The sensitivity of the histogram entropy based regularization was evaluated on the phantom depicted in the first row of Fig. 6.10. The object of matrix size 256^2 comprises, similar to the Shepp-Logan phantom ellipses of different radius and intensity, normalized to 1 and added complexed valued Gaussian noise of with $\sigma = 0.02$. The radius of one circle of intermediate intensity of approximately 0.65 was gradually decreased from a number of 2032 to only 4 pixels. In percentage of the total pixel count this complies with a decrease from 3% to 0.006%. The second row of Fig. 6.10 depicts the histogram for three exemplary cases of varying radii.
Figure 6.11 presents the reconstruction results solely based on the histogram entropy regularization for the three cases depicted in Fig. 6.10. While the enlarged area still shows residual artifacts, the detail was recovered in all cases. Figures 6.11(a/b) demonstrate that width and intensity of the reconstructed object comply with the original, although the gridded reconstruction suffers from heavy artifacts. In case of a pixel count of only 4 in Fig. 6.11(c) the detail is still visible in the reconstruction, however, the peak encountered loss in intensity. Nevertheless, this results show that the proposed algorithm succeeds in reconstructing and maintaining even small details of unique intensity. Additionally, one can conclude that, in case the peak in the histogram is in fact too insignificant to get recognized by the algorithm, the results are merely residual artifacts limited to that specific intensity without corrupting the rest of the image or suppressing the uncorrected intensity.

6.2.3 Summary

This chapter intended to fathom the limits of the reference histogram constrained reconstruction in terms of contrast to noise ratio (CNR) and detail fidelity.
In order to evaluate the ability to recover intensities in images of low CNR an undersampled acquisition on a phantom with variable CNR was simulated. The CNR in image space corresponds to the ratio of the peak distance and the spread of the single peaks in the histogram domain. Since the applied corrections relies on information gathered from the histograms it is crucial to observe the behaviour when the distance of intensity peaks is reduced. The evaluation demonstrated a successful recovery of the image and suppression of artifacts even at a CNR of only 1.66, measured at a intensity difference of 0.1.
Since the intensity histogram is a non-local measure, only depending upon the intensity and number of pixels per intensity, the recovery of details is secured as long as small structures are part of a bigger family of pixels of the same intensity, corresponding to an easily detectable peak in the histogram. Consequently, the detail fidelity was assessed on a structure with unique intermediate intensity and decreasing pixel count. The simulation demonstrated that the detail was recognized and preserved by the algorithm even at a pixel count of only 4, an extremely small number when compared to the total pixel count of $6.5 \cdot 10^5$.

7 Iterative Reconstruction of Few-View Grating-Based Phase-Contrast CT - an *in vitro* Mouse Model

As an extension to the described reconstruction results on radial MRI, a compressed sensing based iterative approach was also applied to grating based phase-contrast CT data sets. To comprehensively evaluate the applicability of the implemented iterative algorithm, a numerical phantom (cf. Section 7.2), as well as undersampled *in vitro* measurements using a high brilliance X-ray source (cf. Subsection 7.3.1) and a conventional source (cf. Subsection 7.3.2) were conducted. Using NUFFT and the iterative reconstruction, images were generated for qualitative and quantitative comparison with focus on regularizations commonly used in compressed sensing algorithms. Additionally, the novel introduced reference histogram constrained reconstruction is applied on two data sets from different X-ray sources (cf. Subsection 7.3.3). The windowing of the reconstructed images in the results section was chosen based on region of interest (ROI) evaluation. The minimum and maximum in the image structure of interest was detected and set to 10% and 90% of the gray scaling, unless otherwise stated.
The results presented in Section 7.2 and Subsections 7.3.1 and 7.3.2 are in parts based on the publication Gaass *et al.* [153].

7.1 Outline of the method

As explained in Subsection 3.1.1, according to the Fourier slice theorem, after a one-dimensional Fourier transform radial lines in k-space represent the acquired CT projections. In order to compensate for the differential nature of the acquired phase signal, the Hilbert filter [85] was implemented into the NUFFT algorithm. This leads to an initial, so called minimal energy reconstruction of the zero-filled PCCT sinogram. Subsequently, this image is subject to an optimization process, approaching the sparsest solution in the Wavelet and finite differences transformation domains. Equation 7.1 summarizes the penalized minimization based reconstruction.

$$\underset{X}{\operatorname{argmin}} \left[||FT(X) - y||_2 + \lambda_{WL}\ \mathbf{R}_{WL} + \lambda_{TV}\ \mathbf{R}_{TV} \right] \tag{7.1}$$

7.2 Numerical simulations

In order to initially assess the performance of the implemented algorithm on phase-contrast CT, data acquisition was simulated on a numerical Shepp-Logan phantom of matrix size

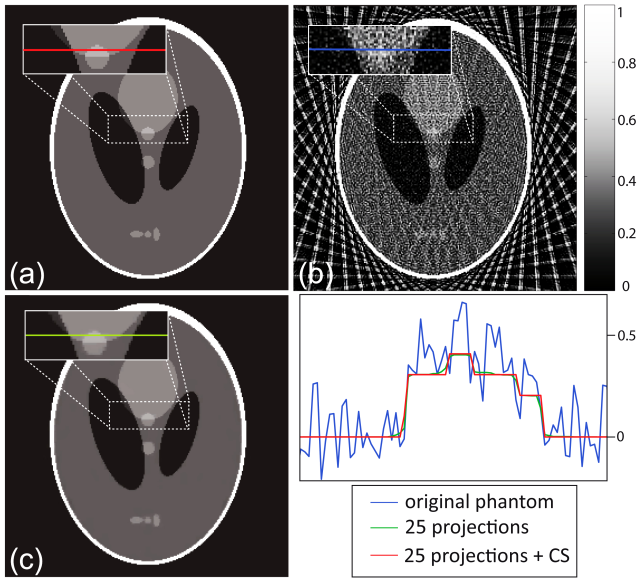

Figure 7.1: (a) Nyquist-sampled reconstruction of the Shepp-Logan phantom with a matrix size of 256×256. (b) Image reconstructed from 25 projections using NUFFT. (c) Reconstruction from 25 projections using the iterative algorithm. (d) Plot of one single line through a part of the reconstruction, marked within the magnified region.

256^2. The phantom was sampled by inversely applying a differential PCCT version of the NUFFT algorithm using 25 projections, corresponding to an undersampling factor of 16. Subsequently the implemented reconstruction was applied to the data set using both Wavelet and total variation regularization.

While Fig. 7.1(a) depicts the original Shepp-Logan phantom, Fig. 7.1(b) displays the NUFFT regridding reconstruction of the few-view data set. The 16-fold undersampled reconstruction shows strong streaking artifacts resulting in complete loss of detail information and sharpness of contrast edges. Figure 7.1(c) depicts the resulting iterative reconstruction. Streaking artifacts are successfully suppressed, with almost no perceptual loss in image details. The profiles presented in Fig. 7.1(d) demonstrate that the algorithm effectively reduced streaking artifacts while preserving edge sharpness and contrast properties of the reconstructed volume. When compared to the artifact impaired profile (blue line), the profile after iterative reconstruction (green line) is free of any aliasing and almost not distinguishable from the profile crossing the original object (red line). The numerical Shepp-Logan phantom indicates the possibility to generate images, very closely resembling the fully sampled original reconstruction with an undersampling factor of 16. Presumably, even lower sampling densities are applicable without losing vital information when using this object.

While the Shepp-Logan phantom is a satisfying object to simulate biological specimen, especially the human head in certain cases, its strong contrast properties and elliptical shapes are unnaturally beneficial for both total variation and projection sampling when compared

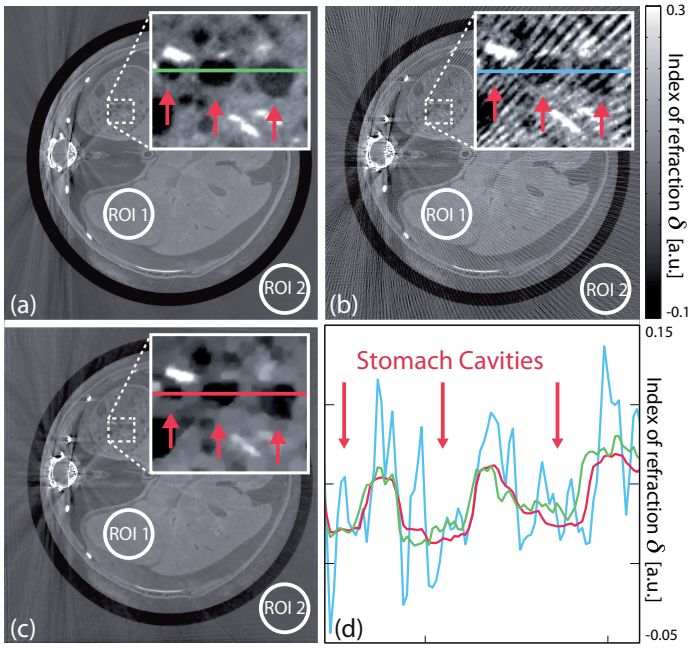

Figure 7.2: (a) Conventional reconstruction, based on a PCCT sinogram with 901 projections, including the used regions of interest (ROI). (b) Conventional reconstruction from 151 projections. (c) Reconstruction from 151 projections using the iterative algorithm. The windowing was chosen for best visual appearance. (d) Line profiles as marked in the enlarged areas.

to actual brain data. Generally speaking, CS-like reconstructions are increasingly effective with increasing sparsity, which applies for piecewise constant objects in case of the finite differences transformation and images that are naturally sparse in case of Wavelet transformation [154, 155]. Consequently, it is crucial to investigate more complex objects.

7.3 Experiments

7.3.1 Synchrotron radiation source

To evaluate the performance of the implemented algorithm on experimental data, a data set comprising both soft tissue and bone structures was reconstructed. In order to observe the results of the proposed algorithm when dealing exclusively with aliasing artifacts, rather then noise and beam hardening, the presented data was acquired in a high performance scan using a synchrotron radiation source at the European Synchrotron Radiation Facility (ESRF, beamline ID19, Grenoble, France). A formalin fixated mouse specimen was examined using a two grating Talbot interferometer (grating periods: $g_1 = 4.79\ \mu m$, $g_2 = 2.40\ \mu m$, inter-grating distance: $d(G1, G2) = 408\ mm$). 901 projections over 360 degrees with four phase steps were acquired at an X-ray energy of 35 keV and an exposure time of $1s$ per image. Using merely a number of 151 projections a 10-fold undersampled

	FS		US		IR	
	Mean δ	STD	Mean δ	STD	Mean δ	STD
ROI 1	0.061	0.006	0.082	0.025	0.061	0.007
ROI 2	-0.005	0.004	0.004	0.019	-0.003	0.003

Table 7.1: Mean pixel values and standard deviation within the regions of interest, depicted in Fig. 7.2 for the fully sampled (FS), the undersampled (US) and the iterative reconstruction (IR) case.

version of the original data was generated.
The fully sampled reconstruction in Fig. 7.2(a) exclusively shows phase wrapping artifacts from bone structures, while Fig. 7.2(b) displays the zero-filling reconstruction impaired by additional aliasing artifacts. Figure 7.2(c) depicts the result of the iterative reconstruction with almost completely suppressed aliasing artifacts.
As the theory of compressed sensing predicts, the algorithm is very effective when dealing with incoherent, or noise-like artifacts. Phase wrapping, as present in this data set, in contrary is of different nature and consequently only weakly suppressed. Detail and contrast fidelity of the iterative reconstruction however is not impaired by the remaining artifacts, as can also be observed in the line profiles presented in Fig. 7.2(d).
In addition to the visual comparison, the synchrotron data set was quantitatively evaluated on the basis of a region of interest (ROI) analysis. The mean pixel value and standard deviation (STD) among the pixels comprised in the marked ROIs were calculated and are compared in Table 7.3.1. The assessment shows that, while maintaining the original pixel intensities, the implemented algorithm was able to reduce the standard deviation within the ROIs by 35% compared to the undersampled reconstruction.

The resulting image, reconstructed from data, undersampled by a factor of 10 shows no residual aliasing artifacts, even when confronted with bone artifacts, while vital details and contrast information are maintained. These observations are also confirmed by quantitative evaluation. Both regions of interest were placed in areas without anatomical structure and present a reduction in standard deviation when compared to the zero-filling reconstruction.

7.3.2 Conventional tube

In order to assess the algorithm on data acquired using a conventional X-ray tube source, two tomographic data sets were examined. Measurements conducted with a conventional X-ray source (an ENRAF rotating anode X-ray tube with a Molybdenum target) were performed using a three grating interferometer in a symmetrical Talbot-Lau geometry. All three gratings had a period of 5.4 μm and were separated by a distance of 87.5 cm. The two absorption gratings have approximately 50 μm high gold structures, while the 8 μm high Nickel phase grating results in a π phase-shift for X-rays of 22.8 keV energy. The X-ray source was operated at a peak voltage of 35 kVp. A total of 701 projections over 360 degree were acquired with 11 phase steps and 5s exposure time each.
The reconstruction of an undersampled acquisition of a fluid phantom allowed to exclusively

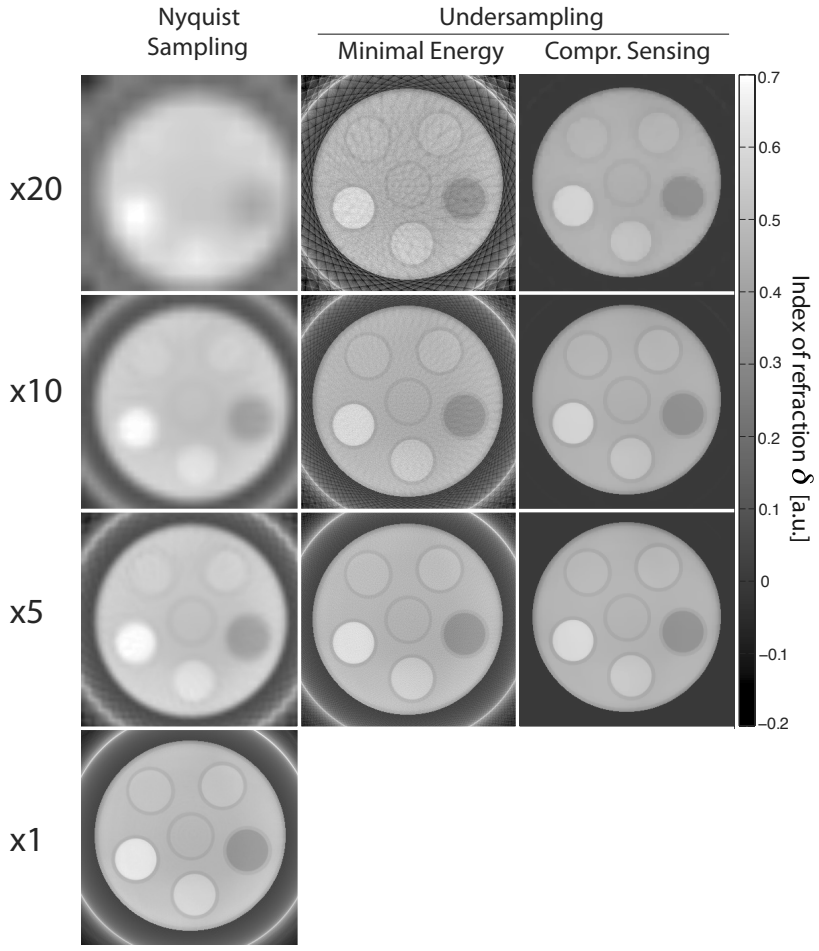

Figure 7.3: Phase-contrast CT measurement of a fluid phantom with undersampling factors up to 20. column 1: Nyquist sampling, satisfying the requirement $n_p = \frac{\pi}{2}n$ of the Nyquist-Shannon-theorem. column 2: NUFFT minimal energy reconstruction, zero-filling not sampled data points. column 3: Iterative reconstruction using both Wavelet sparsity and TV minimization.

focus on contrast fidelity of the iterative reconstruction when applied to PCCT data. The phantom comprised 6 polypropylene tubes, filled with saline solutions and pure liquids to generate a range of different phase-contrast signals (detailed description of the phantom in [156]). Data was acquired using a conventional X-ray source and an original sampling density of 701 projections. The reconstruction algorithm was applied to datasets with gradually decreasing number of projections up to an undersampling factor of 20.
Figure 7.3 presents a comparison of three different reconstruction approaches on the introduced fluid phantom data. Column 1 comprises reconstructions to a resolution corresponding to Equ. 3.12. That is, by rebinning the raw data the base resolution of the sinograms, subject to reconstruction is adapted to the number of projections and subsequently interpolated to the original matrix size. Evidently, this results in a significant reduction of details

to an extent of complete loss of information contained in the image. The reconstruction of undersampled data by zero-filling (column 2) shows heavy streaking artifacts of increasing severity with a decreasing number of used projections. Column 3 presents results of the iterative reconstruction in cases of three different undersampling factors (5,10 and 20). When compared to the original fully sampled image almost no perceptual loss in image quality is observed in the iterative reconstruction. In fact, the quality of the proposed reconstruction algorithm outperforms even the fully sampled image up to an undersampling factor of 10, due to suppression of noise.
The sensitivity of artifact reduction on solely soft tissue PCCT was evaluated on a tomographic data set of a formalin embedded, de-calcified mouse specimen (cf. Fig. 7.4). The chosen slices comprise different signal intensities and fine details. Initially the fixated mouse was sampled using 701 projections and reconstructed to a matrix size of 318^2. The performance of the algorithm was tested on a subset of only 50 of the original projections, hence an undersampling factor of 10.
The undersampled data set was reconstructed using zero-filling (Fig. 7.4(a)) and via rebinning (7.4(b)). Figure 7.4(c) displays the result of the application of the proposed algorithm, while Fig. 7.4(d) comprises the reconstruction of the fully sampled acquisition. The application of the iterative reconstruction led to a considerable reduction of not only aliasing artifacts, but also noise and apparent ring artifacts caused by the interpolation during NUFFT reconstruction. Additionally, residual cupping in the original data was corrected for in the iterative reconstruction, explaining the apparent change in contrast properties in the image center. Line profiles along the dashed black line clearly show that detail information in Fig. 7.4(a), as well as Fig. 7.4(b) is almost completely lost due to aliasing and loss of resolution, respectively. The pixel profile crossing the iterative reconstruction not only displays a recovery of contrast and details, but also a suppression of noise, when compared to the profile of the fully sampled reconstruction. The squared regions of interest specially present details in the object (marked with arrows) which have successfully been recovered during the iterative reconstruction.
While the proposed algorithm was capable of efficiently suppressing streaking artifacts in all presented data sets, the artifact reduction comes at a price. The reconstruction of the two presented phantoms clearly benefits from a strongly TV weighted minimization. However, applying Total Variation regularization to data sets with fine structures or intensity gradients can possibly result in reduced spatial resolution. Consequently, the magnitude of TV weighting has to be well balanced in order to avoid overcompensation of artifacts.
Wavelet convolution has shown to be very effective in sparsifying natural images. Future application of compressive sampling algorithms for PCCT, however, call for further investigation of alternative bases. While the imaging basis of CT is fixed, in contrary to applications such as magnetic resonance imaging, the transform basis is interchangeable. As aforementioned the success of reconstructing few-view measurements strongly depends on the incoherence of the two bases. Consequently, the quality of the reconstruction can further benefit from an investigation of alternative transformations adapted to the particular application of PCCT.

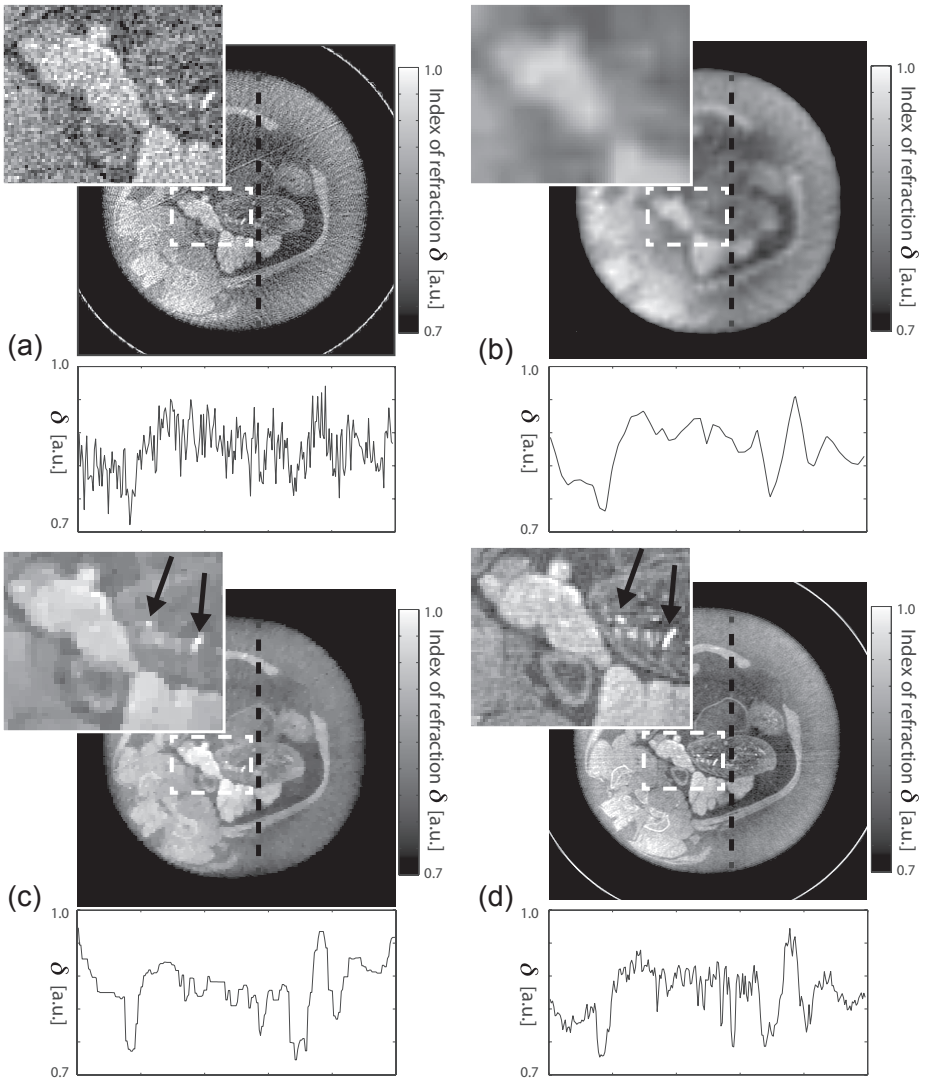

Figure 7.4: Reconstructions of a transverse slice of a fixated, de-calcified mouse. (a) NUFFT reconstruction of a few-view data set ($n_p = 50$, $n = 318$); (b) Few-view low-resolution Nyquist reconstruction ($n_p = 50$, $n = 32$) interpolated to 318^2; (c) Iterative reconstruction of the undersampling data, regaining image smoothness and resolving power comparable to the original; (d) Fully Nyquist sampled NUFFT reconstruction ($n_p = 701$, $n = 318$).

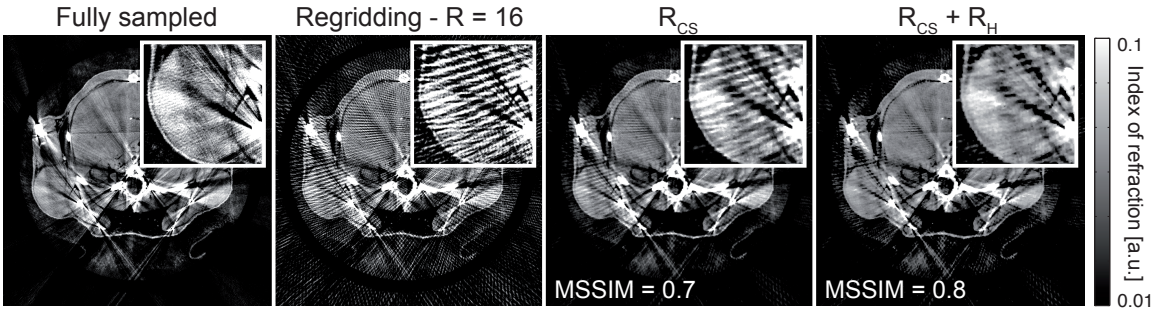

Figure 7.5: Reconstruction of a 16-fold undersampled slice of a fixated mouse specimen measured with a high brilliance synchrotron source. The aliasing artifacts visible in the regridding reconstruction are suppressed even more effectively by combining both regularizations ($R_{TV} + R_H$) when compared to the CS reconstruction alone. Additionally employing the histogram constraint resulted in an increase of 0.1 in the MSSIM quality measure.

7.3.3 RHiCA for PCCT

Similar to the application in MRI the iterative reconstruction algorithm in case of phase-contrast CT was extended by the histogram entropy regularization. The algorithm, including R_H was applied to a slice from the fixated mouse specimen ($R = 16$), evaluated in Subsection 7.3.1 as well as to the introduced fluid phantom ($R = 13$) (see Subsection 7.3.2). Figure 7.5 presents the results of reconstructing an undersampled data set of a fixated mouse specimen. A visual inspection shows that the outcome of combining both regularizations R_{CS} and R_H outperforms the pure compressed sensing reconstruction. Additionally the MSSIM shows an improvement of 0.1 due to the effective suppression of artifacts and noise cancellation when using the histogram constraint. It should be noted that in this evaluation an even higher reduction factor was used. However, the results show comparable quality to the assessment in Subsection 7.3.1 at a reduction factor of $R = 10$.
Figure 7.6 depicts the result from the reconstruction of the fluid phantom acquired with a conventional X-ray source. The regridded reconstruction is corrupted by strong streaking artifacts due to the high reduction factor of 13. While the artifacts are already very effectively suppressed using CS, the additional histogram regularization further improves noise cancellation, edge fidelity and smoothness of the reconstruction, resulting in an improvement in the calculated MSSIM value.

7.4 Summary

The present chapter focussed on the application of an iterative reconstruction similar to the common compressed sensing approach on grating based phase-contrast CT (PCCT). First the algorithm, regularized with Total Variation and Wavelet sparsity, was assessed on a numerical simulation of a 16-fold undersampled PCCT measurement of the 256^2-matrix Shepp-Logan phantom. The resulting image demonstrated complete suppression of arti-

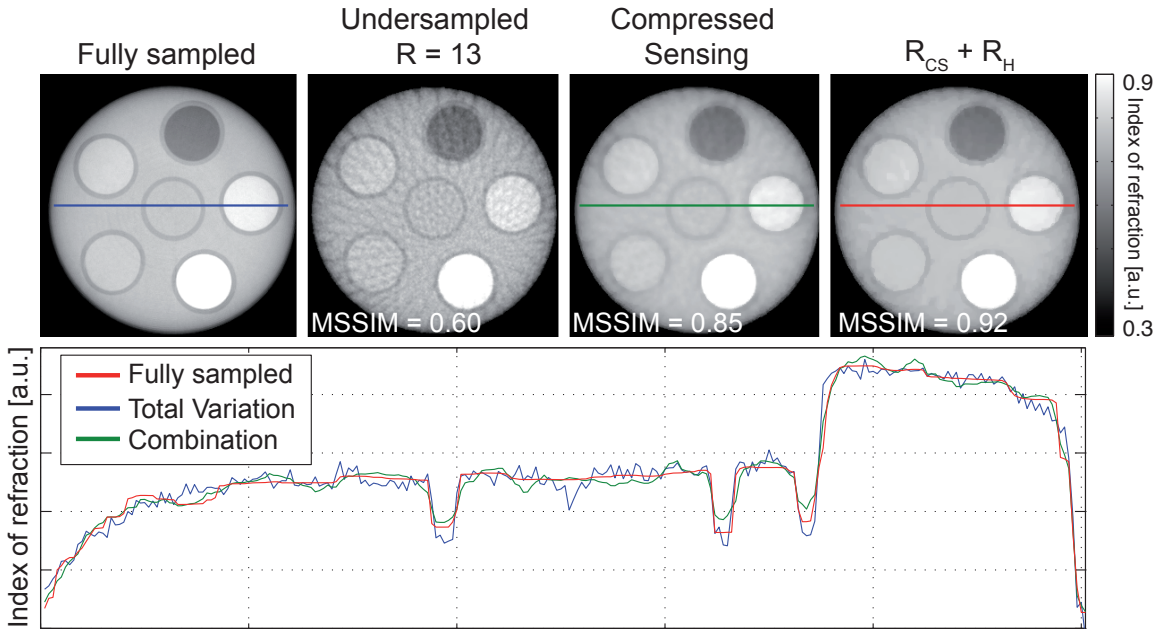

Figure 7.6: Iterative reconstruction using CS regularization and a combination of CS together with the histogram constraint (R_H). The combination of both constraints results in the image of best visual quality and highest MSSIM values of 0.92.

facts, while also maintaining contrast properties. However, as already explained in previous chapters Total Variation causes minor blurring in image details, such as the three elliptical structure in the lower part of the phantom.
The evaluation of the fixated mouse specimen acquired with a high-brilliance synchrotron source yielded an effective suppression of aliasing artifacts, unaffected by present bone artifacts. The region of interest (ROI) evaluation demonstrated a reduction of the standard deviation in two different ROIs by 35% when compared to the fully sampled reconstruction. The assessment of measurements performed on a grating-based set-up using a conventional source comprised a fluid phantom and a fixated de-calcified mouse specimen. In both applications noise and undersampling artifacts were successfully suppressed up to an reduction factor of 20 in case of the fluid phantom and 10 in the more complex *in vitro* object.
Finally, the regularization was extended by the reference histogram constraint R_H and applied on a different slice of the fixated mouse specimen imaged with a synchrotron source ($R = 16$) as well as on the introduced fluid phantom data set, acquired with a conventional source ($R = 13$). Both visual assessment and the MSSIM index clearly demonstrate an improvement when using a combination of CS and the histogram constraint. The MSSIM increased by 0.1 for the mouse reconstruction and by 0.07 in case of the fluid phantom.

8 Discussion and Summary

8.1 Reference histogram regularization

Within this work, the theory and application of reference histogram constrained reconstruction (RHiCA) was evaluated on both single slice and temporally resolved MR images. An algorithm was developed, which detects the impact of undersampling artifacts on the basis of the image's intensity histogram in comparison to a priorly computed reference. Employing both the impaired and the reference histogram, a correction compensating for undersampling effect in the histogram domain was calculated which in turn yields a correction for artifacts in image space. This correction was embedded in a iterative gradient driven framework for the suppression of aliasing in radially sampled MR measurements. The performance of the algorithm was first assessed on static single frame objects, using a low-resolution Nyquist reconstruction as reference for the correction. Subsequently, temporal redundancies in dynamic radial MRI were exploited in order to generate a reference histogram from the composition of consecutive k-spaces. A projection of the joint histogram gradient is used to correlate the impaired and the reference histogram. This projection was utilized to compute a correction, which counteracts the spread of intensity peaks in the target histogram, and re-identifies possibly merged intensity species by computing the corresponding correction in image space.

In static acquisition mode, in order to generate a reference histogram, the base resolution of the raw data was decreased to a degree the Nyquist limit for radial sampling is satisfied. Hence, the low-resolution reconstruction X_{lr} presents with no aliasing artifacts. This process makes an additional acquisition of a reference image obsolete, which is necessary in other reference based techniques. While the visibility of fine details in image space may suffer due to low resolution, evaluations demonstrated that the effect on the population of corresponding intensity peaks in histogram representation (H_{lr}) is only minor when compared to the impact of aliasing artifacts. Consequently, in H_{lr} both peak position and width, hence, the corresponding intensity and its variation are comparable to the fully sampled reconstruction of high spatial resolution. This fact can be explained in a very intuitive manner. As demonstrated in Subsection 3.2.1, radial aliasing artifacts or streaking has an impact on the whole reconstructed volume. Hence, a great number of pixels in image space is affected by alterations due to aliasing, which in turn causes a significant increase in intensity variations and in the extent of corresponding histogram peaks. Loss in spatial resolution on the other hand has merely an effect on high spatial frequencies, hence distinct intensity steps in the reconstruction. Consequently, merely pixels close to intensity steps are affected due to a smearing effect of edges. Pixels in areas of constant or almost constant intensity are completely unaffected by a change in resolution and fully contribute to one

single intensity peak in the histogram. That is, the intensity and width of intensity peaks in H_{lr} are almost unaffected by loss in spatial resolution.
A limitation to this argumentation is evident in case of complete loss of details in the process. However, in the context of the presented reconstruction it is important to differentiate between details in image space and details in the histogram domain. If details in image space (for instance small vessels in the presented head MRI in Fig. 4.7) are part of a bigger pool of pixels with the same intensity, these localized image details are associated with a major peak in the histogram domain. Hence, details in image space are not always details in histogram representation. An approach relying on the histogram representation, as RHiCA, is in these cases especially well suited to recover image space details. On the other hand, if the algorithm is confronted with an image detail of unique intensity, the detection and recovery of the corresponding peak becomes more challenging. Since the small number of pixels comprised in that singular detail corresponds to a minor peak in the histogram, the risk of this peak to get overshadowed by neighboring intensity species increases drastically. Results of the application of RHiCA on the simulated head MRI (cf. Fig. 4.6) demonstrated, however, that by employing the introduced patched version of RHiCA even minor peaks in the histogram can be recovered. The separation into image patches results in a reduction of the number of different intensities in one histogram. In an ideal case this leads to a complete division of pixel intensities into single histograms, preventing neighbouring peaks to overlap or enclose smaller peaks and increase the chance of re-identifying all included intensity peaks.
Clearly, the reconstruction task becomes increasingly challenging with a decreasing number of pixel per intensity and an increasing undersampling factor. The limitations of information gained from the intermediate histogram can be observed at very high undersampling factors, as used for the brain reconstruction (cf. Fig. 4.8). Heavy streaking might change the intensity of pixels to such an extent that the algorithm recognizes these as part of a different pixel species, which explains remaining artifacts especially in the image background. Using the histogram as basis of the reconstruction and thus being independent of the actual image appearance, is the major benefit of this approach. However, it also accounts for one shortcoming, visible in pure RHiCA reconstructions, such as the performed head MRI simulation (cf. Fig. 4.6). Since, in its current form, the algorithm is based on a pixel by pixel correction without taking neighboring pixels into account, the overall image smoothness is inferior when compared to other reconstruction techniques, such as compressed sensing (CS). In turn, CS reconstructions often present with an overly smoothed, almost comic-like image structure. Evaluations in Subsection 6.1.3 and Chapter 4 demonstrated general improvement in image quality, edge and detail fidelity and increase in the MSSIM value when employing a well balanced combination of CS and RHiCA. While each regularization weighting was provided for the presented reconstruction, especially the weighting parameters for CS heavily depend on the distinct appearance of the respective object. The effect of exaggerated constraints was evaluated in Section 6.1. Consequently, carefully chosen regularization parameters are necessary for an optimal reconstruction result.

When reconstructing dynamic interleaved MRI data, the core task is to suppress aliasing artifacts utilizing the whole gathered dynamic information without incorporating temporally averaged information. Starting from one dynamically acquired interleaved radial data set two alternative reconstructions can yield aliasing-free images, comprising contrast and detail information, respectively. Adapting the resolution of the reconstruction to satisfy the Nyquist limit results again in a low-resolution image (X_{lr}) carrying coarse but vital information about the basic contrast and image structure, which is usable as aliasing-free image space reference. Additionally, the aliasing-free composite image (X_{comp}), calculated from consecutive undersampled k-spaces comprises details and fine structures, however, is impaired by blurring and temporal averaging.
Several of the mentioned pre-existing techniques [17, 54–58] rely on the composition of dynamically acquired data as image space reference and struggle with these drawbacks. Employing the composite image as reference involves the risk of projecting image structures, not present in the original data but in X_{comp}, into the reconstruction of single image frames. The diameter of small vessels visible in a certain slice for instance can drastically vary due to respiratory or cardiac motion (as simulated in Fig. 5.2.1). Also the bulk motion associated with respiration and cardiac motion itself is a major issue in dynamic MRI. In some cases this might even result in a shift of certain structure out of the imaged field of view (FOV) for a certain number of frames. Temporal averaging in the composite image, however, includes all image features once present in the FOV. These are possibly incorporated as false additional information in the reconstruction. Blurring in the composite image on the other hand might cause an apparent loss in temporal resolution in the single frame reconstruction.
The impact of motion blurring on the intensity histogram computed from X_{comp} is comparable to the effect of loss in spatial resolution as already discussed for the single image case. Since affected pixels merely occur in heavily moving areas, the overall impact on the histogram is only minor. Temporal averaging on the other hand might even be beneficial for the reconstruction. Since image structures vanishing from the FOV comprise mostly small details, an temporally averaged representation in from of X_{comp} is likely to include a larger number of details with the same intensity. This in turn facilitates the detection of the corresponding peak in histogram space. As explained before, for the subsequent correction the actual image space appearance is irrelevant, avoiding the risk of incorporating temporally averaged structures altogether (cf. Fig. 5.5).
In particular, motion due to respiration, patient motion and cardiac pulsation can cause fluctuations of the appearance in image space. However, due to its non-local nature, the joint histogram entropy is not affected by changes in the spatial location in image space. Since the histogram merely depends on the number of pixels per intensity and not on the location of those in the image, the reference histogram reconstruction offers the possibility to correct dynamic data even of heavily moving objects. Consequently, the composite intensity histogram H_{comp} is especially well suited as reference in dynamic acquisitions.
The additional integration of X_{lr} as image space reference has shown to improve overall image smoothness and contrast fidelity in the reconstruction. The regularization term R_{lr} maximizes the similarity of the reconstruction to a low-resolution representation of the same

data set. Since X_{lr} is computed from each single frame, no temporal averaging is performed for the image space constraint. Any blurring possibly introduced by the low-resolution reference is corrected for by the dominating composite histogram constraint. Regularization weightings were chosen accordingly. The benefit of employing R_{lr} becomes increasingly evident at high reduction factors (cf. Fig. 5.7). While a reconstruction solely based on the reference histogram might have suffered from residual artifacts due to major intensity shifts, the low-resolution reference facilitates the separation between aliasing artifacts and original image structures. Furthermore, compared to the results presented using iSENSE the low-resolution image enforced reference histogram constrained reconstruction demonstrates clear improvement in perceivable image quality and the root mean square error.

The performance of reference histogram constraint reconstructions on increasingly demanding image structures was evaluated in Section 6.2. As aforementioned an increasing overlap of intensity peaks, hence a decreasing contrast-to-noise ratio (CNR), and the retrieval of histogram details pose major challenges for the reconstruction. CNR evaluations demonstrated that the recovery of histogram peaks could be achieved even at a CNR of 1.66 (cf. Fig. 6.9). Regarding minor histogram peaks the assessment has shown that an image detail with a pixel count of only 4 in an image of $6.5 \cdot 10^5$ pixels was maintained in the reconstruction, while heavy aliasing artifacts were effectively suppressed (cf. Fig. 6.11). This assessment emphasizes one major advantage for this approach. The worst case in a reconstruction occurs if an intensity with a small pixel count is not detected and corrected for in the histogram. However, since small details in image space are usually embedded in other intensities with a greater pixel count, the correction of the surrounding image area is virtually equal to a recovery of the image detail.

Conclusion In summary, the theory and application of reference histogram constrained reconstruction (RHiCA) on radially undersampled MRI data has successfully been presented on simulations and *in vivo* experiments. The presented work on the suppression of undersampling artifacts using reference histogram regularization can be used to drastically accelerate both single acquisition and dynamic MRI.
Single image acquisition results showed that aliasing from undersampling up to a factor of 13 can be corrected completely without perceptual loss of image quality and resolution. The quantitative evaluation demonstrated, that for certain objects the performance of RHiCA is of equal success as compressed sensing. However, the complementarity of features visible in both reconstructions suggests a simultaneous regularization, whose superior performance is confirmed by all quantitative assessments presented. Consequently, drawbacks known to be associated with compressed sensing can be counteracted by utilizing RHiCA. The combination of RHiCA and CS offers the possibility to further decrease measurement times in MRI without the necessity of additional scans or perceptual loss in image quality.
In dynamic MRI the comparison with iSENSE demonstrated the superior performance when using the developed algorithm. Therefore, measurement time in MRI acquisitions can be severely reduced using the composite histogram as constraint, which can be invested in an increase in temporal resolution in dynamic MRI applications. In particular, the composite

histogram constraint has proven to be of great benefit for the recovery of image details and might also be well suited to be included in other iterative dynamic MRI reconstruction algorithms in the future.

8.2 Compressed sensing for phase-contrast computed tomography

The aim of the presented work on phase-contrast CT (PCCT) reconstruction was to provide a compressive assessment of the application of CS inspired reconstruction on grating-based phase-contrast CT. The special focus was set on *in vitro* measurements using a conventional X-ray source in order to prove the feasibility of dose reduction via CS and take a step further towards the clinical application of PCCT.
The numerical Shepp-Logan phantom indicated the possibility to generate images, indistinguishable from the original reconstruction with an undersampling factor of 16 (cf. Fig. 7.1). Presumably, even lower sampling densities are applicable without losing vital information using this particular phantom. On the one hand the Shepp-Logan phantom is a satisfying object to simulate certain biological specimen, especially the human head. On the other hand its strong contrast properties and elliptical shapes make it a disproportionally beneficial specimen for both Total Variation (TV) and projection sampling compared to actual brain data. Generally speaking, the CS reconstruction is increasingly effective with increasing sparsity. This applies to piecewise constant objects in case of TV transformation and images that are initially sparse (e.g. angiography) in case of Wavelet transformation [154, 155]. Consequently, it is crucial to investigate more complex objects.
The first dataset with complex structures under investigation was a synchrotron source X-ray measurement of a fixated mouse (see Fig. 7.2). The resulting CS-image, reconstructed from data, undersampled by a factor of 10 showed no residual aliasing artifacts, even when confronted with bone artifacts, while vital details and contrast information are maintained. These observations were also confirmed by quantitative evaluation. Regions of interest were placed in areas without anatomical structure and presented a great reduction in standard deviation when compared to the zero-filling reconstruction and even the original image.
As already mentioned before, compressed sensing based reconstruction on phase-contrast CT aims to significantly reduce radiation dose in order to open the possibility for future translation into the clinical daily routine. Consequently, it is crucial to assess the achievable low-dose image quality when using a conventional X-ray source. PCCT images, especially those acquired with X-ray sources of low brilliance, are in addition to noise and streaking often impaired by cupping or dishing artifacts due to beam hardening [157]. Since TV is enforcing piecewise constant representation, smooth intensity changes are translated into intensity steps, which leads to so-called stair-casing artifacts. As performed here, a prior correction of these artifacts is necessary. Subsequently, both presented data sets (cf. Figs. 7.3 and 7.4) demonstrated a very effective image recovery up to undersampling factors of 10 and 20, respectively.
While the algorithm was capable of efficiently suppressing streaking artifacts in all presented data sets, the artifact reduction comes at a price. The reconstruction of the two presented

phantoms clearly benefit from a strongly TV weighted minimization. However, applying TV regularization to data sets with fine structures can possibly result in reduced spatial resolution or a comic-like appearance. Consequently, the magnitude of TV weighting has to be well balanced in order to avoid overcompensation of artifacts.
Wavelet convolution has shown to be very effective in sparsifying natural images. However, future application of compressive sampling algorithms for PCCT, call for further investigation of alternative bases. While the imaging basis of CT is fixed, in contrary to applications such as MRI, the transform basis is interchangeable. As aforementioned, the success of reconstructing few-view measurements strongly depends on the incoherence of the two bases. Consequently, the quality of the reconstruction can further benefit from an investigation of alternative transformations adapted to the particular application of PCCT.
Comparable to the observed effects of an additional histogram-based regularization in the form of RHiCA in MRI, results of the reconstruction of PCCT also data demonstrated a clear improvement when combining CS and RHiCA. A more effective suppression of artifacts, higher MSSIM values as well as higher edge and detail fidelity strongly suggest to embed RHiCA also in iterative PCCT reconstructions (cf. Figs. 7.5 and 7.6).
The computational task of detecting the sparsest solution among an infinite set of possible solutions is very demanding. Since regularizing the minimization process too heavily can possibly result in a local minimum and leads to the aforementioned loss in details and other remaining artifacts, the speed of the optimization is very limited. Weak regularization calls for a large number of iterations to achieve the desired artifact suppression. Consequently, with large data sets a reconstruction time of several minutes per slice is not uncommon. Intensive investigation has yet to be done in order to accelerate the reconstruction process.

Conclusion In summary, it was successfully demonstrated, both numerically and with experimental data that a reconstruction based on compressed sensing effectively suppresses undersampling artifacts in phase-contrast CT. Therefore, it is possible to reduce the number of projection images far beneath what the Nyquist/Shannon-theorem conventionally postulates, while maintaining resolution, contrast and visibility of details without perceptual loss. Undersampling factors of up to 16 evidently also correspond to a considerable reduction of dose.
Even if no undersampling is performed, CS offers the possibility to suppress noise, leading to an image with improved SNR, when compared to the fully sampled reconstruction. RHiCA demonstrated superior results when combined with CS on undersampled PCCT data.
Future work should comprise a detailed quantitative evaluation of the achievable resolution with the developed reconstruction algorithm. Additionally, the assessment of optimized penalty parameters poses a very important task.
While many issues, such as image quality with respect to clinical significance or the computational time of the algorithm are yet to be addressed, compressed sensing for phase contrast CT may open the door for future advanced applications, such as 4D-PCCT.

Bibliography

[1] F. Bloch. Nuclear induction. *Physical review*, 70(7-8):460, 1946.

[2] E. M. Purcell, H. Torrey, and R. V. Pound. Resonance absorption by nuclear magnetic moments in a solid. *Physical review*, 69(1-2):37, 1946.

[3] P. Mansfield and P. K. Grannell. Nmr diffraction in solids? *Journal of Physics C: solid state physics*, 6(22):L422, 1973.

[4] P. C. Lauterbur et al. Image formation by induced local interactions: examples employing nuclear magnetic resonance. *Nature*, 242(5394):190–191, 1973.

[5] E. Stejskal and J. Tanner. Spin diffusion measurements: spin echoes in the presence of a time-dependent field gradient. *The journal of chemical physics*, 42(1):288, 1965.

[6] D. Le Bihan, R. Turner, P. Douek, and N. Patronas. Diffusion MR imaging: clinical applications. *American Journal of Roentgenology*, 159(3):591–599, 1992.

[7] F. R. Korosec, R. Frayne, T. M. Grist, and C. A. Mistretta. Time-resolved contrast-enhanced 3D MR angiography. *Magnetic Resonance in Medicine*, 36(3):345–351, 1996.

[8] E. Petersen, I. Zimine, Y. L. Ho, and X. Golay. Non-invasive measurement of perfusion: a critical review of arterial spin labelling techniques. *British journal of radiology*, 79(944):688–701, 2006.

[9] V. M. Mai and S. S. Berr. MR perfusion imaging of pulmonary parenchyma using pulsed arterial spin labeling techniques: FAIRER and FAIR. *Journal of Magnetic Resonance Imaging*, 9(3):483–487, 1999.

[10] R. Christopher deCharms. Applications of real-time fMRI. *Nature Reviews Neuroscience*, 9(9):720–729, 2008.

[11] P. V. Prasad, R. R. Edelman, and F. H. Epstein. Noninvasive evaluation of intrarenal oxygenation with BOLD MRI. *Circulation*, 94(12):3271–3275, 1996.

[12] J. Yang, M.-X. Wan, Y.-M. Guo, et al. Pulmonary functional MRI: an animal model study of oxygen-enhanced ventilation combined with Gd-DTPA-enhanced perfusion. *Chinese medical journal*, 117(10):1489, 2004.

[13] H.-U. Kauczor, R. Surkau, and T. Roberts. MRI using hyperpolarized noble gases. *European radiology*, 8(5):820–827, 1998.

[14] D. C. Peters, F. R. Korosec, T. M. Grist, W. F. Block, J. E. Holden, K. K. Vigen, and C. A. Mistretta. Undersampled projection reconstruction applied to MR angiography. *Magnetic Resonance in Medicine*, 43(1):91–101, 2000.

[15] S. J. Malik, S. Schmitz, D. O'Regan, D. J. Larkman, and J. V. Hajnal. x-f choice: Reconstruction of undersampled dynamic MRI by data-driven alias rejection applied to contrast-enhanced angiography. *Magnetic resonance in medicine*, 56(4):811–823, 2006.

[16] M. Doyle, E. G. Walsh, G. G. Blackwell, and G. M. Pohost. Block Regional Interpolation Scheme for k-Space (BRISK): A Rapid Cardiac Imaging Technique. *Magnetic resonance in medicine*, 33(2):163–170, 1995.

[17] P. Kellman, F. H. Epstein, and E. R. McVeigh. Adaptive sensitivity encoding incorporating temporal filtering (TSENSE). *Magnetic Resonance in Medicine*, 45(5): 846–852, 2001.

[18] S. Kozerke, J. Tsao, R. Razavi, and P. Boesiger. Accelerating cardiac cine 3D imaging using k-t BLAST. *Magnetic resonance in medicine*, 52(1):19–26, 2004.

[19] S. Plein, S. Ryf, J. Schwitter, A. Radjenovic, P. Boesiger, and S. Kozerke. Dynamic contrast-enhanced myocardial perfusion MRI accelerated with k-t SENSE. *Magnetic Resonance in Medicine*, 58(4):777–785, 2007.

[20] H. Jung, K. Sung, K. S. Nayak, E. Y. Kim, and J. C. Ye. k-t FOCUSS: A general compressed sensing framework for high resolution dynamic MRI. *Magnetic Resonance in Medicine*, 61(1):103–116, 2009.

[21] S. Weber, A. Kronfeld, R. P. Kunz, K. Muennemann, G. Horstick, K.-F. Kreitner, and W. G. Schreiber. Quantitative myocardial perfusion imaging using different autocalibrated parallel acquisition techniques. *Journal of Magnetic Resonance Imaging*, 28(1):51–59, 2008.

[22] D. K. Sodickson and W. J. Manning. Simultaneous acquisition of spatial harmonics (SMASH): fast imaging with radiofrequency coil arrays. *Magnetic Resonance in Medicine*, 38(4):591–603, 1997.

[23] D. K. Sodickson. Tailored SMASH image reconstructions for robust in vivo parallel MR imaging. *Magnetic resonance in medicine*, 44(2):243–251, 2000.

[24] M. Blaimer, F. Breuer, M. Mueller, R. M. Heidemann, M. A. Griswold, and P. M. Jakob. SMASH, SENSE, PILS, GRAPPA: how to choose the optimal method. *Topics in Magnetic Resonance Imaging*, 15(4):223–236, 2004.

[25] M. A. Griswold, P. M. Jakob, R. M. Heidemann, M. Nittka, V. Jellus, J. Wang, B. Kiefer, and A. Haase. Generalized autocalibrating partially parallel acquisitions (GRAPPA). *Magnetic Resonance in Medicine*, 47(6):1202–1210, 2002.

[26] K. P. Pruessmann. Encoding and reconstruction in parallel MRI. *NMR in Biomedicine*, 19(3):288–299, 2006.

[27] M. A. Griswold, P. M. Jakob, M. Nittka, J. W. Goldfarb, and A. Haase. Partially parallel imaging with localized sensitivities (PILS). *Magnetic Resonance in Medicine*, 44(4):602–609, 2000.

[28] K. P. Pruessmann, M. Weiger, M. B. Scheidegger, P. Boesiger, et al. SENSE: sensitivity encoding for fast MRI. *Magnetic resonance in medicine*, 42(5):952–962, 1999.

[29] B. Madore. UNFOLD-SENSE: A parallel MRI method with self-calibration and artifact suppression. *Magnetic Resonance in Medicine*, 52(2):310–320, 2004.

[30] A. Haase, J. Frahm, D. Matthaei, W. Hanicke, and K.-D. Merboldt. Flash imaging. rapid nmr imaging using low flip-angle pulses. *Journal of Magnetic Resonance (1969)*, 67(2):258–266, 1986.

[31] J. Frahm, A. Haase, and D. Matthaei. Rapid three-dimensional MR imaging using the FLASH technique. *Journal of computer assisted tomography*, 10(2):363–368, 1986.

[32] H. Carr. Steady-state free precession in nuclear magnetic resonance. *Physical Review*, 112(5):1693, 1958.

[33] S. Plein, T. N. Bloomer, J. P. Ridgway, T. R. Jones, G. J. Bainbridge, and M. U. Sivananthan. Steady-state free precession magnetic resonance imaging of the heart: comparison with segmented k-space gradient-echo imaging. *Journal of Magnetic Resonance Imaging*, 14(3):230–236, 2001.

[34] K. Scheffler and S. Lehnhardt. Principles and applications of balanced SSFP techniques. *European radiology*, 13(11):2409–2418, 2003.

[35] J. Fessler. On NUFFT-based gridding for non-Cartesian MRI. *J Magn Reson*, 188 (2):191–5, 2007. ISSN 1090-7807.

[36] J. Ośullivan. A fast sinc function gridding algorithm for Fourier inversion in computer tomography. *IEEE Transactions on Medical Imaging*, 4(4):200–207, 1985.

[37] P. J. Beatty, D. G. Nishimura, and J. M. Pauly. Rapid gridding reconstruction with a minimal oversampling ratio. *IEEE Transactions on Medical Imaging*, 24(6):799–808, 2005.

[38] M. Lustig, D. Donoho, and J. M. Pauly. Sparse MRI: The application of compressed sensing for rapid MR imaging. *Magnetic resonance in medicine*, 58(6):1182–1195, 2007.

[39] D. L. Donoho and M. Elad. Optimally sparse representation in general (nonorthogonal) dictionaries via l1 minimization. *Proceedings of the National Academy of Sciences*, 100(5):2197–2202, 2003.

[40] D. L. Donoho. Compressed sensing. *IEEE Transactions on Information Theory*, 52 (4):1289–1306, 2006.

[41] E. J. Candès and M. B. Wakin. An introduction to compressive sampling. *Signal Processing Magazine, IEEE*, 25(2):21–30, 2008.

[42] E. J. Candès, J. Romberg, and T. Tao. Robust uncertainty principles: Exact signal reconstruction from highly incomplete frequency information. *Information Theory, IEEE Transactions on*, 52(2):489–509, 2006.

[43] E. J. Candès. The restricted isometry property and its implications for compressed sensing. *Comptes Rendus Mathematique*, 346(9):589–592, 2008.

[44] K. T. Block, M. Uecker, and J. Frahm. Undersampled radial MRI with multiple coils. Iterative image reconstruction using a total variation constraint. *Magnetic resonance in medicine*, 57(6):1086–1098, 2007.

[45] J. Tsao and S. Kozerke. MRI temporal acceleration techniques. *Journal of Magnetic Resonance Imaging*, 36(3):543–560, 2012.

[46] J. J. Van Vaals, M. E. Brummer, W. Thomas Dixon, H. H. Tuithof, H. Engels, R. C. Nelson, B. M. Gerety, J. L. Chezmar, and J. A. Den Boer. Keyhole method for accelerating imaging of contrast agent uptake. *Journal of Magnetic Resonance Imaging*, 3(4):671–675, 1993.

[47] R. Jones, O. Haraldseth, T. Müller, P. Rinck, and A. Øksendal. K-space substitution: A novel dynamic imaging technique. *Magnetic resonance in medicine*, 29(6):830–834, 1993.

[48] A. Shankaranarayanan, M. Wendt, A. J. Aschoff, J. S. Lewin, and J. L. Duerk. Radial KEYHOLE sequences for low field projection reconstruction interventional MRI. *Journal of Magnetic Resonance Imaging*, 13(1):142–151, 2001.

[49] B. Madore, G. H. Glover, N. J. Pelc, et al. Unaliasing by Fourier-encoding the overlaps using the temporal dimension (UNFOLD), applied to cardiac imaging and fMRI. *Magnetic Resonance in Medicine*, 42(5):813–828, 1999.

[50] P. Kellman, F. H. Epstein, and E. R. McVeigh. Adaptive sensitivity encoding incorporating temporal filtering (TSENSE). *Magnetic Resonance in Medicine*, 45(5): 846–852, 2001.

[51] S. J. Malik, S. Schmitz, D. OŔegan, D. J. Larkman, and J. V. Hajnal. x-f choice: Reconstruction of undersampled dynamic MRI by data-driven alias rejection applied to contrast-enhanced angiography. *Magnetic resonance in medicine*, 56(4):811–823, 2006.

[52] J. Tsao, P. Boesiger, and K. P. Pruessmann. k-t BLAST and k-t SENSE: Dynamic MRI with high frame rate exploiting spatiotemporal correlations. *Magnetic Resonance in Medicine*, 50(5):1031–1042, 2003.

[53] M. Lustig, J. M. Santos, D. L. Donoho, and J. M. Pauly. kt SPARSE: High frame rate dynamic MRI exploiting spatio-temporal sparsity. In *Proceedings of the 13th Annual Meeting of ISMRM, Seattle*, page 2420, 2006.

[54] F. A. Breuer, P. Kellman, M. A. Griswold, and P. M. Jakob. Dynamic autocalibrated parallel imaging using temporal GRAPPA (TGRAPPA). *Magnetic resonance in medicine*, 53(4):981–985, 2005.

[55] C. Mistretta, O. Wieben, J. Velikina, W. Block, J. Perry, Y. Wu, and K. Johnson. Highly constrained backprojection for time-resolved MRI. *Magnetic resonance in medicine*, 55(1):30–40, 2006.

[56] K. M. Johnson, J. Velikina, Y. Wu, S. Kecskemeti, O. Wieben, and C. A. Mistretta. Improved waveform fidelity using local HYPR reconstruction (HYPR LR). *Magnetic Resonance in Medicine*, 59(3):456–462, 2008.

[57] J. C. Ye, S. Tak, Y. Han, and H. W. Park. Projection reconstruction MR imaging using FOCUSS. *Magnetic Resonance in Medicine*, 57(4):764–775, 2007.

[58] G.-H. Chen, J. Tang, and S. Leng. Prior image constrained compressed sensing (PICCS): a method to accurately reconstruct dynamic CT images from highly undersampled projection data sets. *Medical physics*, 35:660, 2008.

[59] R. A. Wiggins. Minimum entropy deconvolution. *Geoexploration*, 16(1):21–35, 1978.

[60] D. L. Donoho, I. M. Johnstone, J. C. Hoch, and A. S. Stern. Maximum entropy and the nearly black object. *Journal of the Royal Statistical Society. Series B (Methodological)*, pages 41–81, 1992.

[61] J. C. Hoch and A. S. Stern. Maximum entropy reconstruction, spectrum analysis and deconvolution in multidimensional nuclear magnetic resonance. *Methods in enzymology*, 338:159–178, 2002.

[62] D. Hawkes. Algorithms for radiological image registration and their clinical application. *Journal of anatomy*, 193(3):347–361, 1998.

[63] M. Tseitlin, A. Dhami, S. S. Eaton, and G. R. Eaton. Comparison of maximum entropy and filtered back-projection methods to reconstruct rapid-scan EPR images. *Journal of Magnetic Resonance*, 184(1):157–168, 2007.

[64] M. Huang, R. Aaron, and C. Shiffman. Maximum entropy method for magnetoencephalography. *IEEE Transactions on Biomedical Engineering*, 44(1):98–102, 1997.

[65] S. Somayajula, C. Panagiotou, A. Rangarajan, Q. Li, S. R. Arridge, and R. M. Leahy. PET image reconstruction using information theoretic anatomical priors. *IEEE Transactions on Medical Imaging*, 30(3):537–549, 2011.

[66] C. P. Hess, Z.-P. Liang, and P. C. Lauterbur. Maximum cross-entropy generalized series reconstruction. In *5th IEEE EMBS International Summer School on Biomedical Imaging*, pages 8–pp. IEEE, 2002.

[67] C. E. Shannon. Communication in the presence of noise. *Proceedings of the IRE*, 37 (1):10–21, 1949.

[68] C. E. Shannon. A mathematical theory of communication. *ACM SIGMOBILE Mobile Computing and Communications Review*, 5(1):3–55, 2001.

[69] D. J. Larkman, P. G. Batchelor, D. Atkinson, D. Rueckert, and J. V. Hajnal. Beyond the g-factor limit in sensitivity encoding using joint histogram entropy. *Magnetic resonance in medicine*, 55(1):153–160, 2006.

[70] E. Wong. Joint Reconstruction of Under-Sampled Multiple Contrast Images Using Mutual Information. In *Proc. Intl. Soc. Mag. Reson. Med. 20 (2012)*, page 11. ISMRM, 2012.

[71] W. C. Röntgen. Über eine neue art von strahlen (vorläufige mitteilung). *Sitzungsberichte der Physikalisch-medizinischen Gesellschaft*, 1895.

[72] A. Snigirev, I. Snigireva, V. Kohn, S. Kuznetsov, and I. Schelokov. On the possibilities of X-ray phase contrast microimaging by coherent high-energy synchrotron radiation. *Review of Scientific Instruments*, 66(12):5486–5492, 1995.

[73] V. Ingal and E. Beliaevskaya. X-ray plane-wave topography observation of the phase contrast from a non-crystalline object. *Journal of Physics D: Applied Physics*, 28(11): 2314, 1995.

[74] T. Davis, D. Gao, T. Gureyev, A. Stevenson, and S. Wilkins. Phase-contrast imaging of weakly absorbing materials using hard X-rays. *Nature*, 373(6515):595–598, 1995.

[75] C. David, B. Nohammer, H. Solak, and E. Ziegler. Differential X-ray phase contrast imaging using a shearing interferometer. *Applied physics letters*, 81(17):3287–3289, 2002.

[76] A. Momose. Phase-sensitive imaging and phase tomography using X-ray interferometers. *Optics Express*, 11(19):2303–2314, 2003.

[77] T. Weitkamp, A. Diaz, C. David, F. Pfeiffer, M. Stampanoni, P. Cloetens, E. Ziegler, et al. X-ray phase imaging with a grating interferometer. *Opt. Express*, 13(16): 6296–6304, 2005.

[78] F. Pfeiffer, T. Weitkamp, O. Bunk, and C. David. Phase retrieval and differential phase-contrast imaging with low-brilliance X-ray sources. *Nature physics*, 2(4):258–261, 2006.

[79] F. Pfeiffer, C. Kottler, O. Bunk, and C. David. Hard x-ray phase tomography with low-brilliance sources. *Physical review letters*, 98(10):108105, 2007.

[80] M. Bech, T. H. Jensen, R. Feidenhans, O. Bunk, C. David, and F. Pfeiffer. Soft-tissue phase-contrast tomography with an X-ray tube source. *Physics in medicine and biology*, 54(9):2747, 2009.

[81] T. Donath, F. Pfeiffer, O. Bunk, C. Grünzweig, E. Hempel, S. Popescu, P. Vock, and C. David. Toward clinical X-ray phase-contrast CT: demonstration of enhanced soft-tissue contrast in human specimen. *Investigative radiology*, 45(7):445–452, 2010.

[82] A. Tapfer, M. Bech, A. Velroyen, J. Meiser, J. Mohr, M. Walter, J. Schulz, B. Pauwels, P. Bruyndonckx, X. Liu, et al. Experimental results from a preclinical X-ray phase-contrast CT scanner. *Proceedings of the National Academy of Sciences*, 109(39): 15691–15696, 2012.

[83] M. Stampanoni, Z. Wang, T. Thüring, C. David, E. Roessl, M. Trippel, R. A. Kubik-Huch, G. Singer, M. K. Hohl, and N. Hauser. The first analysis and clinical evaluation of native breast tissue using differential phase-contrast mammography. *Investigative radiology*, 46(12):801–806, 2011.

[84] D. Stutman, T. J. Beck, J. A. Carrino, and C. O. Bingham. Talbot phase-contrast x-ray imaging for the small joints of the hand. *Physics in medicine and biology*, 56 (17):5697, 2011.

[85] F. Pfeiffer, O. Bunk, C. Kottler, and C. David. Tomographic reconstruction of three-dimensional objects from hard X-ray differential phase contrast projection images. *Nuclear Instruments and Methods in Physics Research Section A: Accelerators, Spectrometers, Detectors and Associated Equipment*, 580(2):925–928, 2007.

[86] A. H. Andersen. Algebraic reconstruction in CT from limited views. *IEEE Transactions on Medical Imaging*, 8(1):50–55, 1989.

[87] K. M. Hanson and G. W. Wecksung. Bayesian approach to limited-angle reconstruction in computed tomography. *Journal of the Optical Society of America*, 73(11): 1501–1509, 1983.

[88] J. Gregor and T. Benson. Computational analysis and improvement of SIRT. *IEEE Transactions on Medical Imaging*, 27(7):918–924, 2008.

[89] H. Yu and G. Wang. SART-type image reconstruction from a limited number of projections with the sparsity constraint. *Journal of Biomedical Imaging*, 2010:3, 2010.

[90] A. C. Silva, H. J. Lawder, A. Hara, J. Kujak, and W. Pavlicek. Innovations in CT dose reduction strategy: application of the adaptive statistical iterative reconstruction algorithm. *American Journal of Roentgenology*, 194(1):191–199, 2010.

[91] X. Han, J. Bian, E. L. Ritman, E. Y. Sidky, and X. Pan. Optimization-based reconstruction of sparse images from few-view projections. *Physics in Medicine and Biology*, 57(16):5245, 2012.

[92] Z. Wang, Z. Huang, Z. Chen, L. Zhang, X. Jiang, K. Kang, H. Yin, Z. Wang, and M. Stampanoni. Low-dose multiple-information retrieval algorithm for X-ray grating-based imaging. *Nuclear Instruments and Methods in Physics Research Section A: Accelerators, Spectrometers, Detectors and Associated Equipment*, 635(1):103–107, 2011.

[93] E. Y. Sidky, M. A. Anastasio, and X. Pan. Image reconstruction exploiting object sparsity in boundary-enhanced X-ray phase-contrast tomography. *Optics express*, 18 (10):10404, 2010.

[94] T. Köhler, B. Brendel, and E. Roessl. Iterative reconstruction for differential phase contrast imaging using spherically symmetric basis functions. *Medical physics*, 38: 4542, 2011.

[95] I. Rabi, S. Millman, P. Kusch, and J. Zacharias. The Molecular Beam Resonance Method for Measuring Nuclear Magnetic Moments. The Magnetic Moments of ${}_3\mathrm{Li}^6$, ${}_3\mathrm{Li}^7$ and ${}_9\mathrm{F}^{19}$. *Physical Review*, 55(6):526, 1939.

[96] P. T. Callaghan. *Principles of nuclear magnetic resonance microscopy*. Oxford University Press, 1993.

[97] R. R. Ernst, G. Bodenhausen, A. Wokaun, et al. *Principles of nuclear magnetic resonance in one and two dimensions*, volume 14. Clarendon Press Oxford, 1987.

[98] A. Abraham. *The principles of nuclear magnetism*, volume 32. Oxford University Press, 1961.

[99] M. H. Levitt. *Spin dynamics*. John Wiley & Sons, 2013.

[100] L. G. Hanson. Is quantum mechanics necessary for understanding magnetic resonance? *Concepts in Magnetic Resonance Part A*, 32(5):329–340, 2008.

[101] F. Bloch. Nuclear induction. *Physical review*, 70(7-8):460, 1946.

[102] E. Hahn and D. Maxwell. Spin echo measurements of nuclear spin coupling in molecules. *Physical Review*, 88(5):1070, 1952.

[103] M. A. Bernstein, K. F. King, and X. J. Zhou. *Handbook of MRI pulse sequences*. Access Online via Elsevier, 2004.

[104] H. Nyquist. Certain topics in telegraph transmission theory. *Transactions of the American Institute of Electrical Engineers*, 47(2):617–644, 1928.

[105] R. Jerečić. *Entwicklung und Optimierung von Verfahren zur Messung der Spin-Spin-Relaxationszeiten in der Natrium-Magnetresonanztomographie bei* $1,5$ *Tesla*. PhD thesis, 2001.

[106] G. T. Herman. *Fundamentals of computerized tomography: image reconstruction from projections*. Springer, 2009.

[107] A. C. Kak and M. Slaney. *Principles of computerized tomographic imaging*. AC Kah and Malcolm Slaney, 1999.

[108] A. Momose, T. Takeda, A. Yoneyama, I. Koyama, and Y. Itai. Phase-contrast X-ray imaging using an X-ray interferometer for biological imaging. *Anal. Sci*, 17:i527–i530, 2001.

[109] F. Pfeiffer. Milestones and basic principles of grating-based x-ray and neutron phase-contrast imaging. In *AIP Conference Proceedings*, volume 1466, page 2, 2012.

[110] A. Momose. Recent advances in x-ray phase imaging. *Japanese Journal of Applied Physics*, 44:6355, 2005.

[111] P. Zhu, K. Zhang, Z. Wang, Y. Liu, X. Liu, Z. Wu, S. A. McDonald, F. Marone, and M. Stampanoni. Low-dose, simple, and fast grating-based x-ray phase-contrast imaging. *Proceedings of the National Academy of Sciences*, 107(31):13576–13581, 2010.

[112] J. Zambelli, N. Bevins, Z. Qi, and G.-H. Chen. Radiation dose efficiency comparison between differential phase contrast ct and conventional absorption ct. *Medical physics*, 37:2473, 2010.

[113] P. Modregger, F. Scattarella, B. Pinzer, C. David, R. Bellotti, and M. Stampanoni. Imaging the ultrasmall-angle x-ray scattering distribution with grating interferometry. *Physical review letters*, 108(4):048101, 2012.

[114] I. Zanette, M. Bech, A. Rack, G. Le Duc, P. Tafforeau, C. David, J. Mohr, F. Pfeiffer, and T. Weitkamp. Trimodal low-dose x-ray tomography. *Proceedings of the National Academy of Sciences*, 109(26):10199–10204, 2012.

[115] H. F. Talbot. LXXVI. Facts relating to optical science. No. IV. *The London and Edinburgh Philosophical Magazine and Journal of Science*, 9(56):401–407, 1836.

[116] F. Pfeiffer, M. Bech, O. Bunk, P. Kraft, E. F. Eikenberry, C. Brönnimann, C. Grünzweig, and C. David. Hard-X-ray dark-field imaging using a grating interferometer. *Nature materials*, 7(2):134–137, 2008.

[117] M. Bech. *X-ray imaging with a grating interferometer*. PhD thesis, Københavns Universitet Det Natur-og Biovidenskabelige Fakultet, Faculty of Science, Kemisk Institut, Department of Chemistry, 2009.

[118] P. B. Noël, J. Herzen, A. A. Fingerle, M. Willner, M. K. Stockmar, D. Hahn, M. Settles, E. Drecoll, I. Zanette, T. Weitkamp, et al. Evaluation of the potential of phase-contrast computed tomography for improved visualization of cancerous human liver tissue. *Zeitschrift für Medizinische Physik*, 2013.

[119] L. Feldkamp, L. Davis, and J. Kress. Practical cone-beam algorithm. *JOSA A*, 1(6): 612–619, 1984.

[120] C. David, J. Bruder, T. Rohbeck, C. Grünzweig, C. Kottler, A. Diaz, O. Bunk, and F. Pfeiffer. Fabrication of diffraction gratings for hard X-ray phase contrast imaging. *Microelectronic engineering*, 84(5):1172–1177, 2007.

[121] E. M. Haacke, R. W. Brown, M. R. Thompson, and R. Venkatesan. *Magnetic resonance imaging: physical principles and sequence design*, volume 1. Wiley-Liss New York:, 1999.

[122] R. D. Hoge, R. K. Kwan, and G. Bruce Pike. Density compensation functions for spiral MRI. *Magnetic Resonance in Medicine*, 38(1):117–128, 1997.

[123] E. Yudilevich and H. Stark. Spiral sampling in magnetic resonance imaging-the effect of inhomogeneities. *IEEE Transactions on Medical Imaging*, 6(4):337–345, 1987.

[124] J. G. Pipe, P. Menon, et al. Sampling density compensation in MRI: rationale and an iterative numerical solution. *Magnetic Resonance in Medicine*, 41(1):179–186, 1999.

[125] J. Xie, P. Lai, F. Huang, Y. Li, and D. Li. Cardiac magnetic resonance imaging using radial k-space sampling and self-calibrated partial parallel reconstruction. *Magnetic resonance imaging*, 28(4):495–506, 2010.

[126] K. Scheffler and J. Hennig. Reduced circular field-of-view imaging. *Magnetic resonance in medicine*, 40(3):474–480, 1998.

[127] S. Winkelmann, T. Schaeffter, T. Koehler, H. Eggers, and O. Doessel. An optimal radial profile order based on the Golden Ratio for time-resolved MRI. *IEEE Transactions on Medical Imaging*, 26(1):68–76, 2007.

[128] W. J. Morokoff and R. E. Caflisch. Quasi-random sequences and their discrepancies. *SIAM Journal on Scientific Computing*, 15(6):1251–1279, 1994.

[129] P. Bratley, B. L. Fox, and H. Niederreiter. Implementation and tests of low-discrepancy sequences. *ACM Transactions on Modeling and Computer Simulation (TOMACS)*, 2(3):195–213, 1992.

[130] J. Guo, M. Rosen, and H. Song. Evaluation of principal component analysis for highly undersampled radial DCE-MRI. In *Proceedings of the 15th Annual Meeting of ISMRM, Berlin, Germany*, 2007.

[131] H. Schomberg and J. Timmer. The gridding method for image reconstruction by Fourier transformation. *IEEE Transactions on Medical Imaging*, 14(3):596–607, 1995.

[132] J. Ośullivan. A fast sinc function gridding algorithm for Fourier inversion in computer tomography. *IEEE Transactions on Medical Imaging*, 4(4):200–207, 1985.

[133] J. I. Jackson, C. H. Meyer, D. G. Nishimura, and A. Macovski. Selection of a convolution function for Fourier inversion using gridding [computerised tomography application]. *IEEE Transactions on Medical Imaging*, 10(3):473–478, 1991.

[134] M. L. Lauzon and B. K. Rutt. Effects of polar sampling in k-space. *Magnetic resonance in medicine*, 36(6):940–949, 1996.

[135] J.-M. Jin. Electromagnetics in magnetic resonance imaging. *Antennas and Propagation Magazine, IEEE*, 40(6):7–22, 1998.

[136] C. Crawford and A. Kak. Aliasing artifacts in computerized tomography. *Applied Optics*, 18(21):3704–3711, 1979.

[137] B. E. Usevitch. A tutorial on modern lossy wavelet image compression: foundations of JPEG2000. *Signal Processing Magazine, IEEE*, 18(5):22–35, 2001.

[138] I. Daubechies. Orthonormal bases of compactly supported wavelets. *Communications on pure and applied mathematics*, 41(7):909–996, 1988.

[139] I. Daubechies. The wavelet transform, time-frequency localization and signal analysis. *IEEE Transactions on Information Theory*, 36(5):961–1005, 1990.

[140] L. I. Rudin, S. Osher, and E. Fatemi. Nonlinear total variation based noise removal algorithms. *Physica D: Nonlinear Phenomena*, 60(1):259–268, 1992.

[141] R. Constable and R. Henkelman. Why MEM does not work in MR image reconstruction. *Magnetic resonance in medicine*, 14(1):12–25, 1990.

[142] P. R. Moran. Observations on maximum entropy processing of MR images. *Magnetic resonance imaging*, 9(2):213–221, 1991.

[143] R. Fletcher and C. M. Reeves. Function minimization by conjugate gradients. *The computer journal*, 7(2):149–154, 1964.

[144] B. Girod. What's wrong with mean-squared error? In *Digital images and human vision*, pages 207–220. MIT press, 1993.

[145] P. C. Teo and D. J. Heeger. Perceptual image distortion. In *Proceedings of the IEEE International Conference on Image Processing*, volume 2, pages 982–986. IEEE, 1994.

[146] Z. Wang, A. C. Bovik, and L. Lu. Why is image quality assessment so difficult? In *IEEE International Conference on Acoustics, Speech, and Signal Processing (ICASSP)*, volume 4, pages IV–3313. IEEE, 2002.

[147] Z. Wang, A. C. Bovik, H. R. Sheikh, and E. P. Simoncelli. Image quality assessment: From error visibility to structural similarity. *IEEE Transactions on Image Processing*, 13(4):600–612, 2004.

[148] C. Cocosco, R.-S. Kwan, and D. Collins. BrainWeb: Simulated Brain Database, 1997.

[149] C. A. Cocosco, V. Kollokian, R. K.-S. Kwan, G. B. Pike, and A. C. Evans. Brainweb: Online interface to a 3D MRI simulated brain database. In *NeuroImage*. Citeseer, 1997.

[150] D. L. Collins, A. P. Zijdenbos, V. Kollokian, J. G. Sled, N. J. Kabani, C. J. Holmes, and A. C. Evans. Design and construction of a realistic digital brain phantom. *IEEE Transactions on Medical Imaging*, 17(3):463–468, 1998.

[151] R.-S. Kwan, A. C. Evans, and G. B. Pike. MRI simulation-based evaluation of image-processing and classification methods. *IEEE Transactions on Medical Imaging*, 18 (11):1085–1097, 1999.

[152] J. A. Fessler. Image reconstruction toolbox. `http://web.eecs.umich.edu/~fessler/irt/fessler.tgz`, 2012. [Online; accessed 23-Oct-2013].

[153] T. Gaass, G. Potdevin, M. Bech, P. Noël, M. Willner, A. Tapfer, F. Pfeiffer, and A. Haase. Iterative reconstruction for few-view grating-based phase-contrast ct - an in vitro mouse model. *EPL (Europhysics Letters)*, 102(4):48001, 2013.

[154] J. Bian, J. H. Siewerdsen, X. Han, E. Y. Sidky, J. L. Prince, C. A. Pelizzari, and X. Pan. Evaluation of sparse-view reconstruction from flat-panel-detector cone-beam CT. *Physics in Medicine and Biology*, 55(22):6575, 2010.

[155] X. Han, J. Bian, D. R. Eaker, T. L. Kline, E. Y. Sidky, E. L. Ritman, and X. Pan. Algorithm-enabled low-dose micro-CT imaging. *IEEE Transactions on Medical Imaging*, 30(3):606–620, 2011.

[156] A. Tapfer, M. Bech, B. Pauwels, X. Liu, P. Bruyndonckx, A. Sasov, J. Kenntner, J. Mohr, M. Walter, J. Schulz, et al. Development of a prototype gantry system for preclinical X-ray phase-contrast computed tomography. *Medical physics*, 38:5910, 2011.

[157] M. Chabior, T. Donath, C. David, O. Bunk, M. Schuster, C. Schroer, F. Pfeiffer, et al. Beam hardening effects in grating-based X-ray phase-contrast imaging. *Med. Phys*, 38(3):1189–1195, 2011.

List of Publications

Peer reviewed publications

G. Bauman, U. Lützen, M. Ullrich, T. Gaass, et al. *Pulmonary functional imaging: qualitative comparison of Fourier decomposition MR imaging with SPECT/CT in porcine lung.* Radiology, 260(2): 551-559, 2011

T. Gaass, J. Dinkel, G. Bauman, M. Zaiss, C. Hintze, A. Haase, F. Laun. *Non-contrast-enhanced MRI of the pulmonary blood volume using two-compartment-modeled T1-relaxation.* Journal of Magnetic Resonance Imaging, 36(2): 397-404, 2012

T. Gaass, G. Potdevin, M. Bech, P.B. Noël, M. Willner, A. Tapfer, F. Pfeiffer, A. Haase. *Iterative reconstruction for few-view grating-based phase-contrast CT – An in vitro mouse model.* Europhysics Letters, 102(4): 48001, 2013

T. Gaass, G. Bauman, G. Potdevin, P.B. Noël, A. Haase. *Rapid dynamic radial MRI via reference image enforced histogram constrained reconstruction.* Journal of Magnetic Resonance, DOI: 10.1016/j.jmr.2013.12.011

T. Gaass, G. Potdevin, G. Bauman, I. Dregely, T. Lasser, P. B. Noël, M. Schwaiger, A. Haase. *Reference histogram constrained artifact suppression (RHiCA) for radially undersampled magnetic resonance imaging.* Europhysics Letters, **under revision**

Conference Proceedings

T. Gaass, G. Potdevin, P.B. Noël, A. Tapfer, M. Willner, J. Herzen, M. Bech, F. Pfeiffer, A. Haase. *Compressed sensing for phase contrast CT.* AIP Conference Proceedings. Vol. 1466. 2012.

T. Gaass, G. Potdevin, M. Bech, J. Herzen, M. Willner, P.B. Noël, A. Tapfer, F. Pfeiffer, A. Haase. *Compressed sensing for phase-contrast computed tomography.* SPIE Medical Imaging. International Society for Optics and Photonics, 2012.

P. Zamecnik, G., J. Dinkel, H.-P. Schlemmer, T. Gaass. *Contrast Agent-Free High Resolution MRI for Prostate Cacner Detection Using a Two Compartment Inversion Recovery (TCIR) Technique.* Proceedings of the International Society for Magnetic Resonance in Medicine 20 (2012)

Conference contributions (selection)

T. Gaass, J. Dinkel, G. Bauman, M. Zaiss, A. Haase, F. Laun. *Non-Contrast-Enhanced High Resolution MRI of the Pulmonary Blood Volume Using a Two Compartment Model and T_1-Mapping.* Conference International Society for Magnetic Resonance in Medicine, Montreal, Canada, 2011 (oral)

T. Gaass, G. Bauman, J. Dinkel. *Evaluation of the Myocardial Regional Blood Volume Using Non-Contrast-Enhanced MRI - First Results.* European Congress of Radiology, Wien, 2011 (poster)

T. Gaass, G. Potdevin, A. Tapfer, M. Bech, M. Willner, F. Pfeiffer, A. Haase. *Compressed sensing for phase contrast CT.* 7. Internationales Symposium: Mehrschicht CT, Garmisch-Partenkirchen 2012 (poster)

T. Gaass, G. Potdevin, P.B. Noël, A. Tapfer, M. Bech, J. Herzen, M. Willner, F. Pfeiffer, A. Haase. *Compressed sensing for phase contrast CT.* Xnpig Conference, Tokyo, Japan, 2012 (poster)

T. Gaass, G. Potdevin, M. Bech, J. Herzen, M. Willner, P.B. Noël, A. Tapfer, F. Pfeiffer, A. Haase. *Compressed sensing for phase-contrast computed tomography.* SPIE Medical Imaging Conference, San Diego, USA, 2012 (Cum Laude poster award)

T. Gaass, G. Potdevin, G. Bauman, P.B. Noël, A. Haase. *Reference Histogram constrained artifact suppression (RHiCA) for incoherently undersampled magnetic resonance imaging.* Conference International Society for Magnetic Resonance in Medicine, Salt Lake City, USA, 2013 (oral)

T. Gaass, G. Potdevin, P.B. Noël, F. Pfeiffer, A. Haase. *Composite Histogram constrained artifact supression (CHiCA) for incoherently undersampled magnetic resonance imaging.* Conference International Society for Magnetic Resonance in Medicine, Salt Lake City, USA, 2013 (poster)

T. Gaass, G. Bauman, J. Dinkel, A. Haase, C. Hintze. *Validation of Two-Compartment Inversion Recovery (TCIR) MRI in a Multimodal Animal Study.* Conference International Society for Magnetic Resonance in Medicine, Salt Lake City, USA, 2013 (poster)

Acknowledgements

These last pages are dedicated to everyone who helped me in these past years. Their contributions and support eventually led to the present thesis. Without any of them this would have never been possible. With apologies to anyone who unintentionally remained unmentioned, I would like to specially thank

- *Prof. Dr. Axel Haase* for giving me the chance to work in an amazing scientific environment and for his trust, guidance and the creative scientific stimulus.

- *Prof. Dr. Franz Pfeiffer* for welcoming me in his group. Without the collaborations and support from his side I would have been lost in a field I had no experience in before.

- *Bernhard Gleich* for practically adopting me in his group. Without the occasional visit in the secret 'Stüberl' chamber, barbecues and Christmas party camping experiences, these 3.5 years would have been so much less fun. Thank you for the constant support.

- *Grzegorz Bauman* and *Guillaume Potdevin*. Dziekuje bardzo and merci beaucoup. They were neither my official supervisors, nor could I ever repay the support I received from the both of them in the past years. Without their help and input this thesis would have never happened. Thank you for great dinners and for introducing me to Pastis, Guillaume. And thank you Grzegorz for making hiking in Canada, TNT-evenings in Kiel and roof tops in Montreal so much fun.

- *Franz Schilling* for challenging me in exciting, almost unreal tournaments and for being more than a colleague during these years.

- *Christine, Alexandra, Norbert, Alex, Stephan* and *Matse* for coffee breaks, WWFs and for supporting me in giving the thesis its final touch.

- *Barbara Cervantes* for bringing some life back into the office, for bearing my grumpy phases and for reminding me that there is hardly something better then riding the bike along the Isar to get home from work.

- all the members of my group for interesting discussions, support and surprising visits at the Oktoberfest.

- the members of the E17 group. *Julia, Marian, Astrid, Arne, Michael* and everybody else, thank you so much for making these years so much fun. Thank you for the scientific input, the data you provided and for helping me understand at least a part of your work. I also especially appreciated the leisure-times during our numerous conference travels.

- *Peter Noël, Tobias Lasser* and *Isabel Dregely* for the support, research ideas and especially for the provided time and data.

- to the GSISH managing team *Ursula, Katha* and *Petra* for the constant support in networking all over the globe, the financial support and especially the fun we had, once work was done.

- *my parents* for their unconditional support. You have done so much for me that I don't even know where to begin thanking you. With the examples you set, you challenged me to do my best and pursue my goals, whichever they might be.

- my sister *Lisa* and my brother *Markus* for always believing in me and being there for me with an open ear and a helping hand whenever needed.